Structural Evolution and Self-assembly in Polymer Nanocomposites in Confined Geometry

by

Jenny Kim

A dissertation submitted in partial fulfillment
of the requirements for the degree of
Doctor of Philosophy
(Materials Science and Engineering)
in The University of Michigan
2011

Doctoral Committee:

Professor Peter F. Green, Chair
Professor John Kieffer
Professor Johannes W. Schwank
Assistant Professor Anish Tuteja

To my parents and my younger sister

Acknowledgements

First of all, I offer my sincerest thanks to my adviser Professor Peter Green for his tireless guidance and patience throughout my doctoral studies. He has continuously been supportive and encouraging my ideas and outcomes. Freedom of research was one of his policies that enabled me to be independent in organizing and carrying out the research projects. Peter was not only an outstanding research adviser but was a great mentor. I felt assurance talking with him whenever I ran into problems other than research. His warmness, great vision and understanding for his students were some of the aspects I will endeavor to resemble when I become somebody's mentor in the future.

I would like to express my gratitude to committee members Professor John Kieffer, Professor Johaness Schwank, Professor Anish Tuteja, and former member Professor David Martin. They gave insightful comments and encouragements during my preliminary exam and data meeting which helped me a lot to elaborate my work. Professor Martin and Professor Kieffer played an important role developing block copolymer project on controlling the morphology by raising critical questions during preliminary exam. Professor Schwank as a cognate professor provided different aspects to the coarsening project which enriched my study.

I would also like to acknowledge my current and previous Green group members. I really feel lucky to be surrounded by these smart, fun and wonderful guys. Since they all have strong and diverse academic backgrounds, I could resolve numerous problems associated with the research projects. Chelsea and Emmanouil were especially a huge help with my characterization skills and data analysis. Hengxi supported me a lot on calculations for refractive index and coarsening projects. Previous group members, Luciana, Abraham and Hyun, were the ones who trained and inspired on my projects. As a first year grad student, they have been very generous and patient on my mistakes and faults. I would like to extend my thanks to Jojo, Junnan, Peter, Carl and Bing for sharing wonderful lab and office experiences. I will really miss working with these guys wherever I work in the future.

I would like to mention EMAL staffs and J.A. Woollam engineers for their tremendous assistance in microscopes and spectroscopic ellipsometry respectively. With their great assistance, I could improve my characterization and analytical skills very effectively. Moreover, their suggestions have provided broader aspects and in-depth data interpretation to the paper.

MSE & AA friends especially FTC members hold a special place for me during my graduate studies. Being far away from families for the first time, it wasn't easy for me to adapt to a new environment. However, I was so lucky to meet loving and caring friends that I did not have to suffer from loneliness and stress. Among many friends, Kyungeun and Jihyang have been wonderful sisters to me. With them, my grad life was filled with exciting and enjoyable moments which I will never forget.

I owe much to my parents and younger sister in Korea for their unconditional support and encouragement. Even though I wasn't able to attend most of the events, my parents were very considerate and determined not to make me feel uncomfortable for not being with them especially when they are going through hardships. They always put my health and study as a priority than their own. Any of my achievement would not have been possible without their infinite belief and support.

Last, I would like to express my heartfelt appreciation to my fiancé, Dr. Seungcheol Yang for his endless love and support throughout this process.

TABLE OF CONTENTS

LIST OF FIGURES

LIST OF APPENDICES

ABSTRACT

Polymer nanocomposites (PNCs) are prepared by incorporating nanoparticles within a polymer host. The properties of PNCs are determined, in part, by the functionalities (e.g. electronic, optical, mechanical) of the nanoparticles and of the polymer host. Designing PNCs, however, is challenging due to uncontrolled enthalpic and entropic interactions that generally lead to micro and macrophase separation between the nanoparticles and the polymer; this negatively impacts the properties of the PNC. The goals of this thesis are the design of the structure and properties of thin film polymer nanocomposites in thin film geometry. Specifically, the research involved: (1) using thermodynamic principles to design and to fabricate thin film homopolymer/metallic nanoparticle PNCs; (2) investigating the dynamics of structural evolution of di-block copolymer (BCP)/metallic nanoparticle PNCs.

In order to control the structure of PNCs, particularly the nanoparticle distribution, polymer chains were grafted onto the surface of the nanoparticles. Prudent choices of the grafted chain lengths, grafting densities and nanoparticle radii enabled significant control of the nanoparticle distribution within the PNC. A morphological phase diagram, which describes regimes of miscibility, in terms of the molecular characteristics of the mixture, was developed for polystyrene/polystyrene-coated gold nanoparticle (PS/PS-Au) mixtures. This information enabled the design and fabrication of PS/PS-Au PNCs with

unusual optical absorption (surface plasmon) and dielectric properties. The refractive indices of the thin film PNCs were tailored by manipulating the nanoparticle concentration and distribution, and the film thickness.

In the second part of this thesis, it was shown how defects, specifically dislocations, had a significant impact on the nanoparticle distribution throughout thin film BCP hosts. When the nanoparticles are small compared to the average phase separated domains of the BCP, they reside preferentially within the domains. However, when the nanoparticles were comparable to the domain size they preferentially resided within the defect structures. This was shown to have a significant effect on the time-dependent evolution of surface nano-architecture of the BCP thin films.

CHAPTER 1

INTRODUCTION

1.1 Motivation and Research Objectives

The fabrication of polymer-based composites by the incorporation of inorganic fillers into a polymeric host has had a wide ranging impact on the technological applications and performance of polymer based systems. Recently, nanoscopic fillers (sub-100nm particle size) with diverse functionalities (e.g., optical, magnetic, and mechanical) have been intensively explored as they relate to the design of polymer composites, specifically polymer nanocomposites (PNCs). Owing to the high surface-area-to-volume ratio of nanoscopic fillers, low filler loading (<10 vol%) is often sufficient to maximize the property enhancements that can be attained by loading up to 40 vol% for conventional microscopic fillers. Applications of polymer nanocomposites are in principle limitless, and range from photovoltaics and batteries to biological sensors [1-5]. Even though the research related to PNCs has been around for over decades, designing PNCs is still considered to be challenging since nanoparticles (NPs) have tendency to agglomerate, e.g., by Van der Waals attraction between NPs [6,7].

Here, we have attempted to resolve the agglomeration problem by grafting polymer chains onto the nanoparticle surface hindering particle-particle interactions. Still, when chain grafted particles are incorporated into polymer matrices, host polymer chains

undergo entropic penalties near the particle surface due to the stretching of chains around particles. This entropic penalty will lead to phase separation between particles and host chains. Therefore, energetic interactions between the components must be carefully tailored to the spatial distribution of NPs.

Inclusion of NPs not only creates desired properties based on their functionalities but also alters other material characteristics, such as glass transition dynamics [8,9] and viscosity [10] from their intermolecular interactions between polymer chains and particles. Lack of understanding of these intricate changes in the host materials may introduce a series of problems, from the fabrication of the product to the durability of the material. For example, nanoparticles have shown to drive defect nucleation due to unfavorable interaction between host chains and nanoparticles [11,12], which leads to performance loss and failure of the material. Other problems can come from the shift in dynamics and thermal properties of the materials. To minimize these issues, it is critical to align material properties with well-defined PNC structures.

Here, we focus on the morphology of PNCs confined in thin film matrices as an extension of emerging thin film technologies such as data storage devices [13], optical coatings [14], and sensors [4]. The presence of interfacial interactions between polymer-interface and particle-interface in thin films were capable of changing the phase miscibility from their bulk counterpart.

The goal of this research is to establish the design rule by tuning the scaling behaviors that relate to material properties involve thermodynamic interactions and kinetics of thin film polymer/brush-coated nanoparticle mixtures. We begin the discussion with the energetic interactions lying in thin film polystyrene (PS)-coated Au

nanoparticles/ PS mixtures which ultimately determine the film morphology. The next step is to employ these well-defined systems to correlate to the optical properties of the film in terms of NP distribution, particle size, and film thickness, where surface plasmon resonance (i.e., collective oscillations of conduction electrons induced by incident light) peak was shown to shift. Then, we change the host to block copolymers to further investigate NP organization in the phase separated polymer matrices, particularly the role of defects in thin film block copolymers (BCPs). In the final chapter, we illustrate the NP effect on the structural evolution of the two-dimensional islands on thin film BCPs associated with surface-driven defects. The remaining sections of this chapter provide the background and the context of the work described in the body of this dissertation.

1.2 Background

1.2.1 Phase behavior of homopolymer/nanoparticle mixtures

1.2.1.1 Bulk Homopolymer/nanoparticle mixtures

To control the distribution of NPs throughout the polymer host, it is essential to understand the interactions between the entities. Ideally, the dispersion state of bare spherical NPs in the polymer host is determined by the volume fraction, ϕ, and NP size, R, where translational entropy $F_{trans} \approx (\phi/R^3)ln\phi$. However, there is an opposite effect as the volume fraction of NPs increases; the excluded volume effect leads to a loss of entropy which scales as ϕ^2 [15]. Also, depletion interaction between particles arises from host chains trying to minimize contact with the particles to reduce entropic penalty near the surface. Moreover, Van der Waals interactions of NPs, which scale as Hamaker constant R and $1/x_d$ (a distance between particles), increase the tendency to aggregate [6].

Molecular dynamics simulations have demonstrated that when there is a strong absorption of polymer into the particle surface, bridging interactions can be effective at reducing the miscibility of particles [16]. All these factors render the spatial distribution of NPs a highly challenging issue.

Functionalizing NPs with polymer brush is a well-known technique to control the dispersion of NPs within the polymer matrices [17,18]. Even for chemically identical polymer brush and host chains, that is, an athermal mixture $\chi K_B T = 0$ where χ is Flory interaction parameter, entropic effects need to be further controlled to attain a complete miscibility between two mixtures. Parameter space for athermal mixtures of polymer host and particles are the degree of polymerization of homopolymer chains, P, degree of polymerization, N, NP size, R, and grafting density, σ are the factors that controls the distribution of NPs [17,19]. The miscibility between grafted chains and host chains is described as either wet brush (Figure 1.1a) or dry brush (Figure 1.1b) where the former exhibits complete intermixing while the latter shows partial intermixing.

The scaling theory of interactions between host chains and polymer brush originated from the polymer brushes on the planar surface. When the interaction parameter is $\chi = 0$, surface tension between brush and host chains dominates the wetting of the host chain to the brush. For positive surface tension between brush and the host, $\gamma_{brush\text{-}host} > 0$, host chains will tend to dewet from the brush layer, often referred to as the autophobic dewetting of polymer chains. As $\gamma_{b\text{-}h}$ decreases almost to a negligible value, host chains will wet the polymer brush by interpenetration into the layer and lead to the surface stabilization. The former is a “dry” brush while the latter describes a “wet” brush condition; note that minimal interpenetration still exists in the dry brush state. Longer

host chains and higher σ of the brush are unfavorable conditions for wetting the brush since the entropic loss will become significant for both host and brush. In dry brush conditions, opposing brush will be attracted due to the depletion of host chains. But when grafted chains on the planar surface are sufficiently sparse, brush collapses into a semi-spherical cap which resembles a "mushroom" shape. Ferreira et al. [20] have estimated the wetting transition by self-consistent field (SCF) approximation to be $\sigma\sqrt{N} > (N/P)^2$ while the calculation reaches its limitation for stretched brushes, $\sigma\sqrt{N} > 1$. Brush further stretches to conform to host chains in comparison to the case where $\chi = 0$ at similar N and P. Diagram of states in Figure 1.2 illustrates the scaling behavior of grafted chains undergoing different conformation. Borukhov and Leibler [21] have generalized the scaling theory by integrating χ into SCF equations. They verified that when χ is negative, short-range attraction between grafted chains and host chains favors the interpenetration. The enthalpic interactions are dominant for long chains. The differences between enthalpic-dominated regimes and entropic-dominated regimes were identified to be approximately at $|\chi|P \cong 1$.

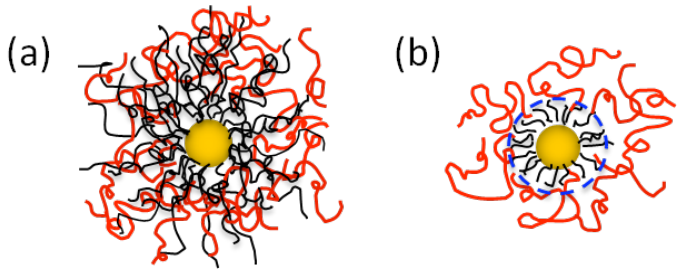

Figure 1.1 Chain-end grafted spherical nanoparticles of length N mixed with homopolymer melt of length P. (a) Wet brush condition: complete intermixing between homopolymer melt and grafted chains. (b) Dry brush condition: partial intermixing

between homopolymer melt and grafted chains.

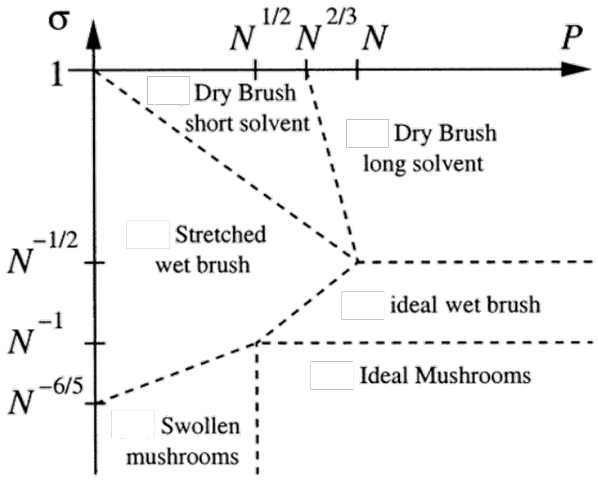

Figure 1.2 Diagram of states for grafted chains in contact with chemically identical homopolymer melt. Reprinted with permission [21].

The curvature effect becomes more significant as NPs become smaller, $R < N^{1/2}a$, where a is the segment size [22]. The higher the curvature surface is, the less the chains will crowd radially from the particle surface to the end point of the brush. Spherical brush (brush on spherical surface), hence, will have a greater tendency to intermix with host chains. By using self-consistent field theory (SCFT) and scaling theory, Victor et al.[23] were able to demonstrate that the wetting transition is influenced by the curvature effect. They used the ratio of interpenetration width, $w_{b\text{-}h}$, to the brush height l, as the scale to quantify the compatibility of grafted chains and polymer host. The segmental density of chains from the particle core was calculated and the critical wetting transition, N/P, increased with increasing particle curvature. The wetting behavior of large NPs, that is, $R > N^{1/2}a$, will be nearly identical to the behavior of brush on flat surface.

Phase miscibility of brush-coated NPs/homopolymer athermal mixtures is therefore controlled by N, P, R, ϕ, and σ. At low σ limit, below 0.1 chains/nm^2, core-core attraction has not been screened completely, and NPs form aggregates in an asymmetrical shape. Ackora et al.[24] used self-consistent theory and Monte Carlo simulation to confirm the asymmetric geometries of particle aggregates. Experimental data agreed well with the theory and simulation based on the concept of short-ranged "point" interparticle attraction. A morphological diagram was established by the grafting density as a function of grafted chain length/matrix chain length and was characterized by four regimes: spherical aggregates, strings, sheets, and dispersed. Interplay between the rearrangements of grafted chains and core-core attractions governed the development of such morphologies. On the other hand, for high σ, particles do not show any distinctive morphology when they aggregate since direct core-core attraction is completely screened by densely grafted chains. In the dry brush regime, particle aggregates randomly formed but the aggregate size increased with the increase in particle concentration. A more general description of the phase behavior of these systems has been established qualitatively but a complete picture remains elusive since the parameter space is complex for different regimes and materials.

1.2.1.2 Homopolymer/NP mixtures in thin films

Interactions between surfaces and the two components play an important role in the miscibility of homopolymer/NP mixtures confined in thin film geometry. McGarrity et al. [25] used density functional theory (DFT) to demonstrate the surface induced layering of particles near the hard surface and the exclusion of polymer chains from the surface. They referred to this as "entropic push". The first order surface transition has

been rationalized by the subtle interplay between the chain entropy and packing entropy near the surface. Size anisotropies between particle and chain, and conformational entropy were the determining factors for the surface transition. However, the "entropic push" only presents in the narrow particle size range according to the theory: for sufficiently small particles, polymer chains do not suffer an entropic loss by incorporating particles while for larger particles, polymer chains resemble the particle surface as a hard flat surface.

Earlier studies have shown that particles tend to stabilize the film when particles are expelled to interfaces. When particles were entropically-driven to interfaces, particles suppressed the dewetting by reducing the surface energy of the film. Hosaka et al. [11] systematically controlled the dispersion state of polyhedral oligomeric silsesquioxane (POSS) particles by functionalizing the surface in order to study the dewetting behavior of polystyrene films. They have confirmed that dewetting was inhibited by the surface-segregated particles while dispersed particles did not generate this effect. Also, the pinning of holes was pronounced for films in the dewetting process. Specifically, particles were shown to segregate to the boundaries of the holes, which suppressed the hole growth considerably. This tendency of NPs to segregate toward the interfaces can be used for self-healing materials and patterning by controlling the dewetting of the film.

Meli et al. [19] was the first to experimentally demonstrate the crossover from miscibility to surface segregation of brush-coated spherical NPs in thin film homopolymer host. At fixed N =10 and P = 1500, a transition from surface segregation to intermixing occurred by changing R_{core} from 2.5 nm to 1nm as translational entropy increases. For R_{core} = 2.5 nm, host chains suffer a conformational entropic loss near the

particle which led particles to segregate. However, at fixed R = 2.5 nm, host chains enable to intermixing with the grafted chains as the size ratio between brush size and host chain length, N/P increases. In the wet brush regime, particles generally remained dispersed within the thin film host with surface excess showing up in the depth profile. Even though the particle and the host are miscible, particles are still tend to segregate towards the surface due to the entropic gain in thin film mixtures.

In chapter 2, we examine the phase behavior of polystyrene-coated gold NPs in thin film PS host. Phase separation was driven by the difference in architecture between athermal mixtures. Three regimes have been identified from the phase behavior of the system: (1) phase separation accompanied by surface fluctuation, (2) complete interfacial segregation and (3) miscibility. Since the transition from intermixing to phase separation was gradual with the ratio of P over N, an intermediate regime has been indicated in the phase diagram.

Subsequently in chapter 3, we apply the system in chapter 2 to explore the effect of morphology on the optical properties of thin film PNCs. We demonstrate the control of optical constants of thin film PNCs with respect to the NP morphology, particle size, concentration, and film thickness. With the control of miscibility between nanoparticles and polymeric host, we were able to fabricate the film from single- to multi- layer structure with alternating particle-rich and particle-poor layers creating optical anisotropy in the film. Spectroscopic ellipsometry was used to characterize the optical spectra in homogeneous and phase separated mixtures by integrating the degree of anisotropy to the optical layers in the model.

1.2.2 Phase Behavior of Diblock Copolymer/NP Mixtures

1.2.2.1 Bulk Block Copolymer/NP Mixtures

A-b-B diblock copolymers (BCPs) serve as a great template for tailoring NP organization. BCPs, consist of two covalently bonded immiscible polymer blocks, phase-separate into various structures from cylinders and spheres to lamellae. Figure 1.2 illustrates a phase diagram of BCPs where f is the volume fraction of A block, χ is the Flory interaction parameter, and N is the degree of polymerization of BCP [26]. The surface functionalization of NPs is a general method for particles to stabilize into BCP matrices without aggregation [27-30]. When particles are functionalized to be compatible with one of the phase separated domains, e.g., A block, particles preferentially segregate to A domain upon phase separation.

Even though particles are enthalpically stabilized to A domain, one needs to consider parameters for entropic effects to tailor the precise spatial distribution within the block domain. Thompson et al. [31] calculated the free energy of BCP/NP mixtures using self-consistent field theory (SCFT) for polymers and density functional theory (DFT) for particles to predict the morphology of the particles within the BCP domain when $\chi_{A\text{-}NP} = 0$. As a result, the distribution of NPs within the domain changed by the ratio between particle size R and the periodic spacing of BCP domain. In the case of $R = 0.3R_0$, particles exclusively localized in the center of the domain to minimize conformational entropic loss of polymer chains. On the other hand, for R = 0.2R, particles distributed towards the interfaces since translational entropy dominates, while the conformational entropy of polymer chains is negligible. Following Thompson et al.'s pioneering work, many theoretical and experimental studies have studied wide range of parameter space to

control the NP localization [29, 30, 32-34]. In particular, the factors that determine the composite structure for polymer-grafted NPs are grafted chain size, areal chain density, χN, interfacial tension, volume fraction of particles as well as R/R_0. By implementing these parameters, more complex structures have been developed such as organizing two different particles in BCPs by differentiating the core size or chemistry of the grafted chain.

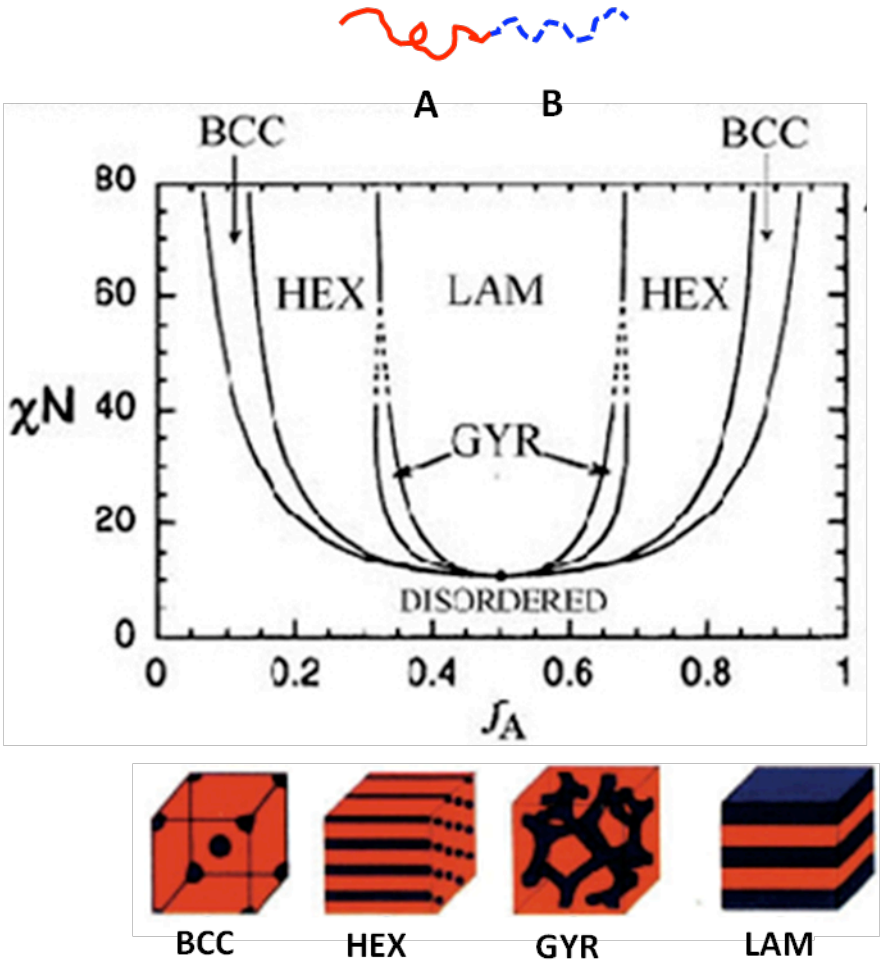

Figure 1.3 Mean-field phase diagram for symmetric A-b-B diblock copolymer, reproduced from [26]. The diagram depicts the different microstructures: BCC (spheres in a body-centered cubic array), HEX (cylinders in a hexagonal array), GTR (gyroid), and LAM (lamellar).

At relatively high NP concentrations, NPs were shown to shift the order-disorder transition (ODT) and order-order transition (OOT) [29, 33,35]. Depending on the degree of surface affinity of NPs to the BCP chain, BCPs exhibited an increase or decrease in the segregation strength which shifted ODT. Kim et al. [33] have illustrated OOT by the concentration gradient in the 100μm-thick PS-b-P2VP film. As concentration gradually increased from top-to-bottom of the film, a phase transition occurred from lamellar to either spherical or hexagonal structures based on the molecular weight, M_n, 59 kg/mol and 114 kg/mol of PS-b-P2VP. The transition was largely due to the swelling of the domain by NPs, which induced the interfacial curvature of the BCP chains. Morphological transitions in BCP/NP mixtures provide rich phase separation characteristics that need to be considered in designing PNC structures.

1.2.2.2 Block Copolymer/NP Mixtures in Thin Film Matrices

The self-assembly of BCPs in two dimensions (2D) has drawn considerable attention as scaffolds or templates for nanostructured materials [26]. To develop perfect long-range order, researchers have topographically [36] or chemically patterned [37] the substrate to direct the domain orientation and minimize the number of defects. A wide range of materials has been organized in thin film BCPs so far: quantum dots, spherical nanoparticles, nanorods, proteins, and metal/semiconductor channels [27, 35, 37, 38].

A number of studies have successfully presented a simple route to arranging inorganic NPs in cylindrical or lamellar thin film BCPs. Lin et al.[39] reported that the localization of CdSe particles in the P2VP domain of PS-b-P2VP film stabilized the hexagonally-ordered cylindrical structures. Solvent annealing of the film in liquid solvent

or in supercritical carbon dioxide enhances the degree of ordering with respect to high temperature vacuum annealing [39]. Kang et al. [37] chemically patterned the substrate to arrange the perpendicular lamellar structure of PS-b-PMMA film upon annealing.

Even though this topic has been investigated vigorously for over a decade, tailoring NP organization in thin film BCPs is still challenging thermodynamically and kinetically [40]. Despite the fact that the interaction parameter, χ dominates the thermodynamic interactions, interfacial interactions and wetting behavior of thin film BCPs near the wall place additional constraints on the morphologies near the thin film. Moreover, there is a tendency for NP to segregate towards the wall instead of spatially distributing throughout the preferential domain. Using SCFT, Lee et al. [41] demonstrated that when BCP film is confined to two hard walls, the majority of NPs directed to the walls. Interfacial segregation of NPs is due to depletion attraction despite of the wetting condition between polymer and NP. He et al. also pointed out that upon annealing NPs segregated towards the substrate and to the free surface as the structure shifted from micelles to cylinders. Surface segregation of NPs led to faster ordering near the surface while the process was slower for the bulk [40]. Other challenges associated with the kinetic process come from the variation in morphology of thin film BCP-NP mixtures during the fabrication procedures. For example, heterogeneous solvent evaporation in the drying process leads to irregularity in BCP domains and particle aggregations [37]. Evidently, more theoretical and experimental studies are essential to fully understand and optimize the self-assembly process in thin film BCP-NP mixtures.

1.2.2.3 Defect Evolution in BCPs upon Ordering

Without any external field applied to BCPs, various defects are prone to developing in BCP upon phase separation. A defect is a non-equilibrium structure usually formed during the late stage of phase separation. Defects strongly impacts on material properties such as mechanical and dielectric properties. Understanding the nature of the defect formation is critical to tackle the problems in a range of chemical and physical applications. For example, grain boundaries (GBs) in bulk lamellar BCPs are better established than in other structures. GBs developed in lamellar BCPs are largely divided into two morphologies: twist and tilt GBs. Gido et al. rationalized the formation of such morphologies in lamellar BCPs by calculating free energy density as a function of interfacial curvature within the structure [42, 43].

For thin film BCPs forming lamellae parallel to the substrate, defectless structures are only formed by the film thickness that is commensurate to multiple times of lamellar spacing, h = nL When the initial film thickness is other than h = nL, excess materials will evolve into islands or holes. Dislocations and/or disclinations were typically examined on the boundaries of island/hole structures to accommodate these structures [26, 44, 45]. Turner et al. [46] calculated the equilibrium position of edge dislocation that minimizes the free energy. This issue will be revisited in detail in chapter 4. For perpendicular lamellar structure, dislocations and disclinations are exposed to free surface. Hahm and Siebener were able to track defects by in-situ AFM studies to examine the defect mobility and morphological transitions. Substantial progress has been made in understanding defect-defect interactions and defect evolution involving propagation, relinking or joining, clustering, and annihilation.

Recently, studies in defect evolution have been moving towards an understanding of the effect on NP organization. Listak et al. [47] displayed NP aggregates along the grain boundaries formed in lamellar BCPs. While NPs strongly segregated to high-angle tilt GBs, i.e. T-junction and omega, NPs were not selective in low-angle tilt GBs, i.e. chevron grain boundaries (Figure 1.4). NPs not only organize along the GBs but also stabilized high-angle tilt GBs, which are barely examined in pure BCPs due to instability. An SCFT/DFT theoretical study by Thompson et al. provided qualitative evidence of Listak et al.'s observation. The theory predicted that NPs tend to be crowded in the regions of high packing frustration in GBs while NPs still show a sign of aggregation in regions of lesser packing frustration. They envisioned the feasibility of engineering "packing frustration" to self-organize NP clusters. In this context, we explored the role of defects on the self-assembly of NPs in lamellar-forming thin film BCPs (Chapter 4). This study proposed a novel method to self-organize NP clusters into defects trapped into boundaries of island/hole structures.

In the following chapter, we investigate the NP effect on coarsening dynamics of islands on lamellar BCP film. The structural evolution of islands is discussed in terms of classical coarsening mechanisms, Ostwald ripening, and coalescence, which can be characterized by the morphology of NPs sequestered in island boundaries.

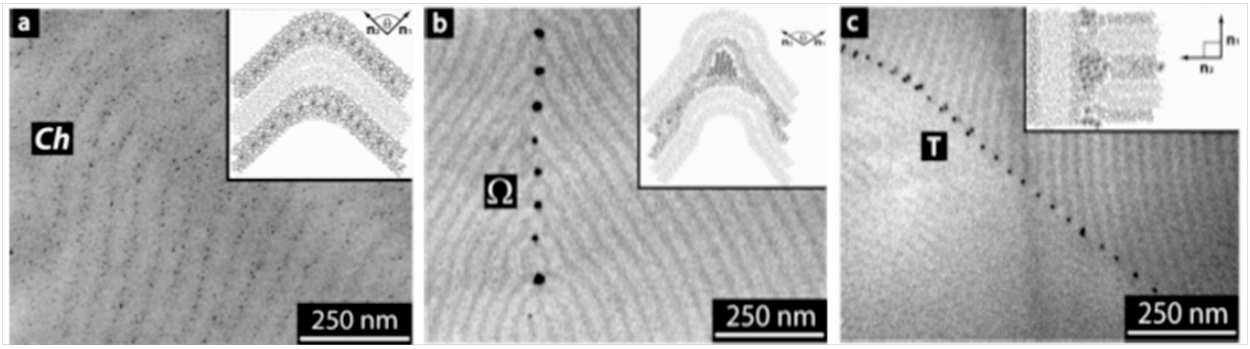

Figure 1.4 Transmission Electron Micrograph of Poly(styrene-block-ethylene propylene) copolymer/polystyrene coated-gold NP mixtures depicting a (a) chevron grain boundary, (b) omega-type grain boundary, and (c) T-junction grain boundary. Particle formed aggregates and periodically array along the high angle grain boundaries (omega-type and T-junction) while particle remained dispersed in polystyrene domain across the low angle grain boundary (chevron). Reprinted with permission. [47]

1.2.3 Processing polymer thin films under supercritical carbon dioxide ($scCO_2$)

Pressurized carbon dioxide is becoming an attractive alternative to organic solvents in polymer processing. Some advantages of CO_2 processing include but are not limited to: non-toxicity, controllability of solvent strength, and enhancement in interfacial and transport properties of the material [48-51].

Many studies have examined a wide range of CO_2 conditions related to the plasticization effect and decrease in T_g of bulk/thin film polymers. Conditions for glassy-to-rubbery transition rely on the interplay between thermal energy and CO_2 solubility [49, 52]. For amorphous polymer thin films, anomalous maxima swelling occurred under isothermal conditions where compressibility of CO_2 becomes largely dissimilar to the

bulk [53]. Likewise, by subjecting to $scCO_2$, a significant enhancement in crystallization was examined for Bisphenol A polycarbonate thin films comparing to the bulk analogue [48]. Differences between thin film and bulk was claimed to be due to the large surface excess of CO_2 [48, 53]. Moreover, interfacial width in the bilayer film was shown to extend even at very low CO_2 pressure. This characteristics can be employed to enhance interfacial properties of polymer layers [50, 51].

Morphology and phase transitions of BCPs/polymer blends could also be tailored by pressurized carbon dioxide. Watkins et al. demonstrated that LCST (lower critical transition) of PS/poly (vinyl methyl ether) blend can be reduced as much as 115 ºC at only 2.4MPa [54, 55]. Considerable shift in phase boundaries was caused by the increase in volume disparity and the screening effect of favorable interactions in CO_2. On the other hand, CO_2 can in some cases drive phase miscibility for polymers that carry ODT (order-disorder transition)/UCST (upper critical transition) by screening repulsive intermolecular interactions. Morphologies of polymer blends and BCPs were controlled by tuning the temperature and pressure of CO_2. For example, structural inversion of two segments in BCP micelles took place upon annealing in $scCO_2$ as one of the blocks had a strong affinity to CO_2 [18, 56]. The size of the micelle aggregates was modified by annealing conditions where the decrease in $scCO_2$ activities led to an increase in size [56].

Here, $scCO_2$ annealing was particularly important for low temperature annealing. Sorption of CO2 plasticizes the polymer and lowers the glass transition temperature and viscosity for the polymer. Using $scCO_2$ annealing, therefore, prevents ligands from thermal desorption and avoid the steric stabilization of NPs. Evidence of detachment of thiol-terminated ligands has been seen several studies which resulted in aggregation and

coarsening of particles [7]. For this reason, in this study $scCO_2$ was selected as the annealing environment for processing thin film polymer/NP mixtures.

1.3 References

1. Atwater, H. A.; Polman, A., Plasmonics for improved photovoltaic devices. Nat Mater 9, (3), 205-213.

2. Croce, F.; Appetecchi, G. B.; Persi, L.; Scrosati, B., Nanocomposite polymer electrolytes for lithium batteries. Nature 1998, 394, (6692), 456-458.

3. Barry, P. R.; Peter, P.; Stephen, R. F., Long-range absorption enhancement in organic tandem thin-film solar cells containing silver nanoclusters. AIP: 2004; Vol. 96, p 7519-7526.

4. Nath, N.; Chilkoti, A., A Colorimetric Gold Nanoparticle Sensor To Interrogate Biomolecular Interactions in Real Time on a Surface. Analytical Chemistry 2001, 74, (3), 504-509.

5. Yan, H.; Park, S. H.; Finkelstein, G.; Reif, J. H.; LaBean, T. H., DNA-Templated Self-Assembly of Protein Arrays and Highly Conductive Nanowires. In 2003; Vol. 301, pp 1882-1884.

6. Green, P. F., The structure of chain end-grafted nanoparticle/homopolymer nanocomposites. Soft Matter 2011.

7. Meli, L.; Green, P. F., Aggregation and Coarsening of Ligand-Stabilized Gold Nanoparticles in Poly(methyl methacrylate) Thin Films. ACS Nano 2008, 2, (6), 1305-1312.

8. Arceo, A.; Meli, L.; Green, P. F., Glass transition of polymer-nanocrystal thin film mixtures: Role of entropically directed forces on nanocrystal distribution. Nano Letters 2008, 8, (8), 2271-2276.

9. Oh, H.; Green, P. F., Polymer chain dynamics and glass transition in athermal polymer/nanoparticle mixtures. Nature Materials 2009, 8, (2), 139-143.

10. Mackay, M. E.; Dao, T. T.; Tuteja, A.; Ho, D. L.; Van Horn, B.; Kim, H. C.; Hawker, C. J., Nanoscale effects leading to non-Einstein-like decrease in viscosity. Nature Materials 2003, 2, (11), 762-766.

11. Hosaka, N.; Torikai, N.; Otsuka, H.; Takahara, A., Structure and Dewetting

Behavior of Polyhedral Oligomeric Silsesquioxane-Filled Polystyrene Thin Films. Langmuir 2006, 23, (2), 902-907.

12. Sharma, S.; Rafailovich, M. H.; Peiffer, D.; Sokolov, J., Control of Dewetting Dynamics by Adding Nanoparticle Fillers. Nano Letters 2001, 1, (10), 511-514.

13. Jo, A.; Joo, W.; Jin, W.-H.; Nam, H.; Kim, J. K., Ultrahigh-density phase-change data storage without the use of heating. Nat Nano 2009, 4, (11), 727-731.

14. Xi, J. Q.; Schubert, M. F.; Kim, J. K.; Schubert, E. F.; Chen, M.; Lin, S.-Y.; LiuW; Smart, J. A., Optical thin-film materials with low refractive index for broadband elimination of Fresnel reflection. Nat Photon 2007, 1, (3), 176-179.

15. Hall, L. M.; Jayaraman, A.; Schweizer, K. S., Molecular theories of polymer nanocomposites. Current Opinion in Solid State and Materials Science 14, (2), 38-48.

16. Hur, K.; Jeong, C.; Winkler, R. G.; Lacevic, N.; Gee, R. H.; Yoon, D. Y., Chain Dynamics of Ring and Linear Polyethylene Melts from Molecular Dynamics Simulations. Macromolecules 44, (7), 2311-2315.

17. Kim, J.; Green, P. F., Phase Behavior of Thin Film Brush-Coated Nanoparticles/Homopolymer Mixtures. Macromolecules 2010, 43, (3), 1524-1529.

18. Meli, L.; Li, Y.; Lim, K. T.; Johnston, K. P.; Green, P. F., Templating of Gold Nanocrystals in Micellar Cores of Block Copolymer Films. Macromolecules 2007, 40, (18), 6713-6720.

19. Meli, L.; Arceo, A.; Green, P. F., Control of the entropic interactions and phase behavior of athermal nanoparticle/homopolymer thin film mixtures. Soft Matter 2009, 5, (3), 533-537.

20. Ferreira, P. G.; Ajdari, A.; Leibler, L., Scaling Law for Entropic Effects at Interfaces between Grafted Layers and Polymer Melts. Macromolecules 1998, 31, (12), 3994-4003.

21. Borukhov, I.; Leibler, L., Enthalpic Stabilization of Brush-Coated Particles in a Polymer Melt. Macromolecules 2002, 35, (13), 5171-5182.

22. Xu, J. J.; Qiu, F.; Zhang, H. D.; Yang, Y. L., Morphology and interactions of polymer brush-coated spheres in a polymer matrix. Journal of Polymer Science Part B-Polymer Physics 2006, 44, (19), 2811-2820.

23. Victor, P.; Venkat, G.; Athanassios, Z. P.; Hongjun, L.; Sanat, K. K., Modeling the anisotropic self-assembly of spherical polymer-grafted nanoparticles. AIP: 2009; Vol. 131, p 221102.

24. Akcora, P.; Liu, H.; Kumar, S. K.; Moll, J.; Li, Y.; Benicewicz, B. C.; Schadler, L.

S.; Acehan, D.; Panagiotopoulos, A. Z.; Pryamitsyn, V.; Ganesan, V.; Ilavsky, J.; Thiyagarajan, P.; Colby, R. H.; Douglas, J. F., Anisotropic self-assembly of spherical polymer-grafted nanoparticles. Nat Mater 2009, 8, (4), 354-359.

25. McGarrity, E. S.; Frischknecht, A. L.; Mackay, M. E., Phase behavior of polymer/nanoparticle blends near a substrate. AIP: 2008; Vol. 128, p 154904.

26. Marencic, A. P.; Register, R. A., Controlling Order in Block Copolymer Thin Films for Nanopatterning Applications. In 2011; Vol. 1, pp 277-297.

27. Bockstaller, M.; Kolb, R.; Thomas, E. L., Metallodielectric Photonic Crystals Based on Diblock Copolymers. Advanced Materials 2001, 13, (23), 1783-1786.

28. Bockstaller, M. R.; Mickiewicz, R. A.; Thomas, E. L., Block Copolymer Nanocomposites: Perspectives for Tailored Functional Materials. Advanced Materials 2005, 17, (11), 1331-1349.

29. Kim, B. J.; Fredrickson, G. H.; Hawker, C. J.; Kramer, E. J., Nanoparticle Surfactants as a Route to Bicontinuous Block Copolymer Morphologies. Langmuir 2007, 23, (14), 7804-7809.

30. Kim, B. J.; Fredrickson, G. H.; Kramer, E. J., Effect of Polymer Ligand Molecular Weight on Polymer-Coated Nanoparticle Location in Block Copolymers. Macromolecules 2008, 41, (2), 436-447.

31. Thompson, R.; Ginzburg, V.; Matsen, M.; Balazs, A., Predicting the mesophases of copolymer-nanoparticle composites. Science 2001, 292, (5526), 2469.

32. Kim, B. J.; Bang, J.; Hawker, C. J.; Kramer, E. J., Effect of Areal Chain Density on the Location of Polymer-Modified Gold Nanoparticles in a Block Copolymer Template. Macromolecules 2006, 39, (12), 4108-4114.

33. Kim, B. J.; Chiu, J. J.; Yi, G.-R.; Pine, D. J.; Kramer, E. J., Nanoparticle-Induced Phase Transitions in Diblock-Copolymer Films. Advanced Materials 2005, 17, (21), 2618-2622.

34. Matsen, M. W.; Thompson, R. B., Particle Distributions in a Block Copolymer Nanocomposite. Macromolecules 2008, 41, (5), 1853-1860.

35. Yeh, S.-W.; Wei, K.-H.; Sun, Y.-S.; Jeng, U. S.; Liang, K. S., CdS Nanoparticles Induce a Morphological Transformation of Poly(styrene-b-4-vinylpyridine) from Hexagonally Packed Cylinders to a Lamellar Structure. Macromolecules 2005, 38, (15), 6559-6565.

36. Bita, I.; Yang, J. K. W.; Jung, Y. S.; Ross, C. A.; Thomas, E. L.; Berggren, K. K., Graphoepitaxy of Self-Assembled Block Copolymers on Two-Dimensional Periodic Patterned Templates. Science 2008, 321, (5891), 939-943.

37. Kang, H.; Detcheverry, F.; Mangham, A.; Stoykovich, M.; Daoulas, K.; Hamers, R.; Müller, M.; de Pablo, J.; Nealey, P., Hierarchical Assembly of Nanoparticle Superstructures from Block Copolymer-Nanoparticle Composites. Physical review letters 2008, 100, (14), 148303.

38. Zhang, Q.; Gupta, S.; Emrick, T.; Russell, T. P., Surface-Functionalized CdSe Nanorods for Assembly in Diblock Copolymer Templates. Journal of the American Chemical Society 2006, 128, (12), 3898-3899.

39. Lin, Y.; Boker, A.; He, J.; Sill, K.; Xiang, H.; Abetz, C.; Li, X.; Wang, J.; Emrick, T.; Long, S.; Wang, Q.; Balazs, A.; Russell, T. P., Self-directed self-assembly of nanoparticle/copolymer mixtures. Nature 2005, 434, (7029), 55-59.

40. He, J.; Tangirala, R.; Emrick, T.; Russell, T. P.; Böker, A.; Li, X.; Wang, J., Self-Assembly of Nanoparticle–Copolymer Mixtures: A Kinetic Point of View. Advanced Materials 2007, 19, (3), 381-385.

41. Lee, J. Y.; Shou, Z.; Balazs, A. C., Predicting the Morphologies of Confined Copolymer/Nanoparticle Mixtures. Macromolecules 2003, 36, (20), 7730-7739.

42. Gido, S.; Gunther, J.; Thomas, E.; Hoffman, D., Lamellar diblock copolymer grain boundary morphology. 1. Twist boundary characterization. Macromolecules 1993, 26, (17), 4506-4520.

43. Gido, S.; Thomas, E., Lamellar Diblock Copolymer Grain Boundary Morphology. 4. Tilt Boundaries. Macromolecules 1994, 27, (21), 6137-6144.

44. Hamdoun, B.; Ausserré, D.; Cabuil, V.; Joly., S., Composites copolymères-nanoparticules : I. Période lamellaire dans le régime des "petites nanoparticules". J. Phys. II France 1996, 6, (4), 503-510.

45. Hamdoun, B.; Ausserré, D.; Joly, S.; Gallot, Y.; Cabuil, V.; Clinard, C., New nanocomposite materials. Journal de Physique II 1996, 6, (4), 493-501.

46. Turner, M.; Maaloum, M.; Ausserré, D.; Joanny, J.; Kunz, M., Edge dislocations in copolymer lamellar films. Journal de Physique II 1994, 4, (4), 689-702.

47. Listak, J.; Bockstaller, M. R., Stabilization of Grain Boundary Morphologies in Lamellar Block Copolymer/Nanoparticle Blends. Macromolecules 2006, 39, (17), 5820-5825.

CHAPTER 2

PHASE BEHAVIOR OF THIN FILM BRUSH-COATED NANOPARTICLES / HOMOPOLYMER MIXTURES

The phase behavior of supported thin film mixtures (h~120 nm thick) of polystyrene (PS) brush-coated spherical nanoparticle and PS homopolymers is characterized by three regimes, depending on P, the degree of polymerization of the PS host, and N, the degree of polymerization of the grafted chains. Phase separation between the nanoparticles and the host chains occurs in samples for which $N < N^*$ and P>>N. Specifically, the nanoparticles segregate exclusively at the substrate and free surface in these samples, forming a trilayered structure. When P>>N and N> N*, preferential segregation of the grafted nanoparticles to the interfaces is accompanied by a structural instability (surface roughening). We identify this as Regime I and the former as Regime II. The system is miscible in Regime III (P < N and N > N*); the nanoparticles are dispersed throughout the film. There exists a region of partial miscibility that separates regimes I and III. The characteristics of Regime I are reminiscent of phase separation in polymer/polymer thin film mixtures. Regime II is reminiscent of the interfacial segregation of hard spheres in an athermal melt of polymer chains.

Reprinted with permission from Kim, J; Green P. F. *Macromolecules* **2010**, 43 (3), 1524-1529.

2.1 Introduction

Polymer nanocomposites (PNCs) are a technologically important class of materials, with structural, biomedical and optoelectronic applications.[1-3] Depending on the polymer host and nanoparticle functionalities, this class of materials may exhibit properties, such as thermal, mechanical and optical, that differ significantly from the pure polymer host, even at low nanoparticle concentrations.[3-5] The properties of PNCs are sensitive to their microstructural features, which are generally difficult to control, largely due to a complex interplay of entropic and enthalpic interactions determine the spatial distribution of nanoparticles. [4, 6] One successful strategy that has been used to control the phase behavior of these systems is to graft chains, chemically identical to the melt chains, onto the nanoparticle surfaces. In principle, control of the degree of polymerization of the grafted chains, N, the degree of polymerization of the host, P, nanoparticle core radius, R_c, composition and the grafting density, σ, would enable control of the phase behavior, and hence the properties of the system. [4, 6] The phase behavior of thin film mixtures polystyrene (PS) chain grafted gold nanoparticles with PS homopolymer chains is of particular interest in this paper.

The miscibility between brush coated nanoparticles and a melt of chains, chemically identical to the grafted chains, is determined primarily by entropic constraints. The translational entropy promotes dispersion of the spherical particles in the system. For spherical particles of diameter D in a melt, the entropy of mixing is $F_{mix} \sim (\phi/D^3) \ln\phi$, where ϕ is the volume fraction; mixing is favored with decreasing D.[7, 8] When chains are grafted onto the nanoparticles, the chains from the melt may be excluded from the brush layer at sufficiently high grafting densities. This would favor aggregation of the

particles in order to reduce the interfacial free energy associated with the brush/host chain interfaces. There is an additional driving force; attraction between the nanoparticles might occur because the melt chains confined between particles suffer a loss of conformational entropy. This loss increases with increasing P, which would have the effect of enhancing particle-particle aggregation for larger P. At lower grafting densities, and $P/N > 1$, interpenetration of the brush layer by the free host chains may occur and this would favor dispersion of the particles within the host.

The curvature of the particle surface has an important influence on the nanoparticle/host chain interpenetration, and hence miscibility. Klos et al. calculated density profiles for small nanoparticles, $R_c < N^{1/2}a$, where a is the size of a monomer, as a function of distance from particle surfaces for a wide range of values of R_c, N, σ and P.[9] It was shown that as R_c decreases, the grafted chains became less stretched, due to reduced crowding, for a constant σ and P. [10, 11] The probability of interpenetration by the host chains into the brush layer therefore increases with decreasing particle radius. Hence particle dispersion is therefore favored under these circumstances.

In thin films, miscibility is determined by additional factors that include melt/interface and nanoparticle/interface and melt /nanoparticle interactions. Recently Meli et al. showed that it was possible to disperse the nanoparticles within the polymer host and, additionally, to induce the nanoparticles to reside exclusively at the interfaces, free surface and substrate, through control of N and P.[12] Specifically, for small gold nanoparticles of $R_c = 1.8$ nm ($R_c << N^{1/2}a$), and N = 10 ($R = 2(R_c+R_N) \sim 4.5$ nm), the nanoparticles were miscible with PS host chains of P = 125, whereas for $R_c = 2.5$, N = 10 (D = 7.5 nm), the nanoparticles phase separated toward the interfaces; the interior was

virtually devoid of nanoparticles. However, when N = 480, the system was miscible largely due to interpenetration between the melt chains of P = 125 and the grafted chains. These observations were rationalized in terms of the foregoing melt/brush interaction scaling arguments.

In this study we examine the phase behavior of thin film mixtures of ϕ~2-5 wt.% gold nanoparticles (R_c = 2.5 nm), onto which PS chains of varying N were grafted, and *entangled* PS chains of varying P. A phase diagram, which shows qualitatively the location of miscible, partially miscible and immiscible regions, depending on N and P (at constant σ) is proposed for this system. We show that the phase behavior of supported thin film (h= 120±10 nm) PS brush-coated spherical nanoparticle/PS homopolymer mixtures is characterized by three regimes, depending on P and N. For P >>N > N*, complete phase separation occurs, wherein the nanoparticles segregate to both interfaces, accompanied by a structural instability. The topography of the film is characterized by spatial fluctuations in height. We will identify this as Regime I. When P>>N and $N < N^*$, phase separation occurs only normal to the substrate; the nanoparticles reside exclusively at the interfaces and the sample is characterized by a tri-layer structure. This is the regime discussed by Meli et al. and is identified in this paper as regime II. For P/N < 3 and N > N*, the system is miscible, wherein the nanoparticles are dispersed throughout the sample; this is regime III. There is a transition between regimes I and III, where nanoparticles and host chains are partially miscible. The characteristics of phase separation in Regime I are similar to those of thin film polymer/polymer blends, whereas those of regime II are similar to the phase separation of hard spheres in an athermal melt with homopolymer chains.

2.2 Experimental

The gold nanoparticles (AuNPs) were synthesized through modification of a two-phase precipitation method described elsewhere. [4, 6] The thiol-terminated PS molecules (PS-SH) were purchased from Polymer Source (M_n=1,000 g mol^{-1}, M_w/M_n = 1.4; M_n = 29,000, M_w/M_n = 1.08; M_n = 50,000 g mol^{-1}, M_w/M_n = 1.06). The synthesized particles were cleaned 10 times using methanol and toluene to remove excess ligands in the solution. After cleaning, the particles were dried, completely, and dissolved in toluene. Thermogravimetric analysis (TGA) was used to obtain the weight fractions of gold and ligands. The runs were performed by TA 2960 instrument under air at the heating rate 5 °C/min. Using the weight fractions, the average particle size, determined from scanning transmission microscopy (STEM), and the densities of each species, we were able to calculate, for the M_n = 50,000 g mol^{-1} ligand, the areal grafting density, σ = 1.44/nm^2 and R_{NP} = 27.0 nm, with the R_c (radius of core) = 2.42 (±0.61) nm and R_N (brush thickness) = 12.3 nm.[12, 13] R_{NP} was calculated from the interparticle spacing considering that chain-grafted particles are closely packed. Throughout the remainder of this paper the gold nanoparticles are identified as $AuPS_N$, where N is the degree of polymerization of the grafted chain. While results for $AuPS_{480}$ are mainly discussed, $AuPS_{10}$, $AuPS_{115}$, $AuPS_{280}$ particles have been synthesized with the sizes 2.0, 4.65 and 4.81 nm and σ = 1.44, 1.54, and 1.48 chains/nm^2 respectively.

Sample Preparation

A series of toluene/PS solutions, each containing 3 wt.% PS of different monodisperse molecular weights (M = 170,000 g/mol. (P = 1630); 400,000 g/mol. (P = 3840); 590,000 g/mol. (P = 5660); 900,000 g/mol. (P = 8640), were mixed with of

$AuPS_{480}$ nanoparticles, of concentrations 2~5 wt.%; the mixtures were stirred for at least 30 min. The solutions are then spin cast onto cleaned SiO_x/Si substrates to form films with thicknesses of approximately 110-130 nm. The thicknesses of the samples were determined using spectroscopic ellipsometry (M-44, J.A Woollam Co.).

Samples were annealed in a vacuum oven at 65 ºC for a day for solvent evaporation and then annealed in compressed CO_2 (T = 50 ºC, P = 13.8MPa) in a high-pressure cell. The annealing procedure is described in detail elsewhere.[14] Super critical-CO_2 is a poor solvent for PS and it plasticizes the mixture enabling the system to reach equilibrium. It is used here in order to avoid heating the sample to very high temperatures to achieve a reasonable degree of plasticization and maintain thermal stability of grafted chains. Additionally sc-CO_2 annealing is more controllable than liquid solvent annealing.

Transmission electron microscopy (TEM), using a JEOL2010F in scanning mode (STEM), was used to characterize the lateral distribution of the nanoparticles in the samples. STEM was used to characterize the Au NP distribution throughout the film before and after annealing. The STEM samples were prepared first by spin casting the solutions onto a glass slide and then floating the resulting film from the slide onto a bath of distilled water. The films were then deposited from the water bath onto silicon nitride windows (SPI Supplies) for STEM analysis. Images were taken using high annular angle dark field (HAADF) detector (Z-contrast) applying accelerating voltage of 200 KV.

Depth profiles of AuNPs within the PS films were acquired using DSIMS, performed by Dr. Tom Mates at the University of California, Santa Barbara, using Physical Electronic 6650 Quadropole instrument. The combination of STEM and SIMS

enabled determination of the spatial distribution of nanoparticles in the films. Topographical analyses were determined using Autoprobe CP scanning force microscopy (SFM), operating in the contact mode. Information about RMS roughness (R_q) and kurtosis were extracted by WSXM software in order to characterize the topography. The characteristic lengths were obtained from the power spectrum density (PSD), which characterizes the surface fluctuations, as a function of frequency.

2.3 Results and discussion

The SFM measurements indicate that the $AuPS_{480}/PS_{8640}$ films, h~120 nm, exhibited surface roughening, as shown in Figure 2.1a for P = 8640 and N = 480. The roughening increased after annealing (Figure 2.1b). The depth profiles of the gold particles in Figures 2.1a and 1b exhibit maxima at the free surface and at the polymer/substrate interface. These maxima represent enhanced interfacial segregation of brush coated Au nanoparticles. This segregation may be understood in analogy to multi-arm star molecules at interfaces; chains tethered to the particles suffer less of an entropy penalty upon segregation to an interface than the linear host chains. This relieves frustrated packing in the bulk; it also relieves the entropic restrictions associated linear chains at flat interfaces. The surface roughening is similar to the behavior of phase separated polymer/polymer thin film mixtures. [15, 16]

Characteristics of the structure of the phase separated samples will be discussed below, but in the meantime we note that samples for which P > 8N exhibit this behavior: preferential nanoparticle segregation to the interfaces accompanied by a structural instability. We will associate this behavior with Regime I. The structural instability is

suppressed in the range of N and P where 3N < P < 8N. However, while the instability is suppressed, phase separation still occurs; the nanoparticles segregate exclusively to the interfaces. This behavior is associated with Regime II and was identified by Meli et al.; it is analogous to phase separation between the homopolymers and athermal hard sphere nanoparticles. When P < 3N, the system is miscible; this behavior is associated with Regime III. A "phase diagram" characterizing the behavior of this system, depending on N and P, will be discussed later.

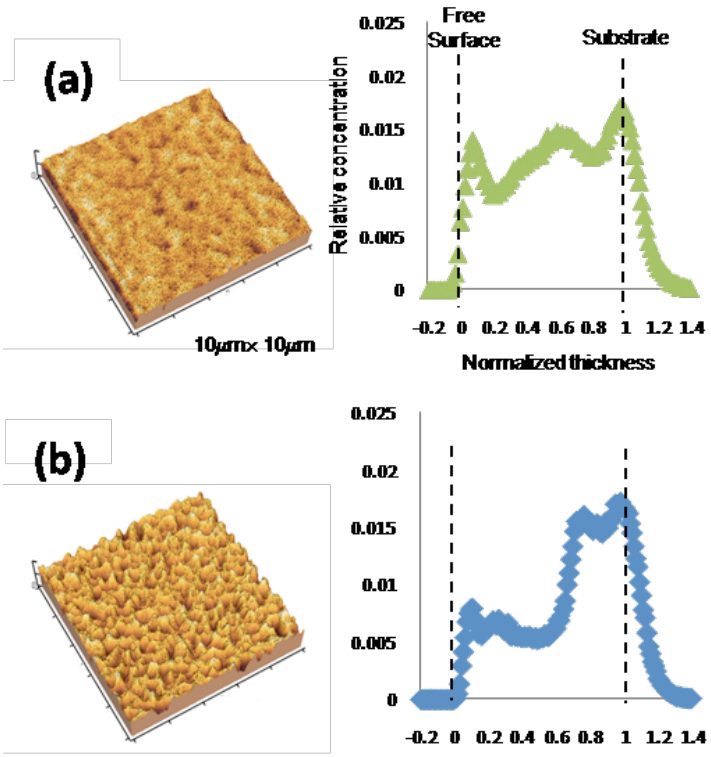

Figure 2.1 Topographies and corresponding depth profiles of Au for a 4 wt.% $AuPS_{480}/PS_{8640}$ films are shown here for: (a) as-cast films (b) CO_2 annealed films at 50 ºC, 13.8MPa for 4320min.

The features of phase separation in Regime I are now discussed. In-plane distributions of AuNPs in hosts of different P, and fixed N = 480, for as-cast films are

shown in Figure 2.2. The particle-rich and particle-poor regions are evident from the images. The images indicate that as P increases from 1630 (=3.4N) to 8640, the particles aggregate and the extent of aggregation increases with increasing P.

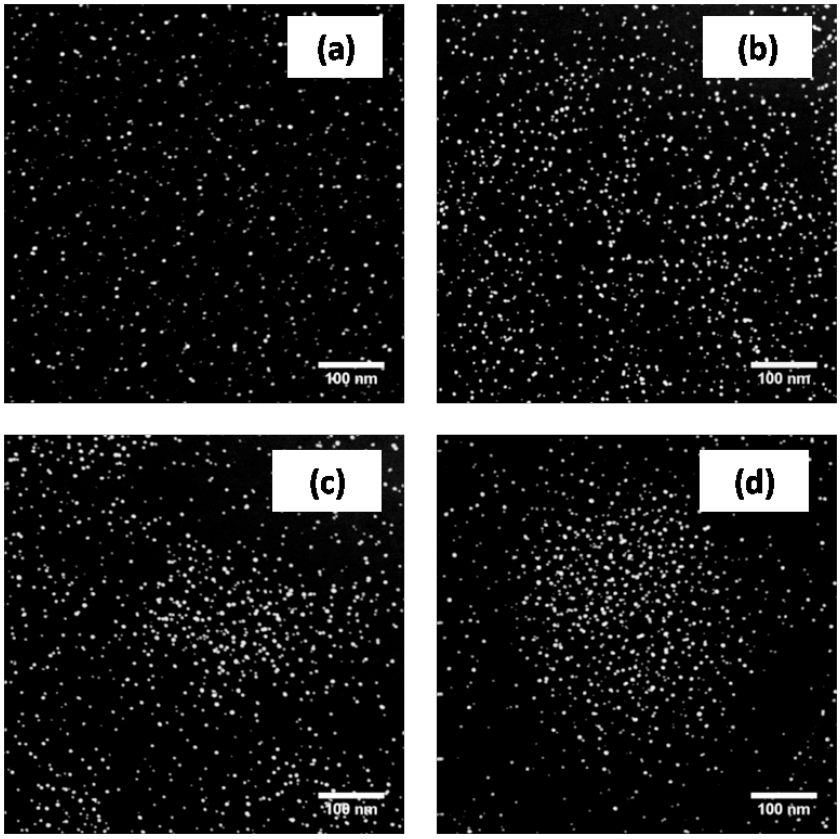

Figure 2.2 STEM images are shown for 4 wt.% $AuPS_{480}$ mixed with PS hosts different molecular weights: (a) M_n (PS)= 170 kg/mole (P=1630) (b) M_n (PS)= 400 kg/mole (P = 3840) (c) M_n (PS)=590 kg/mole (P = 5660) (d) M_n (PS)=900 kg/mole (P=8640).

Information about phase separation of the system may be learned from an analysis of the number of nanoparticles throughout different regions of the sample. The average number of particles in the particle-rich phase, N_{par}, and in the polymer-rich phases, N_{poly}, were determined for each sample by counting the number of particles in several selected areas of each sample; the results are plotted in Figure 2.3. In this Figure, $r=N_{par}/N_{poly}$; r~1.0, increases from P~3840, to r~3.3, for P~8640 (Figure 2.3). P~1630 denotes the

transition from miscibility to partial miscibility, with increasing P; the system is immiscible for P> ~ 4000. This transition miscibility to immiscibility occurs within the range of 3N < P < 8N.

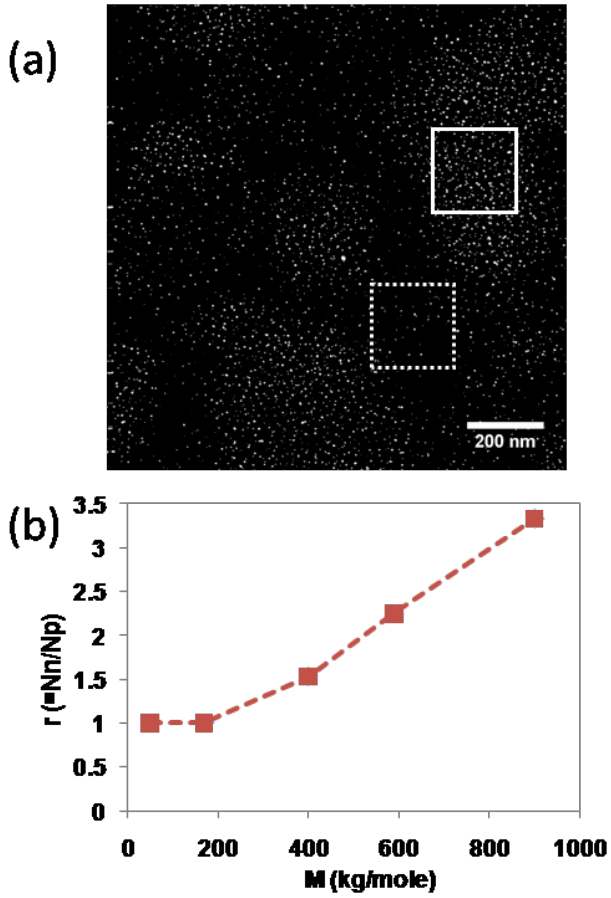

Figure 2.3 The ratio $r=N_{par}/N_{poly}$, is potted as a function of the molecular weight of the PS host chains. 200x200 nm^2 areas were analyzed throughout different regions of the samples. The number of particles at the boundary is $(N_{par}+N_{poly})/2$.

Surface topographies of the $AuPS_{480}$ /PS samples were also examined, using the power spectrum density analysis, to learn more about phase separation (Figure 2.4). The PSD exhibited much larger maxima for the sample containing 4% AuPS480/PS8640 than the sample containing 2% $AuPS_{480}/PS_{8640}$, revealing a much larger degree of phase separation (Figure 2.4a). Further, the PSD maxima and the average wavelength of the

fluctuations in the 4% $AuPS_{480}/PS_{5660}$ sample were appreciably smaller than that of the 4% $AuPS_{480}/PS_{8640}$ sample, reflecting a much smaller degree of phase separation. This observation is consistent with the data in Figure 2.2.

The RMS roughnesses of samples containing 2% and 4% AuPS480/PS are shown in Figure 2.4b. The RMS roughness increased with increasing P, reflecting increasing phase separation. The sample with the higher concentration exhibited larger surface fluctuations, again reflecting increasing phase separation. Note that for host $P < 4000$, the surfaces are effectively smooth. However for greater values of P, the surface fluctuations increased rapidly. Again, this latter regime is associated with enhanced lateral phase separation.

Based on the AFM and STEM data, the regions of high nanoparticle concentration (aggregation) are associated with the peak locations of the surface topographies. The development of the topography reflects phase separation of the system, analogous to polymer/polymer phase separation in thin films; phase separation becomes significant at large P. The final state of these sample is one in which an excess of nanoparticles resides at both interfaces. The peaks and valleys in the topographies represent an attempt by the system to minimize the area of contact between the long chain grafted (N=480) nanoparticles and the homopolymer chains, subject to the interfacial constraints. Finally, with regard to experimental details, we note that the state of dispersion of the particles did not change significantly from the in-plane view after annealing for longer times, up to 4320 min, as one might anticipate if the phase separation were nearly complete.

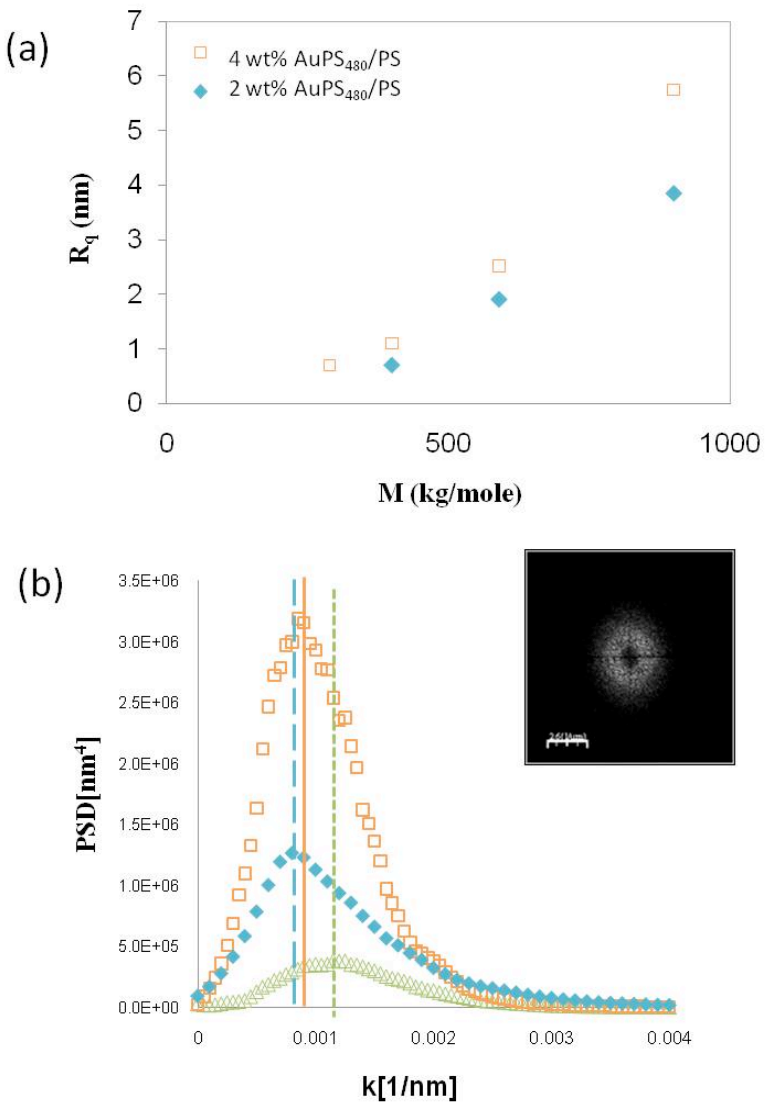

Figure 2.4 (a) The RMS roughness (R_q) vs M. are plotted for various host chain lengths. (b) Power spectrum densities of different samples (orange square: 4% $AuPS_{480}/PS_{8640}$, blue diamond: 2% $AuPS_{480}/PS_{8640}$, green triangle: 4% $AuPS_{480}/PS_{5660}$) are shown here. The lines represent the characteristic wave vector for each mixture.

The distinction between phase separation phenomena in regimes I and II are clearly illustrated in Figures 2.5 and 2.6. It is clear from the STEM images in Figures 2.5a, b and c that as N increases, for these mixtures containing PS of P=8640, the particle

aggregation increases. The SIMS profiles show that for smaller N, the nanoparticles reside exclusively at the interfaces. With increasing N, there is evidence of nanoparticles in the interior of the sample. However, the AFM images in Figure 2.6 provide the best insight into the actual phenomenon. The surface of the sample of lowest N is relatively smooth, whereas with increasing N, the surfaces exhibit significant height fluctuations.

The images in Figures 2.5 and 2.6 show that for small N (N=10), the particles reside exclusively at the interfaces according to the DSIMs profile in Figure 2.5a and the surfaces are smooth (Figure 2.6a). However, at large N, a structural instability accompanies the interfacial segregation, reflecting the behavior of polymer/polymer thin film systems that undergo phase separation.

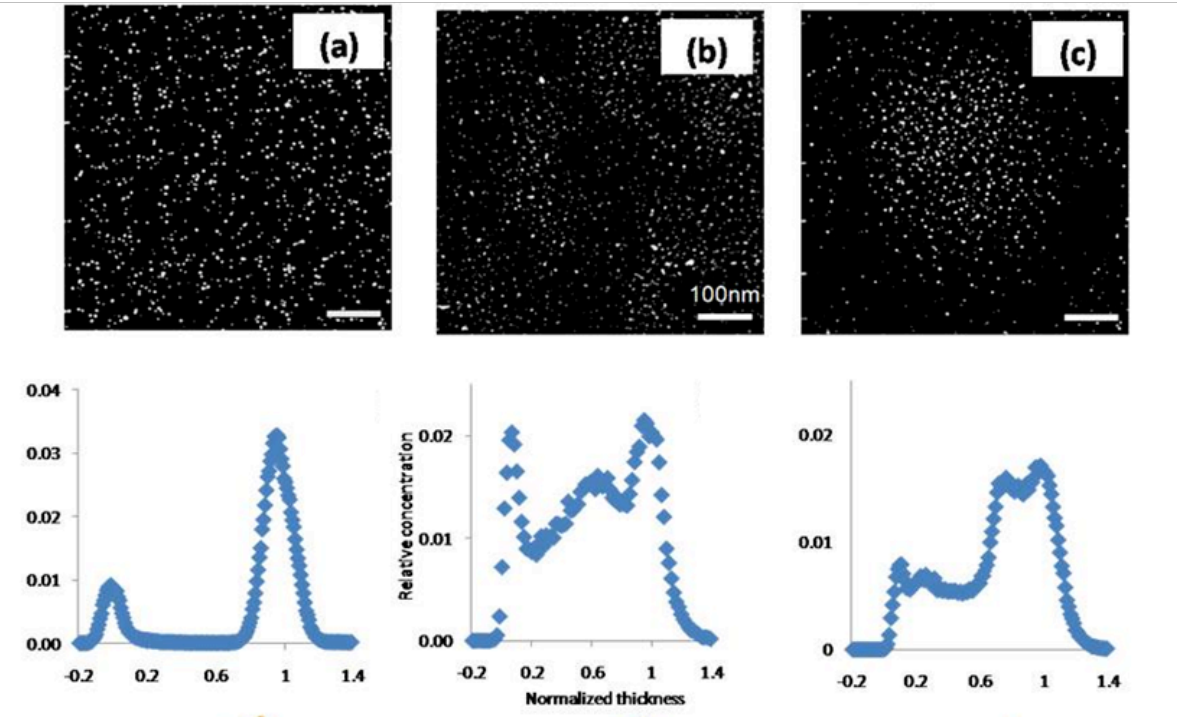

Figure 2.5 STEM images and depth profiles are shown here for samples in which P = 8640 and: (a) N = 10 (b) N = 280 (c) N = 480. All samples contained 4 wt.% Au.

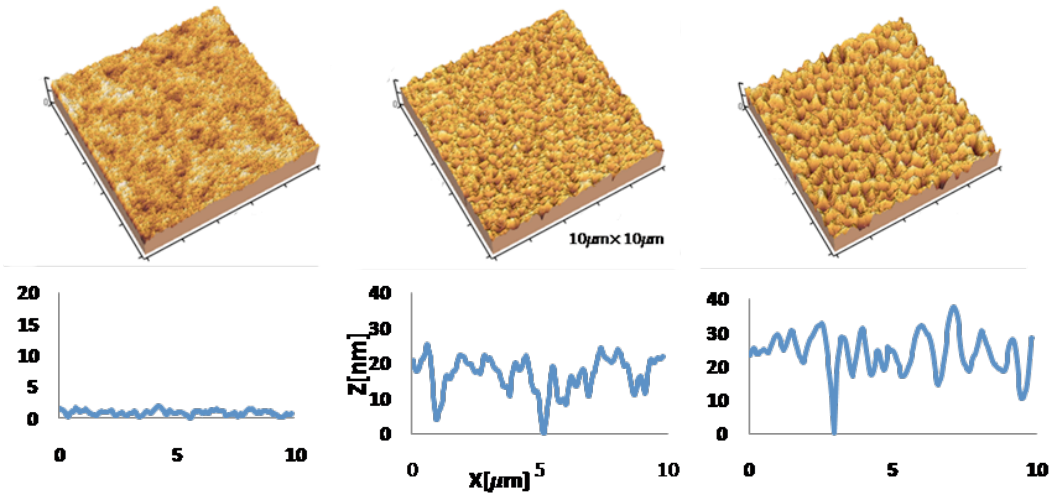

Figure 2.6 The corresponding topographies are shown here for the samples in Figure 2.5.

Parenthetically, for P/N >> 1, one might anticipate that the nanoparticles would be miscible with the melt chains, particularly for sufficiently small values of N and Rc. Under such conditions particles may be incorporated within the host without much loss of conformational entropy. Such a case was observed by Meli et al. when particle diameter was DNP = 4 nm (Rc = 0.9 nm) and P = 8640. In our experiments, nanoparticles were larger, D = 10 nm and this behavior was not observed.

The N-dependence of the phase behavior of $AuPS_N/PS$, described above is associated with three competing entropic contributions to the free energy. While grafted chains pack densely around the particle core to minimize the entropic stretching energy, the grafted chains reside in more stretched state for smaller N, in order to accommodate the high grafting density ($\sigma > 1$) near the surface of the core. Therefore with decreasing N, at constant σ, the host chains are excluded from the brush layer. Consequently, the particles exhibit a larger tendency to segregate to minimize the interfacial free energy. Segregation is further favored, as mentioned earlier, because confinement of the chains between nanoparticles reduces the conformational entropy of the host chains; this effect

increases with increasing P. The competing effect is that the host chain/brush layer interfacial tension decreases with decreasing N (and decreasing RNP), which favors miscibility, and hence dispersion. Therefore the suppression of the instability is not unexpected with decreasing N, at constant P.

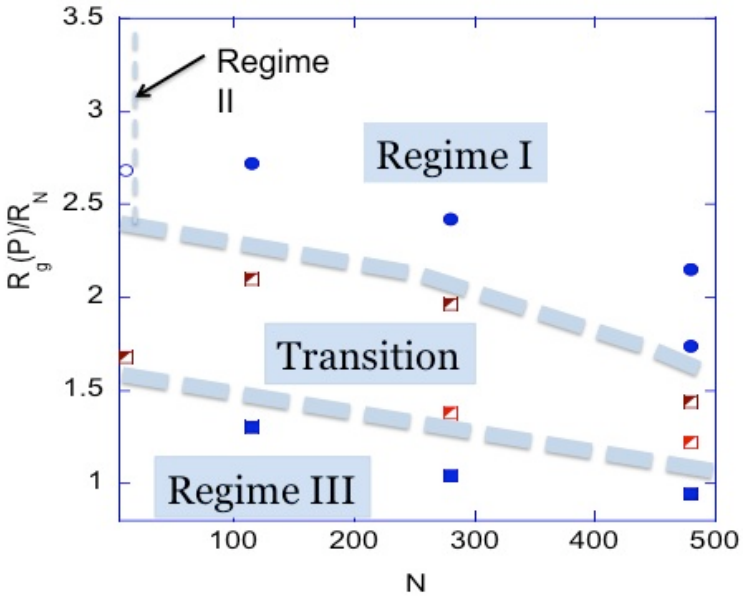

Figure 2.7 Phase diagram, represented by $R_{g,}(P)/R_N$ (Radius of gyration of host over brush thickness) versus N, is shown here for samples characterized for various values of N and P.

A "phase" diagram was developed to qualitatively delineate the different regimes based on N and P at constant σ, Figure 2.7. The broken lines in the diagram show qualitatively where the different regimes of phase separation, miscibility and partial miscibility occur. For large values of N and P, the system is incompatible and phase separation occurs in a manner similar to phase separation in polymer/polymer systems (Regime I). When N is sufficiently small ($N<N^*=10$) the behavior is that of hard particles

segregating to the interfaces to minimize the free energy of the system. There is a transition regime of partial miscibility between Regime I and Regime III, where the system is miscible. We anticipate that the quantitative aspects of the phase diagram are specific to the polymer and the molecular weights. However, we expect that the qualitative aspects of this phase diagram should be general, assuming that the nanoparticle is not too small. We now make final comments regarding the phase separation in regime I and II by drawing an analogy with the behavior of homopolymer/micelle systems. Semenov et al. proposed a theory of phase behavior of a linear homopolymer chain, A, and copolymer, A-B, spherical micelles (A-B/A) mixture.[17, 18] The relative sizes of N_{A-B} to N_A, determines, in part, the size of the micelle, and the phase stability. When $N_{A-B} >> N_A$, separation into A-B micelle-rich and homopolymer-rich phases occurs due to an attraction between micelles. For thin film A-B micelle/A homopolymer mixtures, micelles segregated towards the interfaces.[17, 19]

The attraction between the micelles was predicted to increase with the size of the micelles.[17, 19, 20] Though this comparison between micelle/homopolymer mixtures was qualitative, one may qualitatively anticipate the phase behavior and structure of AuPS/ PS mixtures based on parameters, N, P, and D ($2R_c + 2R_N$). The SIMS image in Figure 2.1 shows four maxima, each of which is associated with a layer of brush-coated nanoparticles. The diameter of the nanoparticles is approximately D = 30 nm and the depth resolution of the SIMS measurement is just under 20 nm. The two peaks near the substrate correspond to the spacing of two layers of nanoparticles. It is difficult to make the same assessment of the free surface due to the instability. Nevertheless, the spacing between the peaks near the free surface and the substrate is also consistent with two

layers of grafted nanoparticles. The central region corresponds to homopolymer chains.

The theory of Semenov indicates that the attraction of micelles, and by extension our brush coated particles, should be strong. This would be consistent with the interpretation of the maxima in the SIMS data. Finally we note that with regard to athermal mixtures of stars and linear chains, where only differences in architecture are considered, Fredrickson et al. predicted that they are intrinsically, thermodynamically less stable than linear-linear athermal mixtures.[21] This prediction is consistent with our findings in regime I.

2.4 Conclusions

Phase separation of thin film brush-coated NPs/homopolymer mixture was systematically studied by changing ϕ, N and P, at a fixed brush density and nanoparticle core radius. We showed that the phase behavior of supported thin film PS brush-coated spherical nanoparticle/PS homopolymer mixtures is characterized by three regimes, depending on P and N. Regime I is characterized by phase separation between the nanoparticles and the host chains normal to the substrate, accompanied by a structural surface instability. With decreasing P, at fixed N, the system became fully miscible for $P/N < 3$ (Regime III). The system was partially miscible between regimes I and III. Regime II was observed, when $N < N^*$ and sufficiently large P; phase separation occurred normal to the substrate, but the instability was suppressed. Characteristics of regime I are reminiscent of the behavior of thin film polymer/polymer mixtures. The behavior in Regime II is characteristic of the behavior of hard spheres separating from an athermal mixture with polymer chains.

2.4 References

1. Jia, J., et al., A Method to Construct a Third-Generation Horseradish Peroxidase Biosensor: Self-Assembling Gold Nanoparticles to Three-Dimensional Sol-Gel Network. Analytical Chemistry, 2002. 74(9): p. 2217-2223.

2. Yu, G., et al., Polymer Photovoltaic Cells: Enhanced Efficiencies via a Network of Internal Donor-Acceptor Heterojunctions. Science, 1992. 270(5243): p. 1789-1791.

3. Bhattacharya, P., S. Ghosh, and A.D. Stiff-Roberts, Quantum dot opto-electronic devices. Annual review of materials research, 2004. 34(1): p. 1.

4. Abraham, A., M. Luciana, and G. Peter F, Glass transition of polymer-nanocrystal thin film mixtures: role of entropically directed forces on nanocrystal distribution. Nano letters, 2008. 8(8): p. 2271.

5. Mackay, M.E., et al., Nanoscale effects leading to non-Einstein-like decrease in viscosity. Nature materials, 2003. 2(11): p. 762.

6. Oh, H. and P.F. Green, Polymer chain dynamics and glass transition in athermal polymer/nanoparticle mixtures. Nature materials, 2009. 8(2): p. 139-143.

7. Lee, J.Y., Z.Y. Shou, and A.C. Balazs, Predicting the morphologies of confined copolymer/nanoparticle mixtures. Macromolecules, 2003. 36(20): p. 7730-7739.

8. Lee, J., G. Buxton, and A. Balazs, Using nanoparticles to create self-healing composites. The Journal of chemical physics, 2004. 121(11): p. 5531.

9. Xu, J., Morphology and interactions of polymer brush-coated spheres in a polymer matrix. Journal of polymer science. Part B, Polymer physics, 2006. 44(19): p. 2811-2820.

10. Klos, J. and T. Pakula, Interaction of a spherical particle with linear chains. II. Chains end-grafted at the particle surface. The Journal of chemical physics, 2003. 118(16): p. 7682.

11. Klos, J. and T. Pakula, Computer Simulations of Chains End-Grafted onto a Spherical Surface. Effect of Matrix Polymer. Macromolecules, 2004. 37(21): p. 8142.

12. Meli, L., A. Arceo, and P.F. Green, Control of the entropic interactions and phase behavior of athermal nanoparticle/homopolymer thin film mixtures. Soft Matter, 2009. 5(3): p. 533-537.

13. Kim, B.J., G.H. Fredrickson, and E.J. Kramer, Effect of Polymer Ligand Molecular Weight on Polymer-Coated Nanoparticle Location in Block Copolymers. Macromolecules, 2008. 41(2): p. 436.

14. Meli, L., et al., Templating of Gold Nanocrystals in Micellar Cores of Block Copolymer Films. Macromolecules, 2007. 40(18): p. 6713-6720.

15. Jandt, K.D., et al., Transient Surface Roughening of Thin Films of Phase Separating Polymer Mixtures&#x2020. Langmuir, 1996. 12(15): p. 3716-3720.

16. Wang, H. and R.J. Composto, Thin film polymer blends undergoing phase separation and wetting: Identification of early, intermediate, and late stages. The Journal of chemical physics, 2000. 113(22): p. 10386.

17. Semenov, A.N., Theory of Diblock-Copolymer Segregation to the Interface and Free Surface of a Homopolymer Layer. Macromolecules, 1992. 25(19): p. 4967.

18. Semenov, A.N., Phase-equilibria in block copolymer homopolymer mixtures. Macromolecules, 1993. 26(9): p. 2273-2281.

19. Esselink, F.J., et al., Formation and structural ordering of micelles of block copolymers in a thin-film-homopolymer matrix. Physical review. B, Condensed matter, 1993. 48(18): p. 13451.

20. Dai, K.H. and E.J. Kramer, Molecular Weight Dependence of Diblock Copolymer Segregation at a Polymer/Polymer Interface. Journal of polymer science. Part B, Polymer physics, 1994. 32(11): p. 1943.

21. Fredrickson, G.H. Liu, A.J., Bates, F.S. Macromolecules 1994, 27, (9), 2503.

CHAPTER 3

TAILORING REFRACTIVE INDEX OF THIN FILM POLYMER NANOCOMPOSITES BY THE CONTROL OF NANOPARTICLE DISTRIBUTION

3.1 Introduction

The functionalities (e.g., optical, magnetic, mechanical) of polymer nanocomposites (PNCs) are influenced by the chemical compositions of the polymer and by the type, size and spatial organization, of nanoparticles (quantum dots, fullerenes, and metallic crystals, etc.) within the polymer host. The geometrical shape, interparticle spacing, and different types of entropic and enthalpic interactions between nanoparticles (NP) and between the nanoparticles and the polymer chains [1, 2] and the external interfaces. For example, optical properties of the polymer may change appreciably when mixed with metallic nanoparticles of different sizes and shapes, particularly for metal NPs possessing average sizes below 100nm) [3-5]. Noble NPs such as gold, silver and copper contributes to strong absorption and scattering of the light. This is due to a surface plasmon resonance (SPR) effect, arising from the collective oscillation of conduction electrons induced by the light. The absorption of light is evident from the color change in solutions or in films of polymer/NP mixtures. The magnitude of the surface plasmon resonance effect is controlled by the interparticle distance and the relative permittivity (dielectric constant)

of polymer, as well as size and shape of particles [6-11]. Applications of the SPR effect include biological sensors, surface-enhanced spectroscopies and photovoltaics [8, 12-14].

In this study, we have incorporated Au NPs, onto which polymer chains are grafted onto the surface, enabling the fabrication of polymers with very stable structures. Functionalizing the surface of NPs is one of the most common methods to control nanoparticle/polymer compatibility and to control the spatial distribution of NPs. This study differs from previous studies, where the SPR effect was studies under conditions where the NPs of varying grafted chain sizes and thus interparticle spacing where placed on a hard substrate [5, 11, 15]. In this study, however, NPs with different grafted chain sizes were incorporated into a polymer hosts of varying chain lengths; this enabled tailoring of the spatial distribution of nanoparticles and hence the optical properties of the mixture. With this, we have demonstrated the effect of interparticle spacing and NP size on the SPR band in homopolymer thin film.

Following our earlier study, NPs were functionalized with polystyrene (PS) ligands and incorporated into PS host; this system is an athermal mixture because the structure is determined largely by the host/brush interactions. Combinations of the degree of polymerization of the host, P, and the degree of polymerization of the ligand, N, grafting density and core size, D_{core} were key factors that determined the miscibility of NPs to the host. Two distinctive systems-homogeneous and phase separated thin film mixtures- created by varying N, P and D_{core}, together with an additional control of film thickness, h and the NP concentration. Apart from the applications abovementioned, thin film phase separated mixtures may have its own merit of enhancing light absorption and

scattering in optical devices as anti-reflection coating for example, with multiple refractive indices inherited in the film [16-18].

Once we characterized the film structures, UV-Vis and spectroscopic ellipsometry (SE) were used to characterize the optical spectra and correlate to the morphology of thin film PS-coated/polystyrene mixtures. While UV-Vis measures the light absorption of the film, SE measures the reflectance ratio between s-polarized light and p-polarized light, which is sensitive to a small shift in refractive index and optical anisotropy within the film. The SE measurement, therefore, was conducted to directly measure the optical properties in order to reveal the nature of NP distribution in thin film polymer host. In these measurements, films containing homogeneous distributions of NPs and others where the NPs preferentially resided at the external interfaces (phase separated), were analyzed using optical models that appropriately described the structure.

3.2 Experimental

3.2.1 Materials and sample preparation

Gold nanoparticles (Au NPs) were synthesized using the two-phase arrested precipitation method reported by Brust et al [19]. Thiol-terminated polystyrene molecules (PS-SH) of number-average molecular weight M_n = 1100 g/mol (M_w/M_n = 1.12), 3000 g/mol (M_w/M_n = 1.07), and 5300 g/mol (M_w/M_n = 1.1), purchased from Polymer Source, Inc., were then grafted onto the surfaces of the nanoparticles. The details of our synthetic procedures are described in earlier publications. The synthesized particles were cleaned at least 10 times using methanol and toluene to remove excess ligands and salts in the solution. Thermogravimetric analysis (TA 2960) was used to estimate the grafting density,

σ with the weight fractions between gold and ligands, densities of each component and the runs were performed under air at a heating rate of 5 °C/min.

The diameters of the NP cores, d_{core}, and the brush thicknesses, h_{brush}, were determined from scanning transmission electron microscopy (STEM) images of the samples, obtained using a JEOL 2010F electron microscope operated at 200 kV. The average particle sizes were determined by measuring the diameters of groups more than 300 NPs in the images. Three sets of grafted nanoparticles were prepared: (1) Au(5)-PS is a nanoparticle of d_{core} = 4.6 ± 1.2 nm and $d_{NP} = d_{core} + 2h_{brush}$ = 8.6 ± 1.1 nm; N = 50, σ = 1.0 chains/nm^2; (2) Au(2)-PS is a nanoparticle of d_{core} = 1.8 ± 0.5 nm; d_{NP} = 4.5 ± 1.1 nm, N = 10 and σ = 1.9 chains/nm^2; (3) Au(7)-PS is a nanoparticle of d_{core} = 7.0 ± 1.4 nm; d_{NP} = 12.8 ± 1.5 nm, N = 30 and σ = 1.9 chains/nm^2.

Polystyrenes (PS) of number-average molecular weight M_n = 7500 g/mol and M_n = 170000 g/mol and polydispersity, $M_w/M_n \leq 1.06$ were purchased from Pressure Chemical Inc. Homogeneous solutions containing well-defined concentrations of the PS and the nanoparticles were prepared using toluene as a solvent. The solutions of PS/Au(d_{NP})PS$_N$ (N = 10, 30, 50) mixtures were spin-casted on to cleaned silicon substrates with native oxide layer (~14 Å) then dried in vacuum oven at 60 °C for 16 ~24 hrs to remove excess solvent in the film.

3.2.2 Structural characterization

The morphologies of the thin film PNCs, the Au NP distributions and the roughness of the sample were determined using a combination of STEM, dynamic secondary ion mass spectrometry (DSIMS) and scanning force microscope (SFM). The

samples examined using STEM were prepared first by spin-casting their solutions onto a glass slide and then floating the film from the slide onto a bath of distilled water. The films were then transferred onto a Si_3N_4 grid and subsequently dried by annealing them in vacuum at 60 °C for 16 h. DSIMS was performed at University of California Santa Barbara by Tom Mates using a Physical Electronics 6650 Quadropole instrument used to determine the depth profile of Au within PS films. SFM measurements of the films were performed using the MFP-3D (Asylum Research, Inc.) microscope, in tapping (AC) mode with silicon cantilevers (Nano and More Inc., spring constant 20 N/m and resonant frequency of 130 kHz) to verify the surface roughness of the film. RMS roughness turned out to be below 1.5 nm for all the samples.

3.2.3 Optical characterization

The absorption spectra were measured using a Varian Cary 50 Bio. The complex refractive index (RI) was characterized by multi-variable angle spectroscopic ellipsometric (M-2000D with the NIR extension, J.A.Woollam Inc., Co.) and CompleteEASE software (J.A.Woollam Inc., Co.). Spectroscopic ellipsometry (SE) data is acquired from the change in polarization of light reflected by the film with the wavelength range of 193-1690 nm and incident angle range of 45-80 degrees. Ellipsometry measures the reflectance ratio, ρ, between p- and s-polarized light which is parameterized by ψ and Δ:

$$\rho = \frac{r_p}{r_s} = \tan(\psi)\, e^{i\Delta} \tag{3.1}$$

To determine the film thicknesses, *h*, of the nanocomposite samples, transparent wavelength range 900-1690 nm was initially selected and fitted by the Cauchy model.

Then the range was expanded to 350-1690 nm rest of wavelength to fit NP coverage and optical spectra in effective medium approximation (EMA) model, which will be discussed more in detail. The merit function used to assess the quality of fitting the measured data was mean-squared error (MSE) between measured data and calculated data by the established model:

$$\mathrm{MSE} = \frac{1}{2N-M}\sum_{j=1}^{N}\left[\left(\psi_j^{\mathrm{mod}} - \psi_j^{\mathrm{exp}}\right)^2 + \left(\Delta_j^{\mathrm{mod}} - \Delta_j^{\mathrm{exp}}\right)^2\right] \quad (3.2)$$

where N is the number of (ψ and Δ) and M is the number of model parameters.

One should proceed with caution when constructing a model and fitting raw data of spectroscopic ellipsometry (SE) because low MSE does not necessarily mean the fitted data is close to the actual physical property. The complexity usually arises from trying to fit too many parameters at the same time. It would be ideal to have a sample with a known structure to attain proper optical constants as a function of wavelength. Step-by-step fitting procedures will be shown in more detail in Appendix D.

Detailed models used to fit ψ and Δ were developed based on the structural characterization, based on DSIMS and STEM data. First, we consider homogeneous composite film for all the samples and build EMA layer that consists of two materials, i.e., Cauchy for PS and bulk Au, on top of substrate layer (Figure 3.1a). To characterize phase separated mixtures, however, it would be unphysical to treat as a single RI since the film contains multiple refractive indices. Therefore a single EMA layer was divided into three EMA layers, which mimic the actual structure (figure 3.2); repeated refining of the model allowed the MSE to be minimized. Since the number of fitting parameters tripled by dividing the layers, we limited the parameters by fixing film thicknesses of each layer based on the h_{total} and h of two NP-rich layers (determined by DSIMS). The volume

fraction of NPs was set to reasonable value 0 for middle layer to further reduce the number of variables. After fitting the particle coverage of NP-rich layers and constants for Cauchy model, the thickness and NP volume fraction of all the layers were re-fitted.

The oscillator models were then built using the optical spectra obtained by EMA model. This is a reasonable procedure since bulk Au permittivity should be re-evaluated since the model does not respond to different particle size and interparticle spacing [20]. Both EMA and Lorentz oscillator models consist of dielectric functions that only describe a homogeneous sample. The simplified Lorentzian equation can be described as the following:

$$\tilde{\varepsilon}(\omega) = \varepsilon_{\infty} - \frac{\omega_p^2}{\omega^2 - i\Gamma\omega} \tag{3.3}$$

In this equation, ω_p is the bulk plasma frequency, and Γ is the free electron relaxation frequency, which describes the peak width. An improvement in MSE was evident; it agreed physically with other theoretical and experimental data. In Figure 3.1, the peak width and location for Au(5)PS_{50}-PS_{70} sample were slightly adjusted after fitting with Lorentz oscillator model; this led to an improvement of the MSE model by 3~5. Results for 2 nm NP embedded film initially displayed the most improvement in MSE, from 18 to 6 by fitting with Lorentz model. Real and imaginary part of complex refractive index, n & k, follows Kramer-Kronigs relation showing the dependence between dispersive and absorptive properties of the sample [21].

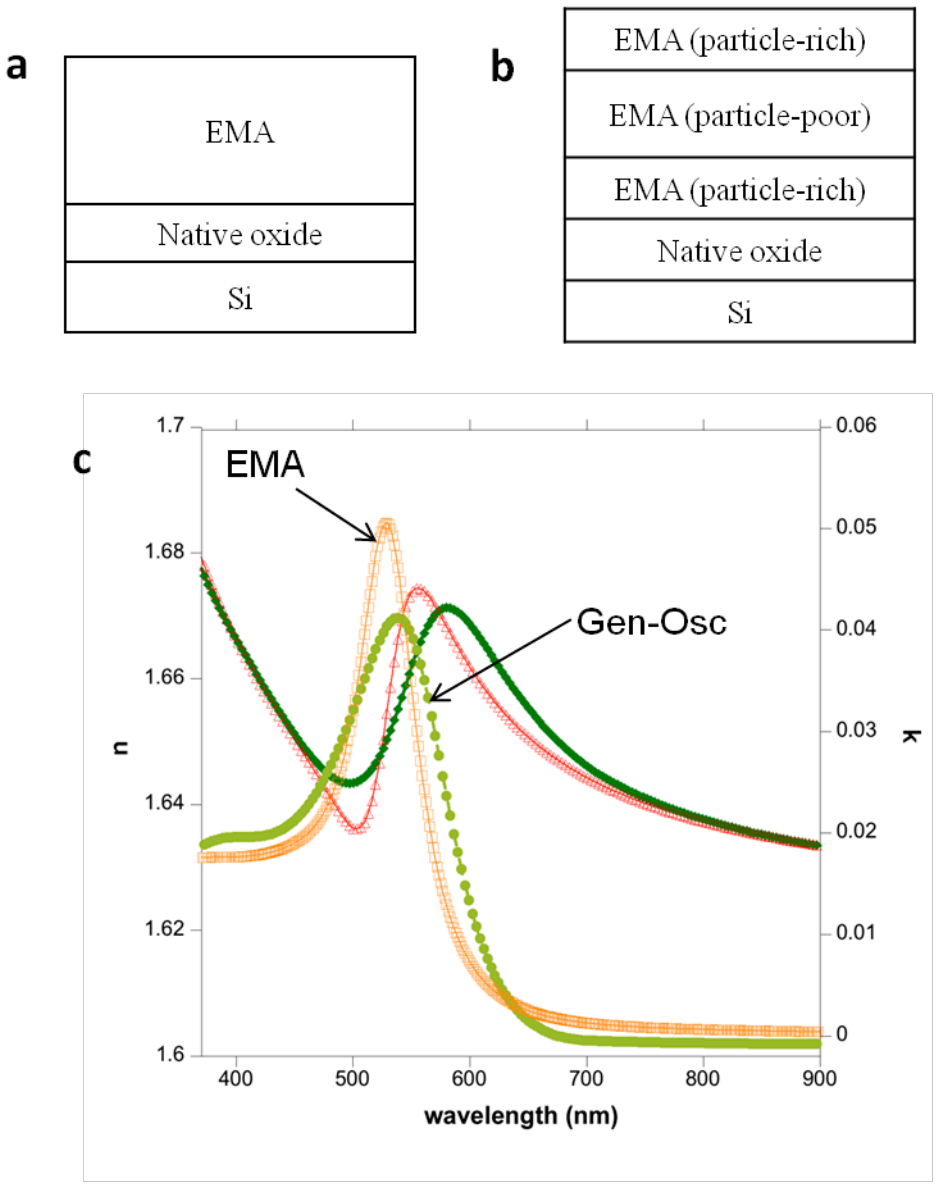

Figure 3.1 (a) and (b) are effective medium approximation (EMA) models for homogeneous (single layer) and phase separated mixtures (tri-layer) (c) An example (20 wt% Au(5)PS_{50}/PS_{70} sample) of fitting ψ and Δ data with EMA model (initial model) and General-Oscillator model (parameterized complex refractive index, n & k from EMA model).

3.3 Results and Discussion

Using the strategies described below, thin film samples contain different nanoparticle distributions: (1) homogeneous distribution and (2) nanoparticles located only at the external interfaces. The nanoparticle distributions of these samples, determined using scanning transmission electron microscopy (STEM) and dynamic secondary ion mass spectrometry (DSIMS) are shown in Figure 3.2. The most important question is to what extent does information about the refractive index (RI), as determined by SE, of thin film PNC reflect the NP distribution.

The NP distributions in the samples were obtained by controlling the experimental variables, N, P, the nanoparticle size and the grafting density of the nanoparticle. Specifically, to obtain phase separated mixtures consist the variables were N = 30, P = 1630 and D_{core}= 7nm. In this situation, the grafting density is sufficiently high and P>>N, so the so-called dry-brush condition is met. The particle is also sufficiently large, comparable to, the radius of gyration of the host chains, that the free energy is minimized when the nanoparticles are located at the external interfaces. The additional driving forces, the van der Waals forces between the nanoparticles and the substrate, are largely responsible for the segregation of a fraction of the nanoparticles to the substrate. When a fraction of the NPs are at the free surface the host chains gain translational entropy. We note further that the particles form close packed structures, local two-dimensional crystalline ordering (Figure 3.2a and 3.2b), at the interfaces, a consequence of the segregation. This structure is obtained regardless of the film thickness h or Au weight fraction □.

The homogeneous distributions were achieved by changing N and D_{core}. When the

nanoparticle size is decreased to D_{core}= 2 nm (Figure 3.2d), smaller the size of the host chains, NPs arranged to form a more uniform distribution throughout the films Figure 3.2f (dashed curve). In this case, the translational entropy became more important; moreover, because of the small size of the nanoparticles relative to the host chains, the conformational entropy (stretching energy) of the host chains is reduced considerably. [1] The second strategy for achieving a homogeneous mixtures (Figure 3.2f) is to increase the value of N (N = 50), decrease P (P= 70) and the particle size from (D_{core}= 7nm to 5 nm. These strategies enabled the "wet brush" condition to be met, i.e., host chains intermix with the brush (Figure 3.2f).

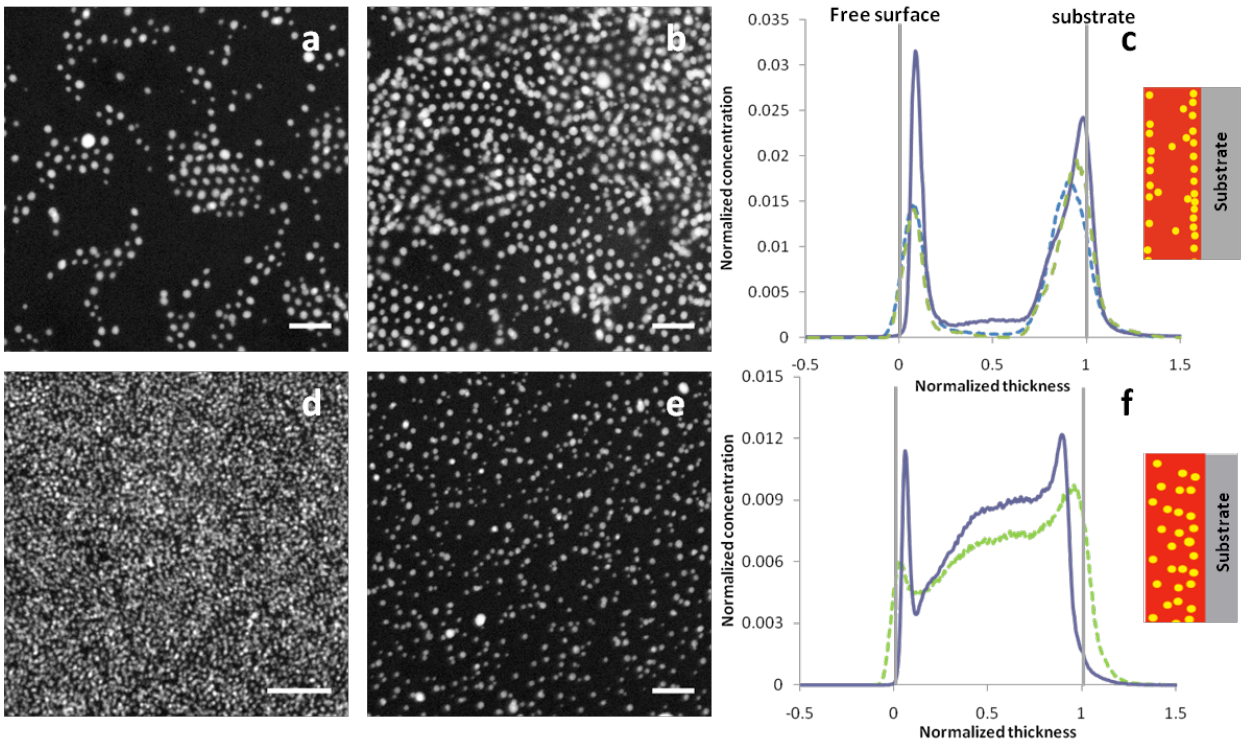

Figure 3.2 (a), (b) and (c) show STEM and DSIMS data of phase separated Au(7)PS_{30}/PS_{1630} mixtures, (a) Φ_{Au}~0.02 (wt. fraction), h ~ 54 nm (b) Φ_{Au}~0.02, h ~ 160 nm (c) Au depth profile which contains Φ_{Au}~0.03 , h~ 90 nm (line), Φ_{Au}~0.02 , h~97 nm (dash), Φ_{Au}~0.02 , h~55nm (square dot); (d), (e), and (f) present homogeneous mixtures

where (d) Au(2)PS_{10}/$PS_{70,}$ Φ_{Au}~0.02, h~97 nm (e) Au(5)PS_{50}/$PS_{70,}$ Φ_{Au}~0.02, h~85nm (f) Au depth profile of Au(2)PS_{10}/PS_{70} (dash) and Au(5)PS_{50}/$PS_{70,}$ (line) both containing Φ_{Au}~0.02. Right side of (c) and (f) are the schematics of phase separated and homogeneous films based on DSIMS profile. Scale bar presents 50 nm.

Based on the structural characteristics of these samples, optical models were constructed in order to interpret their SE optical spectra. The optical properties of homogeneous and phase separated mixtures containing 30 wt% Au were characterized and compared to the absorption spectra shown in Figure 3.3a. The absorption peak locations for homogeneous and phase separated mixtures were 533 nm to 538 nm respectively. This slight red shift of the peak would be due to the shorter interparticle distance and local aggregation of NPs in phase separated mixtures (Figure 3.2b). However, the enhancement of the sensitivity, that is, the ratio between maximum and minimum intensity in the SPR band, was an unexpected result. We speculate that this may arise from the unique geometry of the sample. The role of the NP size on the shift may be excluded because these size ranges (D_{core} = 5 and 7 nm) are too small; this interpretation is consistent with theoretical and experimental studies of nanoparticles in solution.

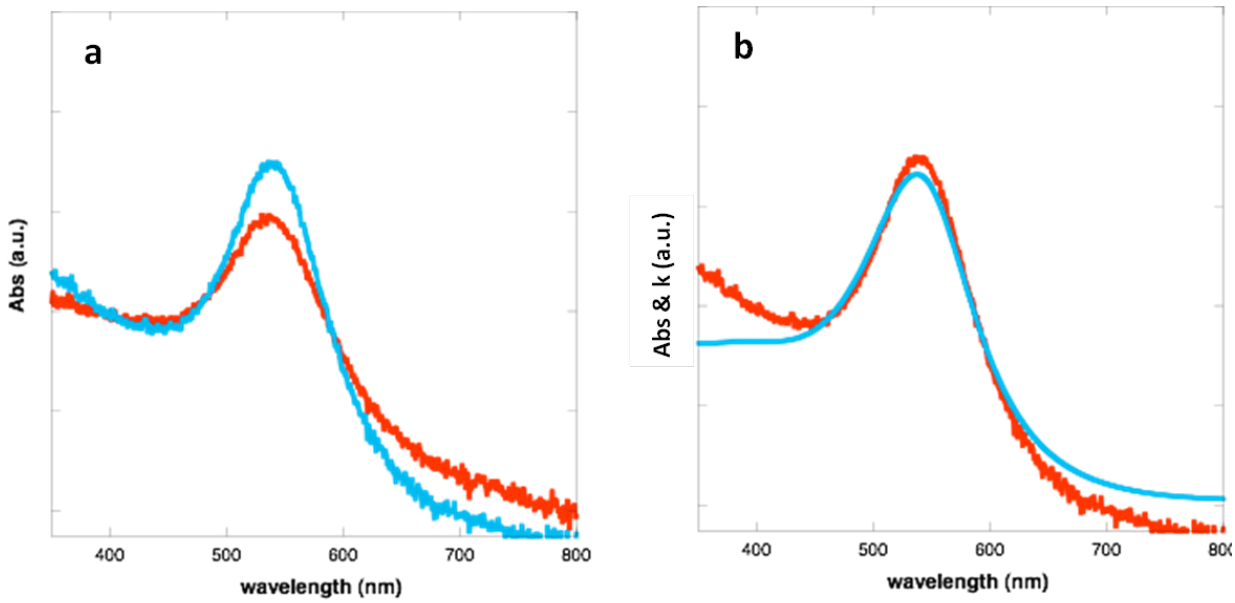

Figure 3.3 (a) Absorption spectra of Au(7)PS_{30}/PS_{1630} (blue, phase separated) and Au(5)PS_{50}/PS_{70}(red, homogeneous) mixtures of Φ_{Au}~0.03(wt. fraction), h ~ 100nm. SPR peak was red-shifted by 5 nm with enhanced refractive index sensitivity (RIS), an intensity ratio between the peak and local minimum within the band from homogeneous to phase separated mixtures. (b) A comparison between absorption spectra from UV-Vis and k (imaginary part of refractive index) from SE of Au(7)PS_{30}/PS_{1630} with Φ_{Au}~0.03, h ~ 100 nm. While two data sets in overall match well, there was a slight deviation below and above SPR band.

The spectroscopic ellipsometry (SE) measurements of the films are now described. Here the complex refractive index is obtained by fitting the measured spectra. We compared the UV-vis absorption spectra with k (imaginary part of refractive index) of the phase separated mixtures to confirm that SE technique is valid to characterize optical properties of these samples. One important thing to bear in mind is the critical difference between angles of incidence used in SE and UV-Vis measurements. SE measures angles

in the range of 40-90 degrees, whereas the UV-Vis measurement angle is 0 degrees (i.e. the entire cross-section of the sample). Moreover, for phase separated films, the effective refractive index should be very different between particle-rich and particle-poor layers. In light of this difference, the optical models to fit SE data must reflect the inhomogeneity in the film.

In homogeneous Au/PS mixtures, two different NP sizes were considered in order to understand the effect of the size on the refractive index of the film. Two samples were: (1) D_{core}= 2 nm, N = 10, P = 1630 and (2) D_{core}=5 nm, N = 50, P = 70 (Figure 3.1e). The data in Figure 3.3a, reveal that the amplitude of SPR peak is smaller and blue-shifted for 2 nm than 5 nm. Peak locations were at 511 nm and 533 nm for the 2 nm and 5 nm NPs, respectively; the 2 nm particles showed less contrast in extinction coefficient ($k_{max}/k_{min\sim450}$). These values are in agreement with the earlier theoretical calculations for corresponding particle sizes. However the peak widths are larger for 2 nm sample; this most likely arises from the effect of size polydispersity.[22] A blue-shift and small intensity of the peak for 2 nm particle samples were due to the short lifetime of plasmon for sufficiently small NPs. This is due to the small mean free path of the electrons in this highly confined 2nm diameter sample [3, 6, 23]. The real part of the refractive index, n, of the Au(5)PS_{50}-PS_{70} sample revealed the existence of a distinctive anomalous dispersion with peak location at ~ 600 nm; the contrast between maximum and minimum values of n are below 0.03. On the other hand Au(2)PS_{10}-PS_{70} sample exhibited a broad shoulder, between 510~650 nm, which is consistent with the Kramers-Kronig consistency between the real and imaginary part of the refractive index near the absorption peaks.

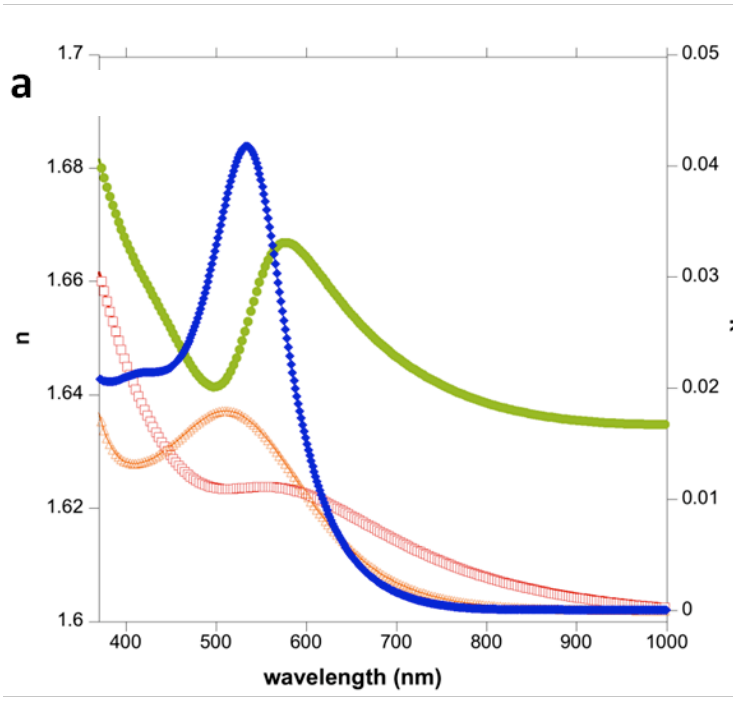

Figure 3.4 Complex refractive index of homogeneous AuPS/PS mixtures; 20 wt% Au(5)PS_{50}/PS_{70} (n: green, k: blue) and 20 wt% Au(2)PS_{10}/PS_{70} (n: red, k: orange) where n is indicated to the left axis and k is to the right.

It is important to note that the phase separated AuPS/PS mixtures could be characterized using three different layers, described here as the top, middle and bottom layers. Schematics of this tri-layer structure (Figure 3.5) show the contrast in the values of n and k between each layer. If we assume that the NPs and the host chains are homogeneously mixed within these individual layers, we can characterize these three layers in terms of their average interparticle spacing. In Figure 3.6, an obvious contrast in the refractive indexes between the separated layers is evident for this 30 wt% Au/PS mixture. Specifically, the SPR peak locations (Figure 3.6b) varied from 535 to 573nm, from top to the bottom layer. In addition, the band was significantly broadened and the peak is red-shifted. The real part of the refractive index, n, showed a maximum contrast from 1.6 to

1.9 in the bottom layer (Figure 3.6a). This variation in refractive index could be interpreted in terms of effective volume fraction and corresponding interparticle spacing within each layer. Based on DSIMS data, the effective volume fractions in each layer were calculated to be 6.4, 0.5, and 6.8 %; in the average (nominal) volume fraction of the entire film is 1.3 %. The average interparticle spacings, l were then calculated to be 16, 290, and 15 nm, for the 6.4, 0.5 and 6.8% regions, respectively. The following equation $l/D_{core} \sim (\varphi_m/\varphi)^{1/3}-1$, where $\varphi_m = 0.638$ is the maximum random packing fraction, was used to perform these calculations.

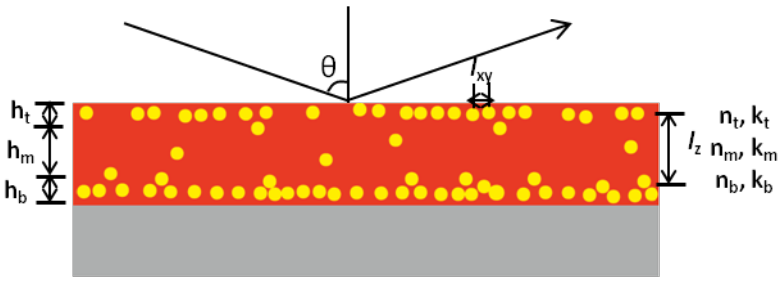

Figure 3.5 Schematics of tri-layer structure divided into top, middle, bottom layers. From SE data, h, n & k of each layer were obtained. Two dominating interparticle spacings could be extracted depending on the direction, l_{xy} and l_z, since middle layer contains negligible amount of Au NPs comparing to other layers. θ indicates angle of incidence.

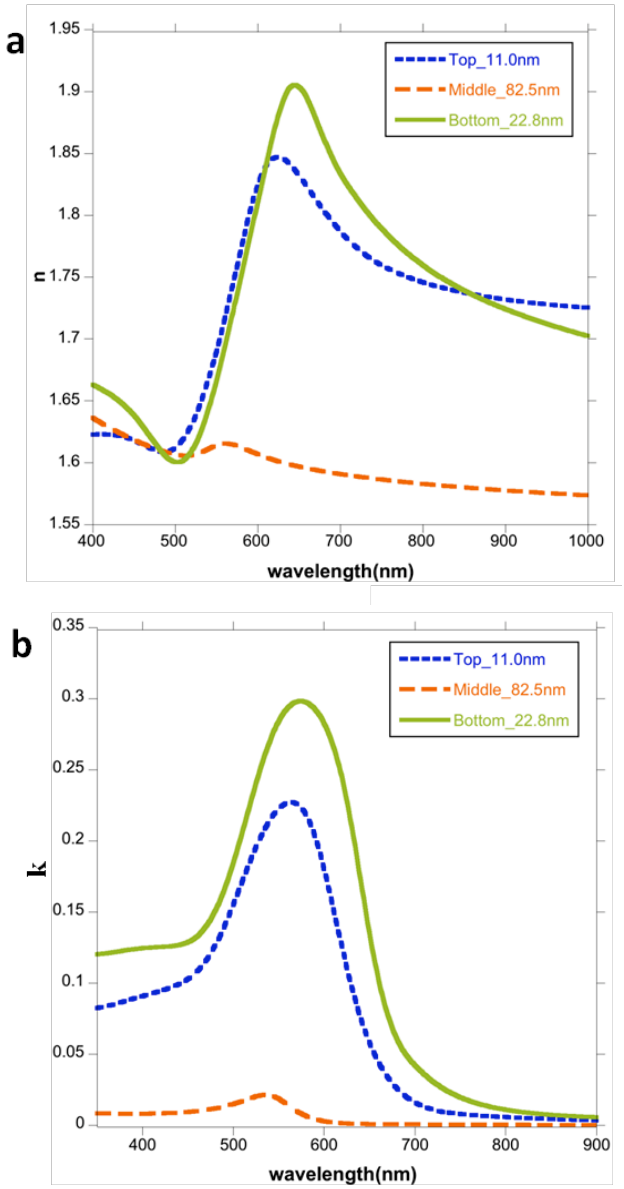

Figure 3.6 Complex refractive index, n (a) and k (b) of tri-layer structure of 30 wt% Au(7)PS_{30}/PS_{1630}. Top, middle, and bottom layer of the sample were shown as square dot, long-dashed, and solid curves respectively.

The interparticle coupling effect, which is supposed to be responsible for the significant red shift and broadening of the band, is reported to be significant when $l \leq 5R$

[7, 10]. However, the average interparticle spacing we obtained from the calculation was approximately equal to the value where the interparticle coupling effect is known to be effective. While the interparticle spacings were somewhat insufficient to explain such a large variation, the NP aggregation into 2-dimensional hexagonal packing, indicated in Figure 3.2a and b, may be responsible for the red-shift and broadening of the band. Descriptions of phase separated samples of different NP concentrations were summarized in Table 1. This data in this table presents the wide range of tunability of the SPR band, and thus the refractive index of the thin film mixtures that may be achieved by tailoring the nanoparticle distributions within a film.

Samples	**h_{total} (nm)**	**φ (vol%, mean)**	**Layer**	**h (nm)**	**φ (effective vol%)**	**Interparticle spacing (nm)**	**Max. peak location (nm)**
10wt%Au(7)PS30/PS1630	151.4	0.61	Top	8.9	4.7	25	552
			Middle	132.1	0	NA	NA
			Bottom	10.4	4.8	24	557
20wt%Au(5)PS50/PS1630	95.3	1.3	Top	10.0	4.3	20	538
			Middle	70.3	0.3	350	533
			Bottom	15.0	4.0	22	535
30wt%Au(7)PS30/PS1630	116.3	2.3	Top	11.0	6.4	16	563
			Middle	82.5	0.5	290	535
			Bottom	22.8	6.8	15	573

Table 3.1 Characterization of phase separated samples of varying NP concentration (Φ_{Au} : 0.01~0.03). Effective volume fraction of each layer was calculated based on DSIMS result. Interparticle spacing was calculated assuming that within the separated layers particles are spatially distributed.

We further characterized the refractive index of phase separated mixtures by differentiating the measurement angles. The optical spectra are expected to vary in the

inhomogeneous samples, based on the angle of incidence. One curve was the result of fitting data measured from 5 or 6 different angles where we separated the ranges into 50-60, 62-70, and 72-80 degrees. As a result, we could gain different optical spectra by varying the angle of incidence; the maximum contrast was shown in the bottom layer (Figure 3.7c). This large contrast may arise from the fact that the bottom layer is adjacent to the substrate where there is a significant and abrupt the shift in dielectric properties. Additionally, the optical spectra obtained from the highest angles of incidence, between 72 and 80 degrees, exhibited a maximum intensity in SPR peak (k) and anomalous dispersion (n) since the light has a higher probability to interact with the thin particle-rich layers. This type of analysis will be also useful in optimizing material performance at angles of incidence other than 0□ for optical coatings [17, 18].

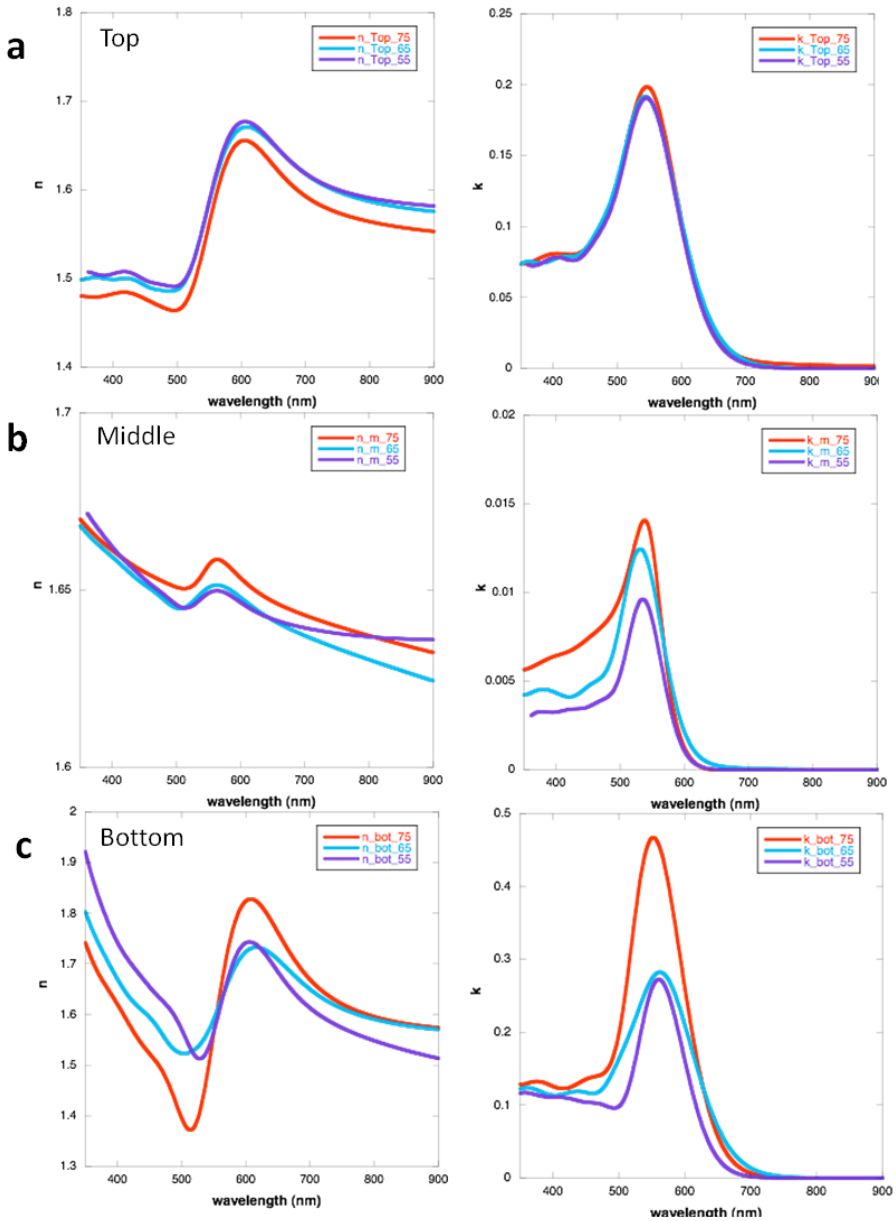

Figure 3.7 Measurement angle dependence on refractive index of phase separated film (30 wt% $AuPS_{30}$-PS_{1630}, h ~ 100 nm) Optical models were divided into three layers: (a) Top (particle-rich) (b) Middle (particle-poor) (c) Bottom (particle-rich) layers. Three different range of angles were identified in the graph; where 55: 50-60 degrees (purple), 65: 62-70 deg (blue), and 75: 72-80 deg (red). Notice the order of magnitude difference in the scale of k between particle-rich (a and c) and particle-poor (b) layers. Largest contrast between the layers was seen for 72-80 degrees.

It is noteworthy that by decreasing the film thickness of phase separated Au/PS mixtures, we no longer obtain multiple optical spectra of particle-rich and particle-poor layers. Films below a threshold thickness appear to lose the contrast between the optical characteristics between these layers, despite the fact that the structure is identical. This apparent contradiction may be understood by evaluating interparticle spacings in xy plane and as a function of depth, z, as indicated in Figure 3.5 (i.e.: l_{xy} and l_z). For samples in table 1, ΔL (=$\langle l_z \rangle$- $\langle l_{xy} \rangle$) are 90, 51, 68 nm for the 10 wt%, 20 wt% and 30 wt% AuPS/PS_{1630}, samples, respectively. However as the h_m and/or mean NP coverage decreases, the contrast between l_{xy} and l_z will be smaller. For the samples described in Figure 3.8, the h_{tot} of each sample are 37.7, 38.4, 67.3 nm where NPs in maximum are able to develop into 3~7 stacks if they are closely packed throughout the film. For phase separated films, the NPs pack into either monolayer or bilayer in interfacial layers. The average values of l_z determined for these samples are 30, 31, 50 nm for the 10, 20, 30 wt% films respectively; these are all much smaller than l_{xy}. Therefore, anisotropy in z-direction does not entail varying refractive index in the film despite the fact that the Au depth profile (Figure 3.2c) shows two distinctive peaks, near free surface and the substrate. As a result, only the 30 wt% sample demonstrated a slight red-shift. The behavior of the 10 and 20 wt% sample, on the other hand, remained similar to the homogeneous mixtures, which is expected when average interparticle spacing, $l_{xy} >> 5R$.

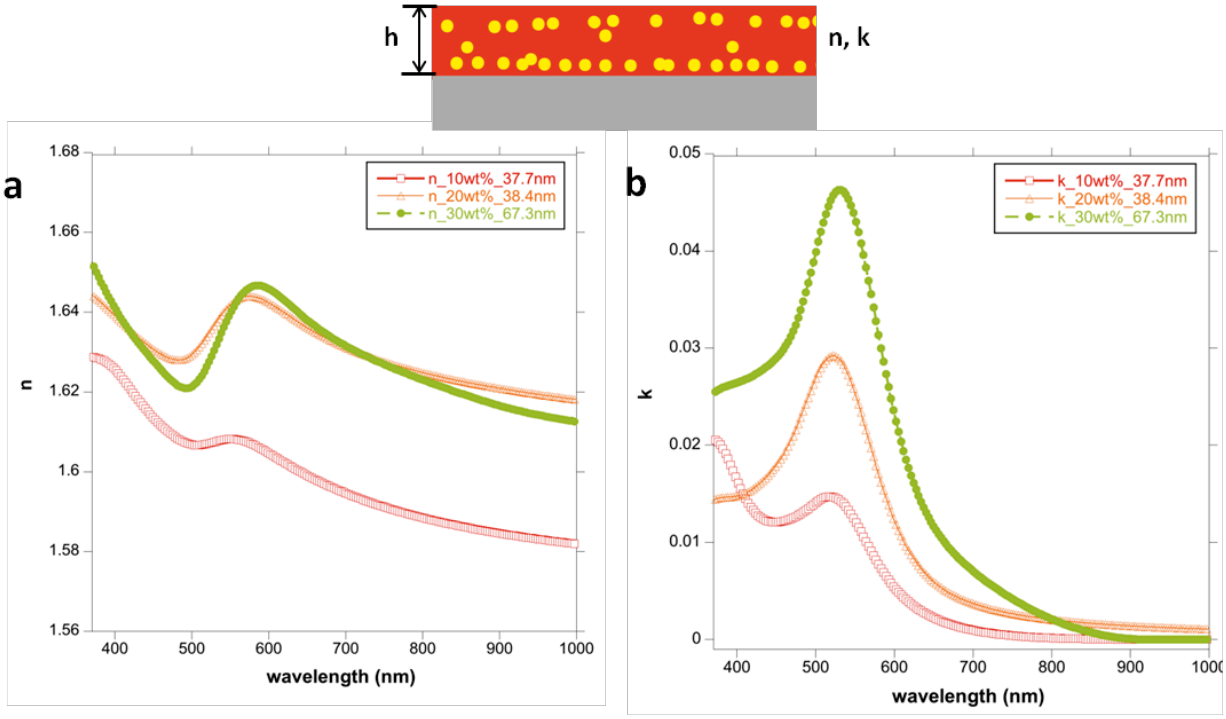

Figure 3.8 Fitted n (a) & k (b) for ultra thin film Au(7)PS_{30}/PS_{1630} mixtures where Φ_{Au}~0.01 (red empty square), 0.02 (orange empty triangle), 0.03 (green circle). Even though NPs are segregated to free surface and the substrate, distance between two NP-rich layers in close proximity that contrast between optical spectra does not exist as in thicker films.

3.4 Conclusion

We established a facile method to tailor and characterize refractive index of polymer/NP mixtures by controlling the experimentally accessible molecular characteristics of the system. The NP distribution in the film was tailored by controlling the nanoparticle size, grafting chains length, grafting density and host chain lengths. Spectroscopic ellipsometry was used to determine the real and imaginary refractive indices of these designed systems. These SE data were interpreted in terms of optical models "built" to reflect the structure of the samples. We showed that the SE spectra manifested details of the structure, phase separated or homogeneous, of the samples. We mentioned that while the SPR peak in homogeneous films corresponded well to the theoretical calculations, the SPR peaks in phase separated films exhibited large red shifts, beyond that expected based on the calculations. This indicates that the local aggregates near substrate and free surface were responsible for the shift and broadening of the peak. Obtaining this type of information is indeed an advantage of the SE measurements. A systematic control of phase miscibility between AuNP and polymer hosts offers unique opportunities to tailor refractive index of thin film polymers for a range of applications, from optoelectonic and/or bio- to chemical- sensor devices.

3.5 References

1. Green, P.F., The structure of chain end-grafted nanoparticle/homopolymer nanocomposites. Soft Matter, 2011.

2. Walters, G. and I.P. Parkin, The incorporation of noble metal nanoparticles into host matrix thin films: synthesis, characterisation and applications. Journal of Materials Chemistry, 2009. 19(5): p. 574-590.

3. Tocho, L.B.S.a.J.O., Size dependence of refractive index of gold nanoparticles Nanotechnology, 2006. 17(5).

4. Chen, X.C. and P.F. Green, Control of Morphology and Its Effects on the Optical Properties of Polymer Nanocomposites. Langmuir, 2009. 26(5): p. 3659-3665.

5. Kubo, S., et al., Tunability of the Refractive Index of Gold Nanoparticle Dispersions. Nano Letters, 2007. 7(11): p. 3418-3423.

6. Alvarez, M.M., et al., Optical Absorption Spectra of Nanocrystal Gold Molecules. The Journal of Physical Chemistry B, 1997. 101(19): p. 3706-3712.

7. Ghosh, S.K. and T. Pal, Interparticle coupling effect on the surface plasmon resonance of gold nanoparticles: from theory to applications. Chemical reviews, 2007. 107(11): p. 4797-862.

8. Katsuhiro, I., et al., Chemical coating of large-area Au nanoparticle two-dimensional arrays as plasmon-resonant optics. Vol. 97: AIP. 221101.

9. Murphy, C.J., et al., Anisotropic Metal Nanoparticles:â€‰ Synthesis, Assembly, and Optical Applications. The Journal of Physical Chemistry B, 2005. 109(29): p. 13857-13870.

10. Su, K.H., et al., Interparticle Coupling Effects on Plasmon Resonances of Nanogold Particles. Nano Letters, 2003. 3(8): p. 1087-1090.

11. Yockell-LeliÃ¨vre, H.l.n., J. Desbiens, and A.M. Ritcey, Two-Dimensional Self-Organization of Polystyrene-Capped Gold Nanoparticles. Langmuir, 2007. 23(5): p. 2843-2850.

12. Atwater, H.A. and A. Polman, Plasmonics for improved photovoltaic devices. Nat Mater. 9(3): p. 205-213.

13. Barnes, W.L., A. Dereux, and T.W. Ebbesen, Surface plasmon subwavelength optics. Nature, 2003. 424(6950): p. 824-830.

14. Barry, P.R., P. Peter, and R.F. Stephen, Long-range absorption enhancement in organic tandem thin-film solar cells containing silver nanoclusters. Vol. 96. 2004: AIP. 7519-7526.

15. Lim, D.-K., et al., Highly uniform and reproducible surface-enhanced Raman scattering from DNA-tailorable nanoparticles with 1-nm interior gap. Nat Nano. 6(7): p. 452-460.

16. Gompf, B., et al., Nanometer-thick Au-films as antireflection coating for infrared light. Opt. Lett., 2007. 32(11): p. 1578-1580.

17. Snyder, P.G., et al., Graded refractive index silicon oxynitride thin film characterized by spectroscopic ellipsometry. Journal of Vacuum Science & Technology A: Vacuum, Surfaces, and Films, 1992. 10(4): p. 1462-1466.

18. Xi, J.Q., et al., Optical thin-film materials with low refractive index for broadband elimination of Fresnel reflection. Nat Photon, 2007. 1(3): p. 176-179.

19. Brust, M., et al., Synthesis of thiol-derivatised gold nanoparticles in a two-phase liquid–liquid system. Journal of the Chemical Society, Chemical Communications, 1994. 1994(7): p. 801-802.

20. private discussion with James Hilfiker and Tom Tiwald from J.A.Woollam company, Inc.

21. D.Palik, E., Handbook of optical constants of solids II. 1991: Academic Press, Inc.

22. Khlebtsov, B., et al., Spectra of resonance light scattering of gold nanoshells: Effects of polydispersity and limited electron free path. Optics and Spectroscopy, 2007. 102(2): p. 233-241.

23. Logunov, S.L., et al., Electron Dynamics of Passivated Gold Nanocrystals Probed by Subpicosecond Transient Absorption Spectroscopy. The Journal of Physical Chemistry B, 1997. 101(19): p. 3713-3719.

CHAPTER 4

DIRECTED ASSEMBLY OF NANOPARTICLES IN BLOCK COPOLYMER THIN FILMS: ROLE OF DEFECTS

The structure of A-b-B diblock copolymer (BCP) thin films is often exploited for "tailoring" the assembly of nanoparticles into various geometries, characterized by long-range order. Mechanistically, the nanoparticles are sequestered within the A or B domains of the copolymer and the domains act as scaffolds to direct the assembly of the nanoparticles. We show that defects play the dominant role in determining the spatial organization of NPs when the NPs are sufficiently large. The nanoparticles preferentially segregate to the core of edge dislocations, which are ubiquitous in ordered thin BCP films of suboptimal thicknesses. We also show that the "healing length," λ, the length scale associated with the transition from an island or hole to the adjacent layer, scales as $\lambda \propto h^{1/2}$, where h is the average film thickness, in accordance with theory. In films of thickness between L and 2L, where L is the domain spacing, λ determines the average size of the region within which the nanoparticles are sequestered.

Reprinted with permission from Kim, J; Green P. F. *Macromolecules* **2010**, 43 (24), 10452-10456.

4.1 Introduction

Functional materials that rely on the combined properties of soft materials and the functionality of inorganic nanoparticles are possible with the fabrication of polymer nanocomposites (PNCs) [1-4]. The use of phase separated A-b-B diblock copolymers as scaffolds enables self-organization of the nanoparticles (NPs) into patterns characterized by long-range order [5, 6]. The long-range nanoparticle pattern is dictated by the BCP domain symmetry because the nanoparticles are confined within the domain with which their interactions are thermodynamically most favorable.

Nanoparticles are known to induce structural phase transitions in BCPs, particularly at higher volume fractions; otherwise they are sequestered within the domains and the structure of the copolymer remains stable [7-11]. The distribution of spherical nanoparticles, of diameter d, within a BCP which possesses a lamellar morphology, for example, is generally determined by the ratio d/L, where L is the interlamellar thickness. Monodisperse particles of sufficiently small d/L, typically $d/L<0.15$, would reside throughout the domains, maximizing the translational entropy. Under these conditions, the chains would stretch, costing entropic (elastic) energy, in order to accommodate nanoparticles; the gain in translational entropy of the nanoparticles offsets this cost in entropic energy [7, 12-15]. However as d/L increases, the penalty due to chain stretching becomes significant and the nanoparticles become more localized toward the center of the appropriate domains. It has been shown that the lateral distribution of nanoparticles within a domain in the BCP/NP system can be quite sensitive to size distributions of nanoparticles; larger particles reside preferentially toward the center of the domains [7, 16-18].

The nanoparticles may form separate phases at sufficiently large nanoparticle volume fractions [15]. Additionally, they may segregate to defects, such as dislocations and grain boundaries, which are well known to exist in bulk BCPs [19, 20]. Generally, they segregate to high angle grain boundaries [21-23]. Larger nanoparticles are also believed to form separate nanoparticle phases within the copolymer. In studies of BCP/NP thin film systems, NPs have been shown to form nanoscale periodic structures, with long-range order, within the phase separated domains of thin film BCPs on chemically or topographically patterned substrate [24-26].

Islands or holes develop at the surface of ordered BCP films of suboptimal thicknesses in order to accommodate excess material not contributing to the formation of a complete layer [10, 11, 27-29]. Edge dislocations are ubiquitous in thin film symmetric BCPs; they accommodate the transition from a complete layer to islands and to holes [28, 29]. In the present study, we show that in thin films defects play the primary role in the self-organization of nanoparticles when d/L is sufficiently large. When d/L is sufficiently small, the nanoparticles reside predominantly within the domains; this situation is well understood. However, for larger d/L, the nanoparticles do not necessarily form a separate phase, as is generally believed; instead they reside almost exclusively at the core of edge dislocations in thin films. Generally, the nanoparticles form clusters within the domains. Layers (domains) within the film undergo significant local elastic deformations in order to accommodate the formation of nanoparticle clusters, particularly at high nanoparticle concentrations.

4.2 Experimental

Gold nanoparticles (Au NPs) were synthesized using the two-phase arrested precipitation method reported by Brust et al.[30]. Thiol-terminated polystyrene molecules (PS-SH) of number average molecular weight M_n=1,000 g/mol (M_w/M_n=1.4), purchased from Polymer Source, Inc., were grafted onto the surfaces of the nanoparticles that were synthesized. Details of our synthetic procedures are described in earlier publications [31, 32].

The diameters of the NP cores, D_{core}, and the brush thicknesses were determined from scanning transmission electron microscopy (STEM) images of the samples, obtained using a JEOL 2010F electron microscope operated at 200 KV. The average particle sizes were determined by measuring the diameters of groups more than 300 NPs in the images. (An example of particle size analysis is described in Appendix A) Two sets of grafted nanoparticles were prepared: (1) D_{core}=5.1±1.2 nm; diameter of the nanoparticle (core + grafted layer (brush) thickness) D_{NP}=8.9±1.1 nm; chain grafting density, σ=2.1 chains/nm^2; (2) D_{core}=1.8±0.5 nm; D_{NP}=4.5±1.1 nm and σ=1.4 chains/nm^2.

Poly(styrene-b-n-butyl methacrylate) (PS-b-PnBMA) diblock copoymers of number average molecular weight M_n=86,700 g/mol and dispersion M_w/M_n=1.08 were purchased from Polymer Source, Inc. The M_ns of the PS and the PnBMA blocks were 43,700 g/mol and 43,000 g/mol, respectively; the volume fraction of PS block was f_{ps}=0.58.

Homogeneous solutions containing well defined concentrations of the copolymer and the nanoparticles were prepared using toluene as a solvent. The solutions of PS-b-PnBMA/AuPS mixtures were spin-cast onto silicon nitride (Si_3N_4) coated silicon

substrates. The Si_3N_4 layer of thickness 100 nm was grown by LPCVD (WaferNet, Inc.). The initial film thicknesses, h_0, of the nanocomposite samples were determined using spectroscopic ellipsometry.

The morphologies of the block copolymer films, the Au NP distributions and the topographies of the sample were determined using a combination of scanning force microscope (SFM) and scanning transmission electron microscopy (STEM). Those samples that were examined using STEM were prepared first by spin casting the solutions onto a glass slide and then floating the film from the slide onto a bath of distilled water. The films were then transferred from the water bath onto a Si_3N_4 grid. These samples were then dried by annealing them in vacuum at 60 °C for 16 hrs. They were subsequently subjected to supercritical carbon dioxide (sc-CO_2) annealing at a temperature of T=60 °C and a pressure of P=13.8± 0.3 MPa for periods between 2 hrs and 72 hrs. Additional details of the annealing procedure are described elsewhere [33]. Sc-CO_2 was used because it is a poor solvent; it plasticizes the films. Using it avoids heating the sample to high temperatures. Therefore thermal stability of the samples was ensured. The primary effect of sc-CO_2 is to swell the films. Considerably less swelling occurs in sc-CO_2 environments than in toluene vapor; the swelling is readily controlled through varying of the amount of sc-CO_2 and the related pressure. (swelling amount as a function of pressure is included in Appendix C) STEM was used to determine the Au NP distributions throughout the samples before and after sc-CO_2 annealing. Many of the samples that underwent sc-CO_2 annealing were also subjected to Ruthenium tetraoxide (RuO_4) vapor for 5-10 min and then examined using STEM. RuO_4 selectively stains the PS phase. Image J software was used analyze the STEM images.

SFM measurements were performed on the films using the MFP-3D (Asylum Research, Inc.) microscope, in tapping (AC) mode**.** Silicon cantilevers (Olympus, Inc.), each with a spring constant of 42 N/m and resonant frequency of 300 kHz, were used. The SFM images were analyzed using Igor Pro (Asylum Research, INC.) software.

The lamellar spacings, L, of the films can readily be measured using SFM by taking advantage of the fact that diblock copolymer films, and droplets, form steps when in contact with the substrate. They are readily observed by scratching the film, thereby exposing the underlying substrate, and then annealing. The step heights provide a measure of the interlamellar spacings of the phase separated system. The edges of PS-b-PnBMA form steps on Si_3N_4 and on SiO_x, substrates upon annealing in air and in sc-CO_2. The step heights determined from samples annealed in vacuum at 150 °C were 32 nm and they were 34±2 nm for samples annealed in CO_2 at 60 °C. Our data are in agreement with published data on this system [34].

4.3 Results and Discussion

We begin by noting that the PS-b-PnBMA copolymer orders symmetrically on the substrates, wherein PnBMA resides at the substrate and at the free surface. The surface energy of PnBMAis less than that of PS, and it is more polar, which explains the wetting behavior of the material. The lateral distributions of nanoparticles throughout films of thicknesses 1.6L< h< 2L are sensitive to the nanoparticle sizes, as illustrated by the STEM images in Figure 1. The STEMimage in Figure 1a is that of a film containing 3 wt % of the Au(5)-PS nanoparticles. The darker regions, within the circular nanoparticle patterns, of the image are holes of depth L belowthe free

surface.The lighter regions are thicker regions of h=2L. Shown in Figure 1b is a magnified image, which includes a hole. It is apparent from this image that while nanoparticles preferentially reside at the boundaries of the hole, they are also distributed throughout the domains at low densities. This behavior is typical of all films in the thickness range L<h<3L that we examined.

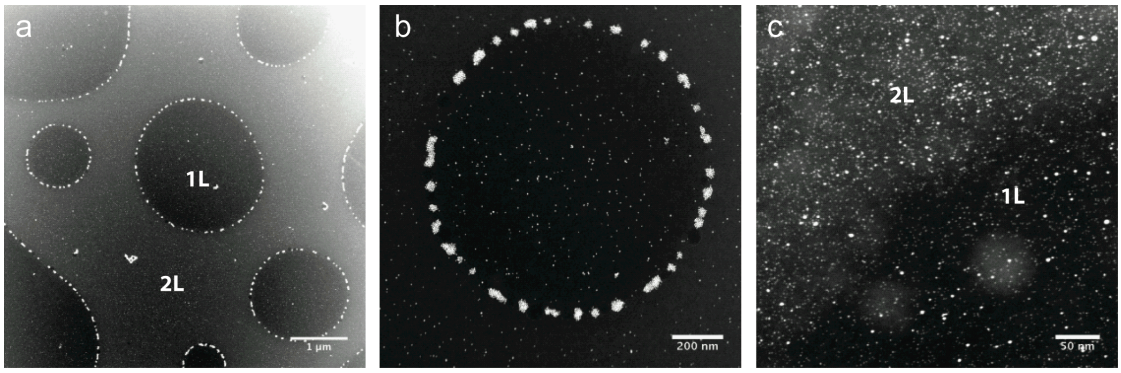

Figure 4.1 STEM images of the lateral distribution of nanoparticles in BCP thin films of thicknesses in the range 3L/2<h<2L, containing 3wt.% nanoparticles, are shown here. (a) The images of a film containing NPs of average diameter (5.1 nm) is shown; the holes are of height h = L above the substrate, and the adjacent layer is of height h = 2L. (b) A magnified image of (a). (c) The edge of a hole in a film containing NPs of average diameter 1.8 nm. Layers of height h = 1L and 2L are identified in the image.

The smaller Au(2)-PS nanoparticles are distributed uniformly throughout the film, exhibiting no evidence of preferential segregation to the boundaries. This is apparent from the high magnification image (Figure 1c) in which the boundary of hole is visible, based on the contrast. In general, preferential segregation is only observed

in BCP films containing nanoparticles sufficiently large in size and cannot be accommodated solely within the domains.

Further insight into the structure of the boundaries is provided in Figure 4.2. A STEM image of a film of average thickness 1.4L, containing 3 wt.% NPs, is shown in Figure 4.2a. The schematic of the distribution of nanoparticles is shown in Figure 4.2b; it indicates that the NP clusters reside at the core of an edge dislocation (extra partial layer). In thin film BCPs, the chains that comprise the dislocation core undergo significant distortion, experiencing a reduction in conformational entropy within the core, in order to accommodate the transition from a complete layer to form an island (or hole) to the layer below [28]. When the nanoparticles are located within the core of the dislocation, the conformational entropy loss associated with chain stretching is minimized. This additional energy gain associated with the incorporation of the nanoparticles, of larger d/L, within the dislocation cores is greater than would be gained by incorporating them within the normal domain structure (Figures 4.2b1 and b2). It is noteworthy that studies of *bulk* BCP-nanoparticle systems reveal that the NPs preferentially segregate at tilt boundaries [22, 35]. In light of this, our observation that nanoparticles of sufficient size would preferentially reside within the defects should not be surprising. The segregation in both cases is due largely to entropic effects.

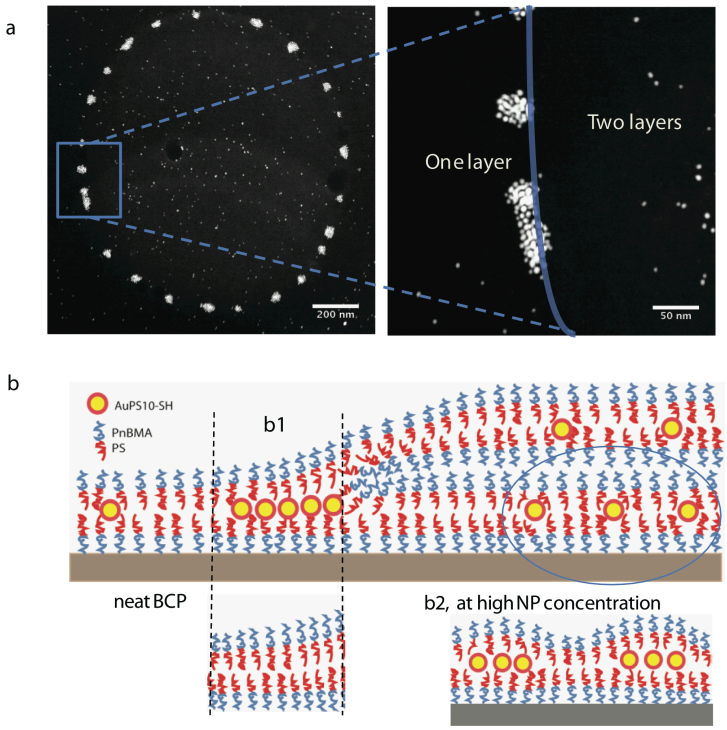

Figure 4.2 Preferential segregation of nanoparticles to the dislocation core surrounding an island. (a) STEM image of nanoparticle clusters at the perimeter of a island in a h=1.4L thick film. (b), Schematic of the cross section of the film, illustrating how the nanoparticles are located at the core of an edge dislocation (extra partial layer); (b2) a copolymer domain layer is shown to undergo a local elastic distortion to accommodate nanoparticle clusters.

An assessment of the early time evolution of the nanoparticle distribution of a film containing 3 wt.% NPs, using STEM, is illustrated in Figure 4.3. Initially, after spin casting, the NPs are nearly uniformly distributed throughout the film, as shown in Figure 4.3a. The islands and holes do not exist at this time. Nanoparticle aggregates begin to form upon annealing. With increasing time nanoparticle aggregates begin to form (Figure 4.3b). These aggregates reside at the boundaries of islands (Figure 4.3c) (and holes) in the ordered film. In short, our observation is that the islands and holes form concurrently

with the segregation of the nanoparticles to the boundaries.

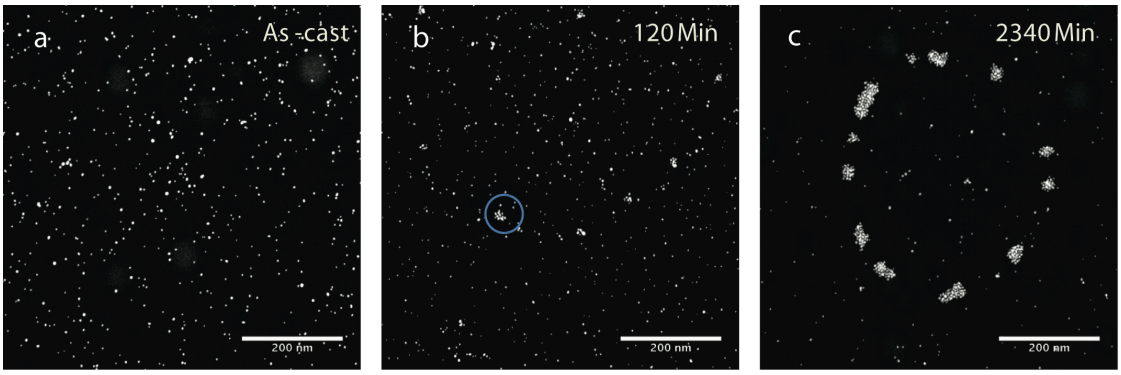

Figure 4.3 Structural evolution of a BCP film (h=1.4L). (a) As-cast; (b) time=120min; (c) time=2340 min.

For samples containing larger NP concentrations, the average size of the NP clusters increase; additionally NP clusters reside throughout the surface of the film. The lateral distribution of NPs is illustrated in Figure 4.4a for a sample containing 13 wt.% nanoparticles; the average NP cluster size is larger than that of the 3 wt% samples. Unlike the 3 wt% samples, NP clusters reside throughout the domains, away from the boundaries. The existence of clusters away from the boundaries of the islands is particularly evident from the STEM image in Figure 4.4b and the SFM image in Figure 4.4c. A line profile from the SFM image (Figure 4.4d) indicates that regions away from the islands exhibit significant local elastic deformation to accommodate the nanoparticles. In fact, the increase in thickness locally is ~50% larger than the domain size.

The basic picture that emerges is the following. For the smallest values of d/L, the nanoparticles reside throughout the appropriate domains and maximize their translational entropy. However for sufficiently large d/L, the nanoparticles preferentially reside in the

dislocation cores where it is entropically more favorable. Clearly, there is a partitioning of these larger nanoparticles between the dislocation cores and the normal domains, based on nanoparticle composition and size.

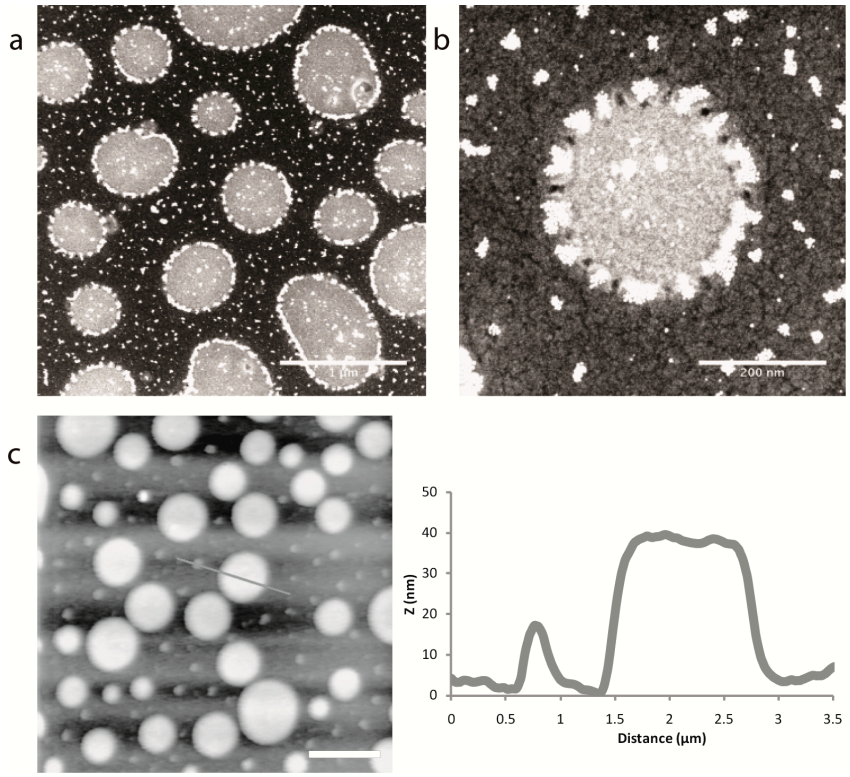

Figure 4.4 Lateral distribution of nanoparticles in film of thickness h=1.4L containing 13 wt % NPs. (a, b) lateral distribution of nanoparticles. (c) Lateral force microscopy image (d) A line scan showing the dimensions of an islands as well as the local elastic deformation of the domain that develops to accommodate a nanoparticle cluster.

We now further discuss the role of dislocations toward nanoparticle sequestration. For a sample of $L < h < 2L$, an edge dislocation would necessarily resides near the free surface, stabilized by the surface tension. Turner et al. have shown that for a lamellar

structure of n layers, in contact with a substrate, the total elastic energy of a single dislocation is approximated to be

$$F \approx (L/2)\gamma_{AB}+(L/2n^{1/2})(\gamma_{AB}\gamma) \quad (4.1)$$

where γ is the surface tension of the component exposed to the free surface and $\gamma_{AB} \approx (KB)^{1/2}$, where K and B are the bending and bulk moduli, respectively [29]. This approximation assumes that the dislocation resides at its equilibrium location, near the center of the film. Generally, it is shown that the depth of the dislocation below the surface of the film is determined by $\gamma_{AB}/(KB)^{1/2}$. Note that the cost of placing an extra layer at the free surface (i.e., the edge dislocation) is proportional to the surface tension difference between the two components, $h\Delta\gamma$, whereas the cost for placing a dislocation below the free surface is $h\gamma_{AB}$. In the case of our copolymer system, PS-b-PnBMA, it has been shown that γ_{AB}~0.9 dynes/cm^2 and $\Delta\gamma$ ~9 dynes/cm^2 [29]. Therefore the edge dislocation would reside beneath the surface. The "healing length," the length scale over which the boundary extends from the top of the island to the layer below (see Figure 4.5), is

$$\lambda \approx (\kappa H \Gamma)^{1/2} \quad (4.2)$$

where $\kappa = (K/B)^{1/2}$ and H is the total film thickness and $\Gamma = \gamma/(K/B)^{1/2}$. One of the key predictions of the theory is that λ should increase as the film thickness increases and the dislocation resides deeper into the film. The depth of the dislocation below the surface of the film is determined by $\Gamma = \gamma/(KB)^{1/2}$. It is evident from Figure 4.5a, b that λ is nearly twice as large for the thicker (h=5.7L) sample. The data in Figure 4.5c indicate that the healing length in our system scales as in a manner consistent with $h^{1/2,}$ in agreement with the theory as described above.

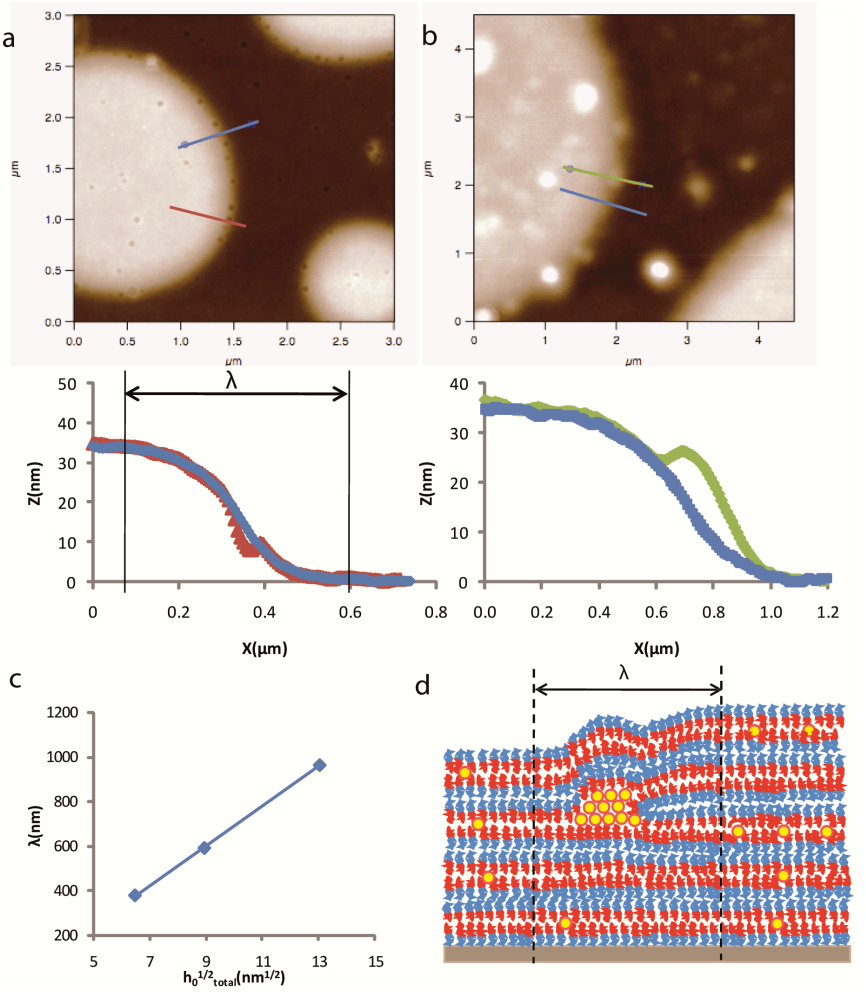

Figure 4.5 The healing length. STEM images of typical islands on films of thicknesses, (a) 81nm (=2.7L) and (b) 170 nm (=5.7L), and their corresponding line profiles at the edge of the islands are shown below each image in order to illustrate the magnitude of the "healing length", λ. The fluctuations in the shape of the lines are due to the presence of nanoparticles. (c) Healing length is plotted as a function of $h^{1/2}$. (d) Schematic, constructed from the topography and STEM image, showing nanoparticles located in the core of an edge dislocation that lies a few layers below the surface of a film.

This observation, $\lambda \propto h^{1/2}$, was first made in a study of pure PS-b-PnBMA systems by Turner et al.[29] While details of the theory remain unexplored, work by Liu et al. made it clear that dislocations would reside within the interior of thick BCP films [36].

In the thinnest films, the healing length is the smallest and the chains undergo more stretching than thicker films in order to accommodate the dislocation at the boundary of an island or hole. We note that when the film thickness increases the dislocation moves deeper within the film as suggested by the theory [29]. When the film thickness increases, the healing length increases; consequently, the chains evidently undergo less stretching to accommodate dislocation formation.

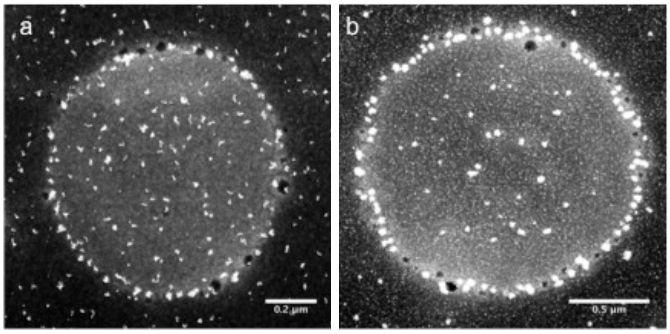

Figure 4.6 STEM images of NP clusters that form in films of different thicknesses: (a) h = 81nm (2.7L) and (b) 170 nm (5.7L).

It would appear that this effect, the increasing λ and the associated relaxation of the chain stretching constraints, would influence the average size of the clusters. The images in Figure 4.6 indicate that the size of the aggregates of the nanoparticles are larger, on average, in the thicker h = 5.7L film (Figure 4.6b) than in thinner h=2.7L film (Figure 4.6a). In Figure 4.6a, the average cluster size is relatively constant, 300±60 nm^2,

regardless of the size of the islands or hole, for a given concentration of nanoparticles. In the case of the h=5.7L film, the average cluster size is 1200 ±400 nm^2. The schematic in Figure 4.5d provides an indication of the probable structure of this system when the film is thick; in this case the cluster is not 2-dimensional, as it is for the thin films of h < 3L.

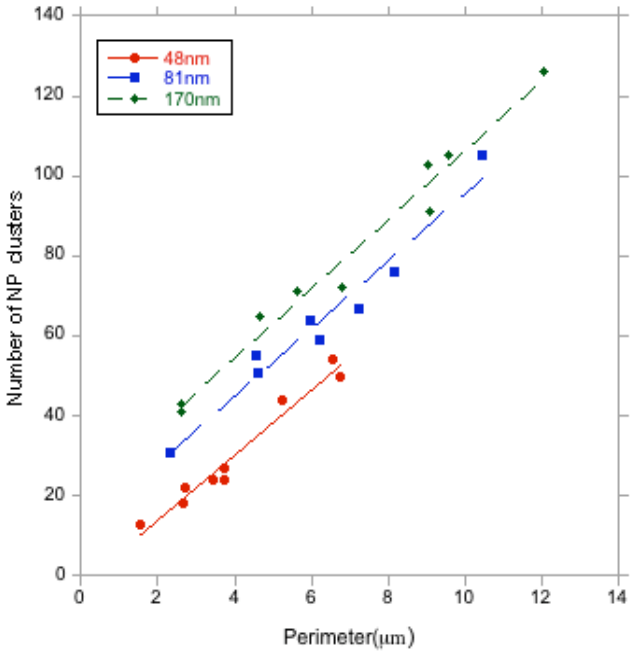

Figure 4.7 Distribution of NP clusters along the perimeters of edge dislocations in films of different thicknesses. Each sample contains 3 wt% nanoparticles.

It is noteworthy that the NPs are not uniformly distributed along the boundaries of the islands (or holes); instead, they form clusters, and the number of clusters per unit length along the perimeter is constant regardless of island size within the film (Figure 4.7). We speculate that the formation of clusters may be understood from the following. The chain grafting density of the nanoparticles and the grafting chain length are such that the PS components of the BCP that comprise the appropriate domains would not

interpenetrate the grafted layers. We are confident of this fact as we have shown that these nanoparticles are immiscible to PS homopolymers of a wide range of molecular weights, as low as 10 kg/mol. In the absence of interpenetration between the grafted and the PS copolymer chains, the nanoparticles show a tendency to cluster in order to minimize the area of contact between the copolymer layer and the nanoparticles. The energy cost is evidently minimized when the nanoparticles form clusters instead for residing uniformly throughout the domains. The fact that the cluster-cluster separation distance is relatively constant is consistent with the notion that the clusters reside within a single plane.

A future study examining the connection between core size, healing length, and the depth of the dislocation below the free surface is planned. Such a study would include thicker films, and it is possible to get cross-sectional TEM images showing the location of the dislocation below the free surface, enabling a direct comparison with additional predictions of the theory. We are currently examining the long-time structural of the evolution (i.e., coarsening phenomena) of the islands/holes, using the nanoparticles as markers.

4.4 Concluding Remarks

We showed that defects play a central role in the assembly of nanoparticles into block copolymer thin films, particularly for sufficiently large d/L. Specifically, for nanoparticles of d/L~0.25, a significant fraction of the nanoparticles reside at the core of edge dislocations. However, when d/L is very small the nanoparticles tend to be located within the domains, thereby maximizing the translational entropy, which is well known.

Our findings will impact the manner in which BCP thin films are used for nano-fabrication. Nanoparticles of larger d/L do not necessarily form separate phases as is commonly believed. Future theoretical efforts should consider the role of defects and their impact on the free energy of the films in order to understand phase transitions and other structural phenomena in thin film BCPs systems containing larger nanoparticles.

4.5 References

1. Bockstaller, M.; Kolb, R.; Thomas, E. L., Metallodielectric Photonic Crystals Based on Diblock Copolymers. Advanced Materials 2001, 13, (23), 1783-1786.

2. Coakley, K. M.; McGehee, M. D., Conjugated Polymer Photovoltaic Cells. Chemistry of Materials 2004, 16, (23), 4533-4542.

3. Huynh, W. U.; Dittmer, J. J.; Alivisatos, A. P., Hybrid Nanorod-Polymer Solar Cells. Science 2002, 295, (5564), 2425-2427.

4. Underhill, R. S.; Liu, G., Preparation and Performance of Pd Particles Encapsulated in Block Copolymer Nanospheres as a Hydrogenation Catalyst. Chemistry of Materials 2000, 12, (12), 3633-3641.

5. Bockstaller, M. R.; Mickiewicz, R. A.; Thomas, E. L., Block Copolymer Nanocomposites: Perspectives for Tailored Functional Materials. Advanced Materials 2005, 17, (11), 1331-1349.

6. Haryono, A.; Binder, Wolfgang H., Controlled Arrangement of Nanoparticle Arrays in Block-Copolymer Domains. Small 2006, 2, (5), 600-611.

7. Kim, B. J.; Bang, J.; Hawker, C. J.; Kramer, E. J., Effect of Areal Chain Density on the Location of Polymer-Modified Gold Nanoparticles in a Block Copolymer Template. Macromolecules 2006, 39, (12), 4108-4114.

8. Lee, J. Y.; Thompson, R. B.; Jasnow, D.; Balazs, A. C., Effect of Nanoscopic Particles on the Mesophase Structure of Diblock Copolymers. Macromolecules 2002, 35, (13), 4855-4858.

9. Lee, J.-Y.; Thompson, R. B.; Jasnow, D.; Balazs, A. C., Entropically Driven Formation of Hierarchically Ordered Nanocomposites. Physical Review Letters 2002, 89, (15), 155503.

10. Pryamitsyn, V.; Ganesan, V., Strong Segregation Theory of Block

Copolymerâ^'Nanoparticle Composites. Macromolecules 2006, 39, (24), 8499-8510.

11. Schultz, A. J.; Hall, C. K.; Genzer, J., Computer Simulation of Block Copolymer/Nanoparticle Composites. Macromolecules 2005, 38, (7), 3007-3016.

12. Hamdoun, B.; Ausserré, D.; Cabuil, V.; Joly., S., Composites copolymères-nanoparticules : I. Période lamellaire dans le régime des "petites nanoparticules". J. Phys. II France 1996, 6, (4), 503-510.

13. Kim, B. J.; Fredrickson, G. H.; Hawker, C. J.; Kramer, E. J., Nanoparticle Surfactants as a Route to Bicontinuous Block Copolymer Morphologies. Langmuir 2007, 23, (14), 7804-7809.

14. Orso, K. A.; Green, P. F., Phase Behavior of Thin Film Blends of Block Copolymers and Homopolymers: Changes in Domain Dimensions. Macromolecules 1999, 32, (4), 1087-1092.

15. Thompson, R.; Ginzburg, V.; Matsen, M.; Balazs, A., Predicting the mesophases of copolymer-nanoparticle composites. Science 2001, 292, (5526), 2469.

16. Chiu, J. J.; Kim, B. J.; Kramer, E. J.; Pine, D. J., Control of Nanoparticle Location in Block Copolymers. Journal of the American Chemical Society 2005, 127, (14), 5036-5037.

17. Listak, J.; Hakem, I. F.; Ryu, H. J.; Rangou, S.; Politakos, N.; Misichronis, K.; Avgeropoulos, A.; Bockstaller, M. R., Effect of Chain Architecture on the Compatibility of Block Copolymer/Nanoparticle Blends. Macromolecules 2009, 42, (15), 5766-5773.

18. Matsen, M. W.; Thompson, R. B., Particle Distributions in a Block Copolymer Nanocomposite. Macromolecules 2008, 41, (5), 1853-1860.

19. Gido, S.; Gunther, J.; Thomas, E.; Hoffman, D., Lamellar diblock copolymer grain boundary morphology. 1. Twist boundary characterization. Macromolecules 1993, 26, (17), 4506-4520.

20. Gido, S.; Thomas, E., Lamellar Diblock Copolymer Grain Boundary Morphology. 4. Tilt Boundaries. Macromolecules 1994, 27, (21), 6137-6144.

21. Bita, I.; Yang, J. K. W.; Jung, Y. S.; Ross, C. A.; Thomas, E. L.; Berggren, K. K., Graphoepitaxy of Self-Assembled Block Copolymers on Two-Dimensional Periodic Patterned Templates. Science 2008, 321, (5891), 939-943.

22. Listak, J.; Bockstaller, M., Stabilization of grain boundary morphologies in lamellar block copolymer/nanoparticle blends. Macromolecules 2006, 39, (17), 5820-5825.

23. Xu, C.; Ohno, K.; Ladmiral, V.; Milkie, D. E.; Kikkawa, J. M.; Composto, R. J., Simultaneous Block Copolymer and Magnetic Nanoparticle Assembly in Nanocomposite Films. Macromolecules 2009, 42, (4), 1219-1228.

24. Kang, H.; Detcheverry, F.; Mangham, A.; Stoykovich, M.; Daoulas, K.; Hamers, R.; Müller, M.; de Pablo, J.; Nealey, P., Hierarchical Assembly of Nanoparticle Superstructures from Block Copolymer-Nanoparticle Composites. Physical review letters 2008, 100, (14), 148303.

25. Park, S.; Lee, D. H.; Xu, J.; Kim, B.; Hong, S. W.; Jeong, U.; Xu, T.; Russell, T. P., Macroscopic 10-Terabit-per-Square-Inch Arrays from Block Copolymers with Lateral Order. Science 2009, 323, (5917), 1030-1033.

26. Stoykovich, M.; Muller, M.; Kim, S.; Solak, H.; Edwards, E.; De Pablo, J.; Nealey, P., Directed assembly of block copolymer blends into nonregular device-oriented structures. Science 2005, 308, (5727), 1442.

27. Green, P. F.; Limary, R., Block copolymer thin films: pattern formation and phase behavior. Advances in Colloid and Interface Science 2001, 94, (1-3), 53-81.

28. Maaloum, M.; Ausserre, D.; Chatenay, D.; Coulon, G.; Gallot, Y., Edge profile of relief 2D domains at the free surface of smectic copolymer thin films. Physical Review Letters 1992, 68, (10), 1575.

29. Turner, M.; Maaloum, M.; Ausserré, D.; Joanny, J.; Kunz, M., Edge dislocations in copolymer lamellar films. Journal de Physique II 1994, 4, (4), 689-702.

30. Brust, M.; Walker, M.; Bethell, D.; Schiffrin, D.; Whyman, R., Synthesis of thiol-derivatised gold nanoparticles in a two-phase liquid–liquid system. Journal of the Chemical Society, Chemical Communications 1994, 1994, (7), 801-802.

31. Chen, X. C.; Green, P. F., Control of Morphology and Its Effects on the Optical Properties of Polymer Nanocomposites. Langmuir 2009, 26, (5), 3659-3665.

32. Kim, J.; Green, P. F., Phase Behavior of Thin Film Brush-Coated Nanoparticles/Homopolymer Mixtures. Macromolecules 43, (3), 1524-1529.

33. Meli, L.; Li, Y.; Lim, K. T.; Johnston, K. P.; Green, P. F., Templating of Gold Nanocrystals in Micellar Cores of Block Copolymer Films. Macromolecules 2007, 40, (18), 6713-6720.

34. Lauter-Pasyuk, V., Physica. B, Neutron reflectivity studies of composite nanoparticle – copolymer thin films. Condensed matter 1998, 248, (1-4), 243.

35. Thompson, R. B., Tilt grain boundaries in a diblock copolymer ordered nanocomposite lamellar phase. The Journal of chemical physics 133, (14), 144902.

36. Liu, Y.; Rafailovich, M.; Sokolov, J.; Schwarz, S.; Bahal, S., Effects of Surface

Tension on the Dislocation Structures of Diblock Copolymers. Macromolecules 1996, 29, (3), 899-906.

CHAPTER 5

TIME EVOLUTION OF THE SURFACE NANO-ARCHITECTURE OF A HYBRID STRUCTURED POLYMER/NANOPARTICLE SYSTEM

5.1 Introduction

Precise control of structural properties of materials at the nanoscale is a key challenge associated with the development of nano-structured materials for many technological applications [1]. A class of hybrid materials, soft material/nanoparticle (NP) composites, has been shown for wide range of applications from biosensors [2] and batteries [3] to opto-electronic devices [4]. A common strategy used to fabricate nanostructured within materials is lithography. The self-assembly of NPs to create functional hybrid materials; the material might include; conjugated polymers, block copolymers, liquid crystals, and proteins [5,6]. Lithography may also be exploited to create templates on surfaces on which, the chemistry and topography may be controlled [5,7-10]. A-b-B diblock copolymers, which are known to self-assemble in into different structures (spherical, hexagonal, lamellar), can be induced to self-organize onto templated surfaces, where they would exhibit long-range order, with minimal defects. Appropriate, A or B, domain of these copolymers may be used as scaffolds in order to direct the assembly of the nanoparticles.

A fundamental understanding of the thermodynamics and kinetics processes that

determine nanostructure formation in materials is essential in order to establish a foundation for the design of polymer nanocomposite (PNC) materials. Defects such as dislocations and grain boundaries are ubiquitous in hard and soft materials that possess long-range structural order; controlling them during processing is a major challenge. In the case of BCPs, difficulties largely arise from the fact that such structural disruptions occur randomly during self-assembly process during solvent evaporation; internal stresses develop and disorientations of ordering domains occur [11-13].

Questions related to role of defects in NP organizations in self-assembled A-b-B diblock copolymers are specific interest in the work described here [14,15]. In phase separated BCPs/NP materials, the NPs are organized within the domain structures and defects to minimize the total free energy. In the particle surface is modified to be chemically identical to one of the block domains, competition between translational entropy of the nanoparticles and conformational entropy of block chains to accommodate particles largely determines the location of the nanoparticles. The nanoparticles preferentially reside within the domains of the same chemical structure. If the particles are too large to be accommodated within the domains, then defects in the organization of the phase separated domains (block copolymers, grain boundaries) influence the NP to its location, largely due to entropic reasons. The chains undergo additional stretching, loss of conformational entropy, to accommodate the formation of defects and the accommodation NPs. The alternative process, significant increase in the domain sizes, becomes too costly to accommodate the increasingly large nanoparticles.

In this study we examined the 2-dimensional structural time-evolution of surface nanoarchitectures of A-b-B diblock copolymer thin films containing nanoparticles. In

particular, the BCP films formed a lamellar structure where similar A domain residing at substrate and free surface (symmetric wetting). Film thickness was below 2L, where L is interdomain spacing a partial layer, composed of islands, is formed on the surface of the copolymer. A majority of NPs are segregated to boundaries of islands, where edge dislocation core is located [16]. Figure 5.1 describes the structure of such a system, part a shows the organization of the nanoparticles around the island (part c) and part b is a schematic of the process. The islands are shown to increase in size, with a growth rate that exhibits power law dependence; the behavior is self-similar. Classical coarsening mechanisms, Ostwald ripening and coalescence were typically observed for both pure and NP containing thin film BCPs. The behavior of the pure BCP system is modified by the nanoparticles; changes in the temporal evolution and of the mechanism of the evolution of the surface nanoarchitecture were apparent. The coarsening dynamics of islands is reminiscent of 2-dimensional phase ordering systems of binary alloys, magnetic systems and others [17]. Specifically, each phase in 2-phase regions possesses power-law behavior in growth where the dynamics exhibits self-similarity [17-20].

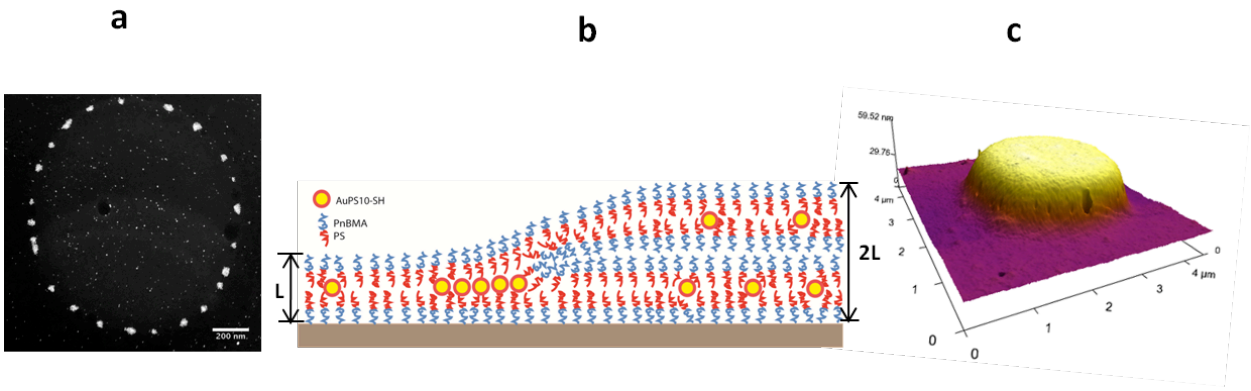

Figure 5.1 Structure of island on top of the lamellar domain of 3wt% $AuPS_{10}$/PS-b-PnBMA. (a) Plane-view of island by HAADF-STEM. NP clusters appear bright surrounding the island (b) schematics of NPs (c) topographical image of island.

5.2 Experimental

Thin films of a Poly(styrene-b-n-butyl methacrylate) (PS-b-PnBMA) diblock copolymer with PS-ligand coated gold nanoparticles (Au NPs) were prepared on silicon substrates, on which there was a native oxide layer of 1.5 nm thick. Solutions, containing 5 wt.% Au nanoparticles, prepared using toluene as the solvent, were spin cast onto SiO_x substrates to create films of thicknesses ranging from 52 nm < h < 55 nm. These films corresponded to thickness of h =1.4L. For the pure BCP, L = 35nm, whereas L=37nm for the BCP/NP mixtures.

The PS-b-PnBMA diblock copolymers of number-average molecular weight, M_n =93000 g/mol (M_w/M_n = 1.08) were purchased from Polymer Source, Inc. The molecular weights of PS and PnBMA blocks were M_n =45000 g/mol and 48000 g/mol respectively, and the volume fraction of polystyrene was f_{ps} = 0.56 (this system forms a lamellar

structure).

The nanoparticles were synthesized using the two-phase arrested precipitation method reported by Brust et al [21]. Thiol-terminated polystyrene molecules (PS-SH) of number-average molecular weight, M_n = 1000 g/mol (M_w/M_n = 1.4) purchased from Polymer Source, Inc. were then grafted onto the surface of nanoparticles. The resulting brush-coated NPs were characterized by scanning transmission electron microscopy (STEM) to determine the average NP core diameter D_{core} = 5.1 ± 1.2 nm, and the overall diameter of the nanoparticle and the brush layer thickness D_{NP} = 8.9 ± 1.1 nm. The grafting density of σ = 2.1 chains/nm^2 was determined based on thermal gravimetric analysis experiments.

The time evolution of topographies of the films was examined using atomic force microscope (AFM), optical microscope (OM) and scanning transmission electron microscopy (STEM). AFM and OM measurements were performed using MFP-3D (Asylum Research, Inc.) and Eclipse LV 150 (Nikon Inc.). Silicon cantilevers (Olympus, Inc.), each with a spring constant of 42 N/m and resonant frequency of 300 kHz, were used.

Samples were annealed under supercritical CO_2 ($scCO_2$) at a temperature of T = 60 °C and a pressure of P = 2000 psi during a time range of t = 150 - 12000 min. The two sets of samples, pure PS-b-PnBMA and 5 wt% $AuPS_{10}$/PS-b-PnBMA, were processed simultaneously. We note that samples of the pure copolymer were analyzed after processing in vacuum at temperatures above the glass transition temperature of the copolymers and the mechanisms that characterize the structural evolution were identical to those that developed in the liquid CO_2 environment under which the present samples

were processed. Ex-situ images of similar areas of the samples were taken by OM and AFM. The island sizes and shapes were analyzed by using Image J, Igor Pro (Asylum Research, Inc.) and WSXM software. Details annealing procedure in $scCO_2$ are described in prior publications.

The samples that were analyzed using STEM were fabricated by spin-casting solutions onto glass substrates, from which they were floated onto a bath of distilled water. They were then picked up onto silicon nitride windows (TEM grid (SPI Supplies)). Images were taken using high annular angle dark field (HAADF) detector (Z-contrast) applying an accelerating voltage of 200 kV.

5.3 Results and Discussion

The optical microscopy images in Figure 5.2 show the topographies, specifically islands, of a pure BCP film and that of a NP/BCP film at various times, throughout the time interval 2500 to 12,000 minutes. In Figure 5.1a, an atomic force microscopy image of a typical island is shown. A STEM image, revealing the gold nanoparticles surrounding an island is shown. A schematic is shown of the edge at an island; the location of the gold nanoparticles in the dislocation core, which surrounds the island, is also evident. Optical microscopy will be used to examine the time evolution of the topography and STEM will be used to examine details of the local nanoparticle distributions in order to get further insight into the mechanism of structural evolution.

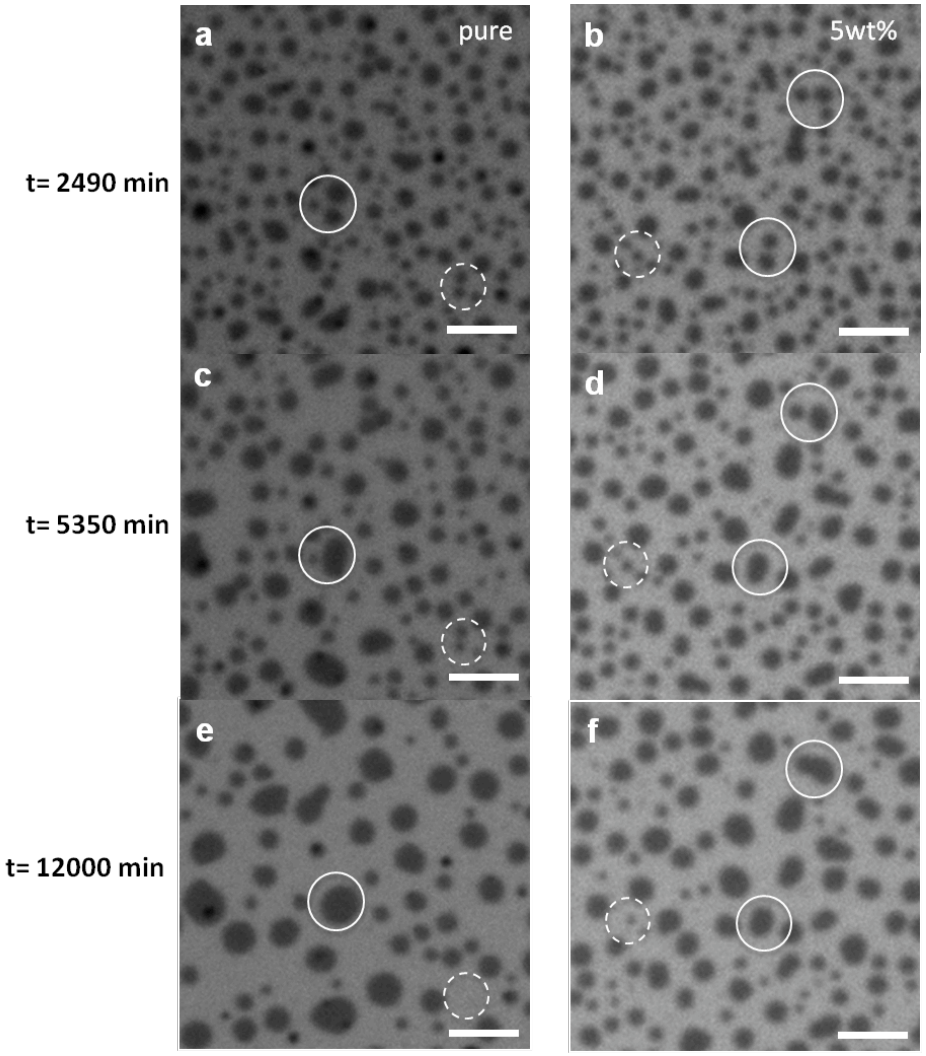

Figure 5.2 Time evolution of islands on thin film PS-b-PnBMA for pure (a, c, e) and 5wt% Au mixtures (b, d, f) at times, t = 2490 min (a, b), 5335 min (c, d) and 12000 min (e, f). Total surface area island for both samples remain 22~23% throughout the annealing period. Solid circle indicates coalescence and reshaping of islands and dashed circle indicate shrinking of islands due to OR. Scale bar corresponds to 5 μm.

The topographies are very similar after 2500 minutes, but are quantitatively and qualitatively different at 12,000 minutes (Figure 5.2e and 5.2f). The dashed circles in the images, taken after 2500 minutes identify islands in both samples. The islands in the

pure BCP gradually disappear whereas they remain, though smaller in size, after 12,000 minutes in the NP/BCP system. The process responsible for the disappearance of the islands is believed to be Ostwald Ripening (OR). The solid circles in the images show the structural evolution, via coalescence, occurs at a faster rate in the pure BCP than in the NP/BCP. We will discuss this issue in further detail below. In the meantime, it is suffice to emphasize that two mechanisms appear to operate simultaneously and are responsible for the evolution of the structure of both systems.

Quantitative information may be gleaned from the systems by analysis of the island sizes and size distributions and comparing them with the theoretical distribution functions. The average area per island, $<S(t)>$ and the number of islands N(t) are shown in Figure 5.3 to exhibit power law dependencies. For the pure BCP, $<S_{BCP}(t)> \sim t^{0.69}$ and $N_{BCP}(t) \sim t^{0.64}$, whereas for the NP/BCP system, $<S_{NP}(t)> \sim t^{0.47}$ and $N_{NP} \sim t^{0.48}$. It is important to note that our analysis was conducted under conditions where the total surface area of islands remained constant at 22-23%. This growth experiment is, within experimental error, $\beta = 2/3$ which is the theoretical classical growth exponent predicted by the theories for capillarity driven growth processes. We note that the growth exponent for our BCP sample is different from that of an earlier study of a pure BCP film. The difference arises from the fact that, as stated by the authors of that study, the interlamellar spacing changed and the total surface area of islands decreased during their experiment. According to the classical theories, the power law behavior is anticipated only during the late stage of structural evolution when the total area is conserved, and the behavior is self-similar.

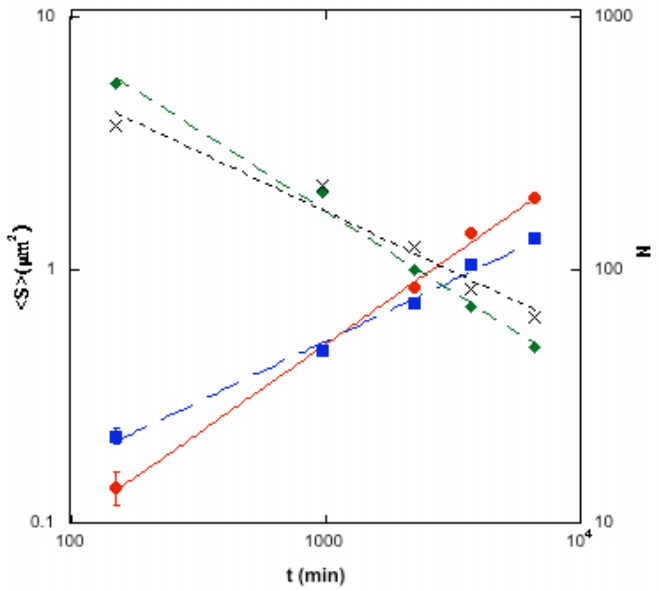

Figure 5.3 Time dependences of average surface area and number of islands, <S(t)> and N(t) for pure and 5wt% samples. All exhibited power law behavior, $<S> \sim t^{\beta}$ and $N \sim t^{-\beta'}$; where β= 0.69 (neat, circle), β= 0.48 (5wt%, square), β'= 0.64 (neat, diamond); β'= 0.47 (5wt%, cross), $R^2 \sim 0.99$ except for $R^2 \sim \beta$ (5wt%) ~ 0.96.

The power law analysis provided only limited insight into the physics and a thorough analysis that involves the use of the distribution functions can reveal more insight into the structural evolution of the system.

In order to do this we now review the classical coarsening theories, Ostwald ripening and coalescence (dynamic and static), that are relevant here [18, 22, 23]**.** The coarsening of the structure of an initially homomogeneous A/B mixture, quenched below a critical temperature into the two-phase regime, may be described within the framework of classical ,coarsening mechanisms such as Ostwald Ripening or coalescence**.** Ostwald ripening (OR) illustrates that islands larger than a critical island radius r_c, grow at the expense of the smaller islands. Lifshitz and Slyozov (LS) used this theory to develop a

late-stage of coarsening in a binary solution assuming atoms (or molecules) have a finite mobility while the islands are static in the limit of dilute volume fraction of minority phase [24]. At a late-stage growth volume fraction of islands remain constant and obeys power law behavior, $r_c \sim t^{\beta}$, where t is time and β is the growth exponent. The island size distribution function F(r, t) can then be described in a scale invariant form $F(R'=r/r_c)$. With these assumptions, Ostwald theory was modeled to describe the bulk-diffusion-controlled dynamics of island. Later on, Wagner included interface-controlled diffusion mechanism into OR theory models [25].

For a two-dimensional island, when the rate limiting step is detachment from the island, then β=1/2. The invariant distribution function is obtained from the solution of the following equation:

$$\frac{\partial F(r,t)}{\partial t} + \frac{\partial}{\partial t}[F(r,t)v(r)] = 0 \tag{5.1}$$

where $v(r) = dr / dt$. With appropriate boundary condition, the distribution function is then,

$$F(R') = \frac{R'}{2}\left(\frac{2}{2-R'}\right)^4 exp\left(-\frac{2R'}{2-R'}\right) \tag{5.2}$$

where F(R□) = 0, when R□ > 2.

However for diffusion-limited process, the growth exponent is β=1/3 and the distribution function yields,

$$F(R') = \frac{CR'^2 exp\left(\frac{-1}{3/2-R'}\right)}{\left(\frac{3}{2}-R'\right)^{\frac{28}{9}}(3+R')^{17/9}} \tag{5.3}$$

where C is a normalization constant and F(R□) = 0 for R□ > 3/2.

Conti et al. have refined the Lifshitz-Slyozov and Wagner's (LSW) theory for more

concentrated islands [20]. According to Conti et al's study, when total surface coverage of the minority phase is above that limit island will prone to contact each other as they grow while the center of the domain is fixed throughout the coarsening procedure. Taking Wagner's self-similarity solution into consideration, probability distribution of OR yields,

$$F(R') = \frac{R'}{R'^{-2\beta R'+2}} exp(-\frac{2\beta}{\sqrt{2-\beta^2}} arctan - \frac{R'-\beta}{\sqrt{2-\beta^2}}) \quad (5.4)$$

where β is constant. The extended solution of OR showed an evidence of coalescence by the integral diverges logarithmically.

Coarsening may also occur from two islands diffusing into each other to coalesce. The coalescence mechanism can be divided into dynamic and static coalescence depending on the motion of center of mass of island. Dynamics coalescence involves diffusion and subsequent merging of islands while static coalescence occurs during the fluctuation in the shape of an island where the center of mass is stationary. Dynamic coalescence is described by using Smoluchowski equation [26], a mean field rate that explains the change in island density by,

$$\frac{dc_N}{dt} = \sum_{i+j=N}^{i\geq j} K_{i,j} c_i c_j - c_N \sum_i K_{i,N} c_i (1 + \delta_{i,N}) \quad (5.5)$$

where c_N is the concentration of islands of size N, and the kernel $K_{i,j}$ is the collision rate constant between islands of mass i and j. The first term describes the coalesced island and second term is associated with the loss due to the irreversible growth of islands. A collision kernel used here is the Brownian diffusion kernel. The growth via Brownian motion, $D_N = D_0 N^{-\alpha}$ exhibit power law scaling, $r \sim t^{\beta}$, where $\beta = 1/d(\alpha + 1)$, and d is dimension (d=2 for islands on flat surface). Finally, the distribution function of dynamic coalescence is,

$$F(R') = \frac{dW(WR')^{d(\alpha+1-(\frac{1}{d}))}}{\Gamma(\alpha+1)} exp(-WR')^d \tag{5.6}$$

where W=$\Gamma(\alpha+1+1/d)/\Gamma(\alpha+1)$ and Γ is the gamma function. Thus, the parameter α is related to the coarsening behavior in dynamic coalescence; for periphery diffusion α yields 3/2 and thus β=1/5; for terrace diffusion (correlated) α =1 and β=1/4; and for uncorrelated diffusion α=1/2 and β=1/3. Probability distributions from Smoluchowski and LSW equations are summarized in Figure 5.4.

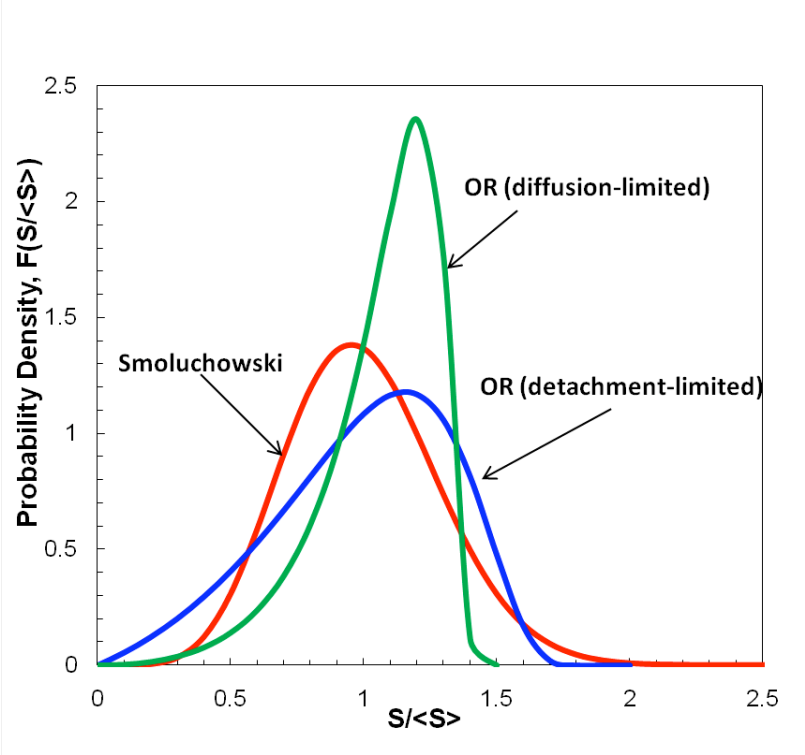

Figure 5.4 Theoretical probability distribution functions, F(S/<S>) versus S/<S> that account for OR (detachment-limited and diffusion-limited) and coalescence respectively.

It is noteworthy that determining operating mechanisms from the probability distributions precautions must be taken, because some assumptions of the classical

theories are not exactly met under experimental conditions. Even though Smoluchowski equation strictly applies for dynamic (Brownian) coalescence, numerical simulations have indicated that the result of static coalescence (islands interact by shape fluctuation) did not present any new length scales to the system [27].

The distributions, determined from measurements of the number of islands of a specific area, normalized by the total number of islands, are plotted in Figure 5.4 for the pure BCP (Figure 5.5a) and for the NP/BCP (Figure 5.5b). The distributions are shown for two different times, 970 minutes and for 6600 minutes. The size distribution for the NP/BCP sample is smaller than that of the pure BCP; this would presumably be due to the role of the nanoparticles decreasing the dynamics of growth. We also note the existence of an anomalous peak at S ~ 0.3 um^2, appearing only in the data representing the NP/BCP sample (t = 6600 min). This suggests the existence of a large number of islands of a certain size that did not further evolve, for a long annealing time. The change in size of these islands is only temporarily suppressed by the nanoparticles; they evolve in size with increasing time.

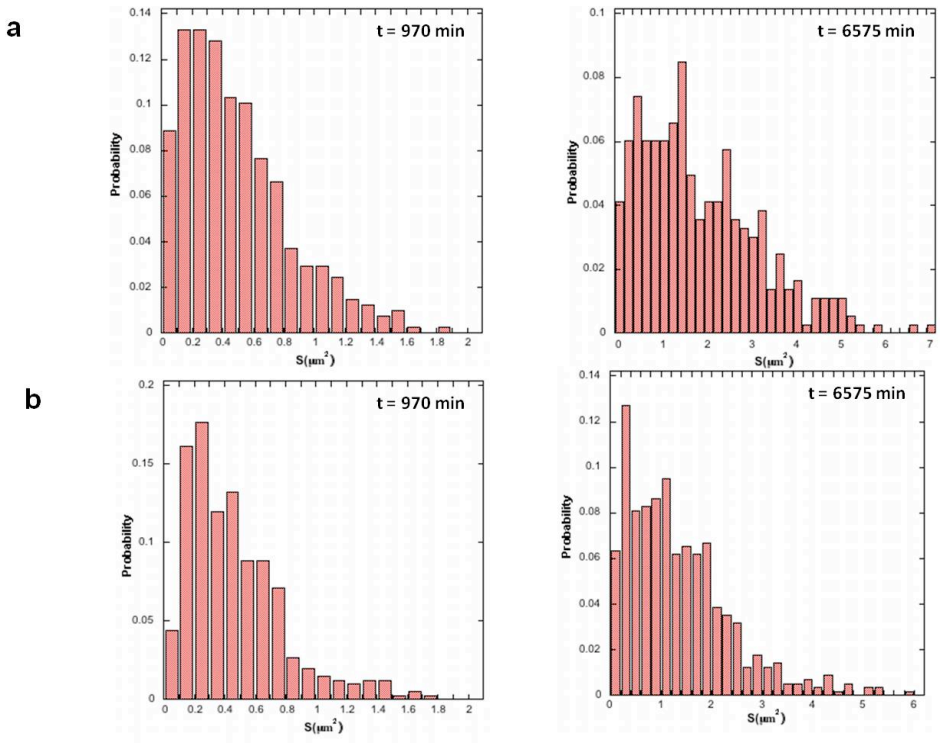

Figure 5.5 Probability distributions of island size (area) for pure (a) and 5 wt% (b) samples of annealing times at t=970 min and 6575 min.

We calculated probability densities of pure and 5 wt% samples in Figure 5.6 and compared them with the theoretical probability distributions for coarsening, i.e. LSW and Smoluchowski equations, for 2D clusters. The island size distribution function, F(S, t) = F(S/<S>) is a time-invariant, dimensionless and asymptotic function where S□=S/<S>. In pure case, probability distributions of islands indicated that coarsening mechanism exhibited a transition from coalescence to OR (detachment-limited). For annealing time t = 150 min (Figure 5.6a) during the initial stages of coarsening, the Smoluchowski equation fit the data reasonably well ($R^2 \sim 0.91$), implying that dynamic coalescence is the primary coarsening mechanism. The growth exponent, β deduced from the single fitting parameter α in Smoluchowski equation (5.6) turns out to be 2/3, which

corresponds well to the experimentally obtained exponent (β ~ 0.69). However, for longer time scales t=3710 and 6575 min, better fit was obtained by the equation that describe the detachment (interface)-limited OR equation (R^2 ~ 0.86) than Smoluchowski (R^2 ~ 0.85) but the difference was within the error range. Even though the dominant mechanism for longer time scales was not distinctive by the comparison with two coarsening theories, it was evident that positive tails have disappeared at the later growth stages. The disappearance of positive tail suggests that OR is becoming more dominant at these time scales. The poor fitting may be due to the fact that LSW equation is truly applicable in dilute systems where islands are sufficiently far apart so they cannot interact or come into contact with each other as they grow. However, any real distribution affected by spatial correlation and thus results in broadening of the distribution. The transition from coalescence (early growth stage) to OR was (later stage) has been observed in other systems such as Cu on Cu (100) [18]. The main reason for this transition emerges from the increase in island mass and distance between the islands with time that makes it harder for islands to come in contact.

On the other hand, in Figure 5.6c the probability distributions for 5 wt% sample were in closer accordance with Smoluchowski equation for all the time scales, t = 150, 3710, 6575 min where R^2 > 0.9. This indicates that the coalescence mechanism dominates the coarsening process throughout the time period of this hybrid sample; contributions to the structural evolution by OR were still apparent, though small. The difference in the dominant mechanisms between pure and 5 wt% was mainly attributed to the NPs that have exclusively formed a cluster along the island boundaries (Figure 5.1a), which will be discussed later in more detail.

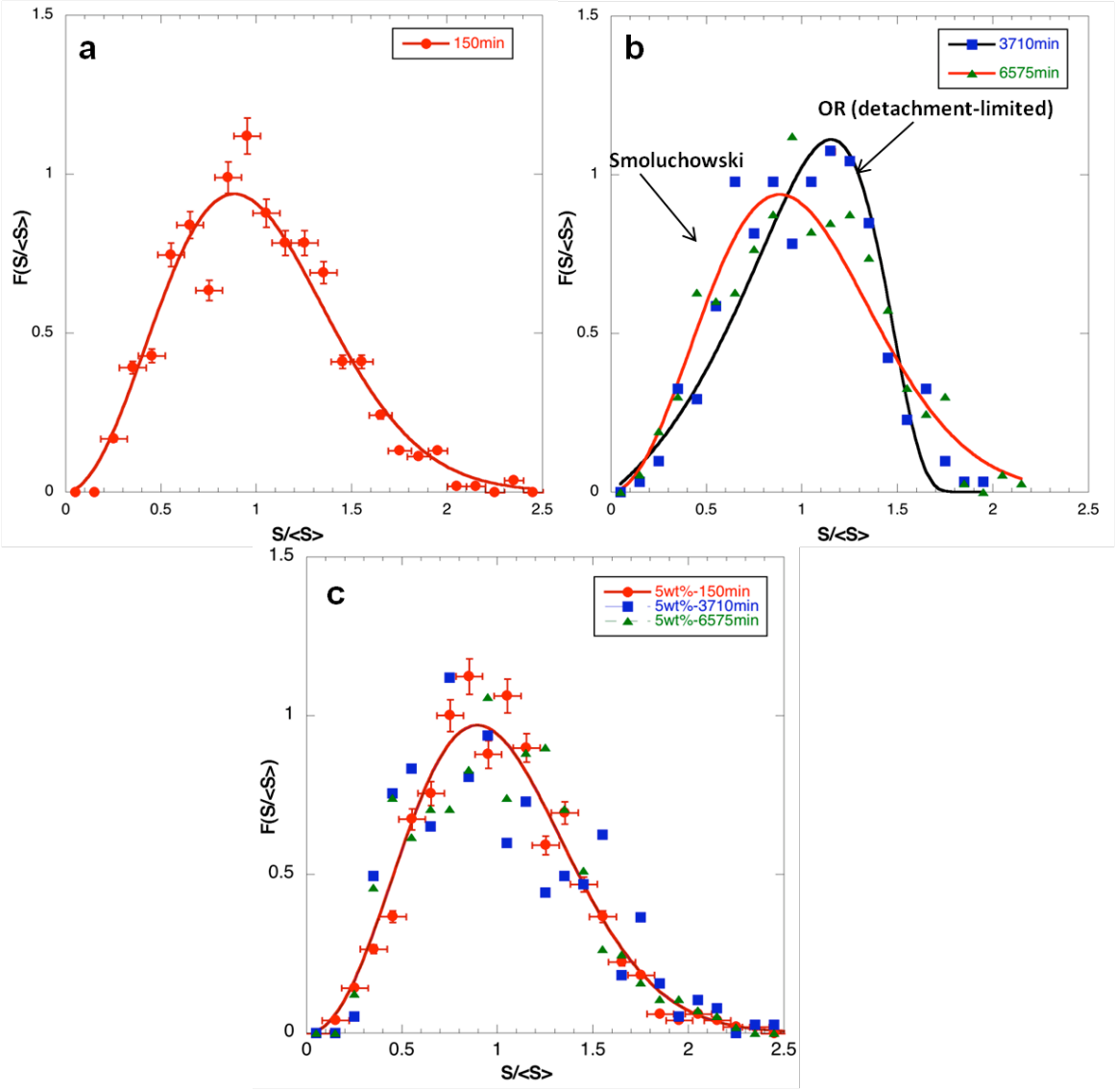

Figure 5.6 Normalized size distribution of islands (R, radius) for pure (a) and 5 wt% (b) samples; t = 150 min (red circle), 3710min (blue square), 6575 min (green triangle). Theoretical curves were fitted to experimental data; black curve indicates OR (detachment- limited) and red curve indicates Smoluchowski equation. For pure case, the peak slightly shifted to the right as positive tails disappeared from 150 min to 3710min. Except for data points for neat at t = 3710, 6575 min other data points showed better fitting to Smoluchowski equation ($R^2 > 0.9$). Error bar is from the area analysis of islands in OM and AFM images.

Despite the fact that all of 5 wt% sample data collapsed into Smoluchowski equation, it is necessary to carefully track the individual islands in the images to determine whether the coalescence is dynamic or not especially at later stages. For example, if we track three islands marked as solid circle in Figure 5.2b (t = 2490 min), it is apparent that two islands merged together in Figure 5.2c (t = 5350 min) possibly during the reshaping (shape fluctuation) process of top right island which appears to be elliptical. From t = 5350 min (Figure 5.2c) to t = 12000 min (Figure 5.2e), remaining island on the left merged into the right island also in the reshaping process. From these observations, static coalescence driven by shape fluctuation turns out to be the mechanism at these stages rather than the by Brownian motion; thus, the coalescence in 5wt% sample for t > 150 min is rather static than dynamic. The growth exponent $\beta = 2/3$ obtained from the Smoluchowski, however, did not correspond to the experimental exponent $\beta = 0.48$. This discrepancy is most likely due to the trapped NPs in boundaries of island (Figure 5.1) slowing down the motion.

Abovementioned discussion, however, does not fully describe the divergence in probability distributions between pure and 5 wt% samples. One possibility for not seeing the transition of coarsening mechanism in 5 wt% sample as in the pure case is because the system has not structurally evolved enough to undergo this transition which, in that case, the threshold (critical island size and distance between islands) for the transition is apparently much higher for the hybrid sample. Another explanation could be the segregated NPs in edge dislocations cores in the boundaries of islands somewhat suppressing OR than coalescence by deterring chains to translate from one island to the

other.

The effect of NPs on island coarsening has been examined in great detail by STEM images. Using the spatial distribution of NP clusters around the island, it was possible to verify the coarsening mechanism of individual islands without in-situ characterization of the sample. Figure 5.7 is STEM images of 3 wt% sample at t = 2340 min (Figure 5.7a) and 12000 min (Figure 5.7b). A contrast between disappearing and growing island was evident in Figure 5.7 from the NP distribution and island shape. One can determine that two islands, indicated as 1 and 2 in Figure 5.7a and b, have been just merged together by the existence of neck in between. We suspect that the shape of these two islands were non-circular before the merging which indicates that these islands have also grown by coalescence. This observation implies that the coalescence is selective towards the islands in the relaxation (reshaping) process consistent with the observations in OM (Figure 5.2). One should note that NP clusters maintained their spatial arrangements around the domain boundaries upon coalescence, meaning that NP clusters translate along with islands during coalescence and the reshaping process. On the other hand, the examples of OR has been denoted as 3 and 4 in the Figure. NP loops or semi-loops in the Figure indicates the location where islands used to locate but disappeared (or disappearing) by OR.

These unique NP morphologies were more common for later time at t =12000 min than t= 2340 min. Specifically, island 3 in Figure 5.7b is an example of an island that is in a shrinking process by OR noticeable by the development of continuous NP chain surrounding the left half of the island. As molecules leave the island by capillarity-driven process, edge dislocations in island boundaries will move toward the center of the island

and moving dislocations carry NP clusters along the path. As a result, distance between NP clusters comes in closer proximity until islands finally disappear leaving NP loops behind. During the OR process, NPs will act as a barrier by limiting the pathway of chains to translate and thus partially stabilizing the edge dislocation core. Trapped NPs in dislocations, therefore, likely to have a stronger influence on OR than the coalescence since NPs constrain individual chains from moving but does not hinder shape fluctuation of islands.

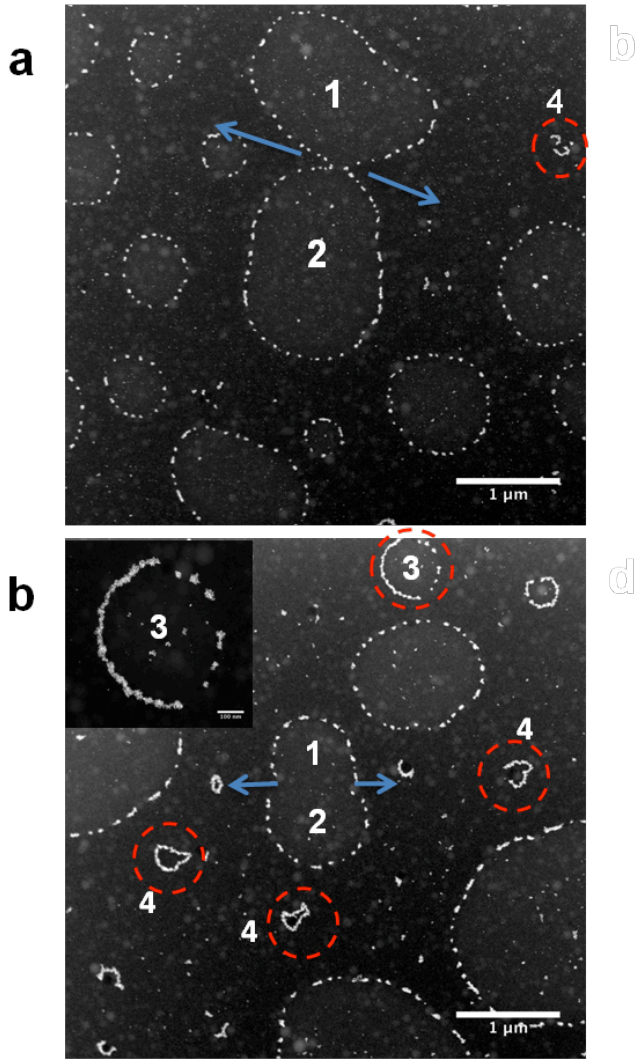

Figure 5.7 STEM images of 3wt% $AuPS_{10}$/PS-b-PnBMA annealing times at t=2340 min (a) and 12000 min (b). Island 1 and 2 indicates coalesced islands in reshaping process. 3

and 4 (red dashed circle) indicates small islands that is disappearing (island 3) or already disappeared by OR (island 4). The inset better illustrates the asymmetrical shrinkage of island 3. Coarsening mechanism operated for each island can be identified from the distribution of NP clusters and the curvature of island.

Finally, we would like to comment on the "dragging" of NP clusters by the moving edge dislocation [28]. This concept introduced by De Gennes' through his calculation of the frictional force a particle experiences while moving parallel to the layers in smectic liquid films. The viscous friction force is an opposing force of the drag force of dislocations. When these opposing forces are in equilibrium, for radius, r of spherical particles,

$$2T\sin\alpha = 8\pi\eta rV \tag{5.7}$$

where T is a line tension of the edge dislocation. Its value is approximately K (bending modulus, ~0.9 dynes/cm for PS-b-PnBMA) and η is the smectic viscosity. The critical velocity, V^* is calculated to be $V^* = T/ 4\pi\eta r$, above this velocity the particles will detach from the edge dislocation and become free. Since NP clusters remain at the island boundaries and being dragged along with the islands during growth we can determine that the velocity of dislocation is lower than the critical velocity. Considering that the shape of NP clusters are close to 2D disks or long ellipses, the viscous friction force of these clusters is at least one order of magnitude smaller than the commensurate volume of a spherical particle. Therefore, unless the host material viscosity is much larger, therefore leading to much larger viscous friction forces, the particles will be dragged along by the dislocations moving parallel to the lamellar structure.

5.4 Conclusion

We examined the effect of "trapped" NPs on the coarsening dynamics of islands by comparing optical microscopy and atomic force microscopy images of islands, and the NP distribution measured by STEM, with theoretical probability distributions. By examining the NP distribution and island shapes, specific coarsening mechanisms responsible for the growth of the islands were identified. The effect of NPs on island growth could be described as follows. During OR, NP clusters acted as a barrier for chains to translate to other islands and thus small islands disappeared at a much slower rate comparing to the pure sample. During coalescence, however, NPs did not appear to influence the shape fluctuation of islands; this led to merging of the islands. The transition between the mechanisms by the presence of NPs contributed to the discrepancy between the island size distribution of pure and NP containing BCP thin films.

5.5 Reference

1. Green, P. F., The structure of chain end-grafted nanoparticle/homopolymer nanocomposites. Soft Matter 2011.

2. Nath, N.; Chilkoti, A., A Colorimetric Gold Nanoparticle Sensor To Interrogate Biomolecular Interactions in Real Time on a Surface. Analytical Chemistry 2001, 74, (3), 504-509.

3. Croce, F.; Appetecchi, G. B.; Persi, L.; Scrosati, B., Nanocomposite polymer electrolytes for lithium batteries. Nature 1998, 394, (6692), 456-458.

4. Atwater, H. A.; Polman, A., Plasmonics for improved photovoltaic devices. Nat Mater 9, (3), 205-213.

5. Sundrani, D.; Darling, S. B.; Sibener, S. J., Guiding Polymers to Perfection:â€‰ Macroscopic Alignment of Nanoscale Domains. Nano Letters 2003, 4, (2), 273-276.

6. Yan, H.; Park, S. H.; Finkelstein, G.; Reif, J. H.; LaBean, T. H., DNA-Templated Self-Assembly of Protein Arrays and Highly Conductive Nanowires. In 2003; Vol. 301, pp 1882-1884.

7. Kang, H.; Detcheverry, F.; Mangham, A.; Stoykovich, M.; Daoulas, K.; Hamers, R.; Müller, M.; de Pablo, J.; Nealey, P., Hierarchical Assembly of Nanoparticle Superstructures from Block Copolymer-Nanoparticle Composites. Physical review letters 2008, 100, (14), 148303.

8. Bita, I.; Yang, J. K. W.; Jung, Y. S.; Ross, C. A.; Thomas, E. L.; Berggren, K. K., Graphoepitaxy of Self-Assembled Block Copolymers on Two-Dimensional Periodic Patterned Templates. Science 2008, 321, (5891), 939-943.

9. Cheng, J.; Ross, C.; Thomas, E.; Smith, H.; Vancso, G., Templated self-assembly of block copolymers: Effect of substrate topography. Advanced Materials 2003, 15, (19), 1599-1602.

10. Stoykovich, M.; Muller, M.; Kim, S.; Solak, H.; Edwards, E.; De Pablo, J.; Nealey, P., Directed assembly of block copolymer blends into nonregular device-oriented structures. Science 2005, 308, (5727), 1442.

11. Listak, J.; Bockstaller, M., Stabilization of grain boundary morphologies in lamellar block copolymer/nanoparticle blends. Macromolecules 2006, 39, (17), 5820-5825.

12. Gido, S.; Gunther, J.; Thomas, E.; Hoffman, D., Lamellar diblock copolymer grain boundary morphology. 1. Twist boundary characterization. Macromolecules 1993, 26, (17), 4506-4520.

13. Gido, S.; Thomas, E., Lamellar Diblock Copolymer Grain Boundary Morphology. 4. Tilt Boundaries. Macromolecules 1994, 27, (21), 6137-6144.

14. Hahm, J.; Lopes, W. A.; Jaeger, H. M.; Sibener, S. J., Defect evolution in ultrathin films of polystyrene-block-polymethylmethacrylate diblock copolymers observed by atomic force microscopy. AIP: 1998; Vol. 109, p 10111-10114.

15. Hahm, J.; Sibener, S. J., Time-resolved atomic force microscopy imaging studies of asymmetric PS-b-PMMA ultrathin films: Dislocation and disclination transformations, defect mobility, and evolution of nanoscale morphology. AIP: 2001; Vol. 114, p 4730-4740.

16. Kim, J.; Green, P. F., Directed Assembly of Nanoparticles in Block Copolymer Thin Films: Role of Defects. Macromolecules 2010, 43, (24), 10452-10456.

17. Bray, A. J., Theory of Phase Ordering Kinetics. Condensed Matter 1994, 43, 357.

18. Alan, L.; Rex, T. S., Kinetic and Monte Carlo models of thin film coarsening: Cross over from diffusion-coalescence to Ostwald growth modes. 2000, 112, (4),

1966-1974.

19. Bassereau, P.; Brodbreck, D.; Russell, T. P.; Brown, H. R.; Shull, K. R., Topological coarsening of symmetric diblock copolymer films: Model 2D systems. Physical Review Letters 1993, 71, (11), 1716.

20. Conti, M.; Meerson, B.; Peleg, A.; Sasorov, P. V., Phase ordering with a global conservation law: Ostwald ripening and coalescence. Physical Review E 2002, 65, (4), 046117.

21. Brust, M.; Walker, M.; Bethell, D.; Schiffrin, D.; Whyman, R., Synthesis of thiol-derivatised gold nanoparticles in a two-phase liquid–liquid system. Journal of the Chemical Society, Chemical Communications 1994, 1994, (7), 801-802.

22. Green, P. F., Wetting and dynamics of structured liquid films. Journal of Polymer Science Part B: Polymer Physics 2003, 41, (19), 2219-2235.

23. Limary, R.; Green, P. F., Late-stage coarsening of an unstable structured liquid film. Physical Review E 2002, 66, (2), 021601.

24. Lifshitz, I. M.; Slyozov, V. V., The kinetics of precipitation from supersaturated solid solutions. Journal of Physics and Chemistry of Solids 1961, 19, (1-2), 35-50.

25. Wagner, C., Theory of precipitate change by redissolution Zeitschrift fuer Elektrochemie und Angewandte Physikalische Chemie 1961, 65, 581.

26. Smoluchowski, M. v., Phys. Z. 1916, 17.

27. Sholl, D. S.; Skodje, R. T., Late-stage coarsening of adlayers by dynamic cluster coalescence. Physica A: Statistical and Theoretical Physics 1996, 231, (4), 631-647.

28. Patrick Oswald, P. P., smectic and columnar liquid crystals. Taylor and Francis: 2006.

CHAPTER 6

CONCLUSION

61. Concluding Remarks

This dissertation demonstrated the thermodynamic phase behavior and kinetic processes of the morphological transitions of thin film polymer-coated NPs/polymer mixtures. The studied morphology of thin film PNCs was subsequently correlated to optical properties and dynamics of the film. This final chapter includes the key findings of this research as well as recommendations for future work.

1) **Phase Behavior of Brush-coated NPs in thin homopolymer matrix and its relationship to optical properties**

A systematic study of the thermodynamic phase behavior of PS-coated Au NPs/PS athermal mixtures has been established to control the morphological structure of thin film mixtures. At fixed $R_{core} \approx 5$ nm, we adjusted the degree of polymerization of grafted chain N and degree of polymerization of linear chains P where the grafting density of all the particles were between 1.5 and 2 chains/nm^2. We were able to identify three different regimes: 1) Phase separation with surface instabilities 2) surface segregation 3) miscibility. In regime 1, at dry brush state, $N << P$, NPs exhibited phase separation both laterally and normally to the substrate confirmed by STEM and DSIMS. Surface roughness of the film reflected the lateral phase separation between particle-rich and

polymer-rich regions. Combining the characteristic length of the domains with the surface roughness obtained from topographical images, we could attain the degree of phase separation quantitatively. As the P/N and N increases within regime 1, characteristic length and the RMS were shown to increase. When N was sufficiently small, however, there was no distinctive lateral phase separation and surface roughness for N << P. At N = 10. Particles were segregated completely to two interfaces, i.e. substrate and free surface, showing a tri-layer structure (regime 2). In regime 3, particle and host chains displayed compatibility as host chains are interpenetrated to the brush layer when the brush thickness was larger than the radius of gyration R_g or host PS chains. This study was intended to explain the pure entropic effect on the phase behavior and morphology of brush-coated NPs/homopolymer athermal mixtures.

In the following study, nanoparticle distribution has been controlled by the phase miscibility of polymer/NP mixtures to tailor the refractive index of the polymer film. Spectroscopic Ellipsometry (SE) was used to obtain single or multiple refractive indices in the film depending on the phase miscibility of the mixture. As a proof of concept, we begin the discussion by showing the homogeneous case with two different particle sizes of approximately 2 and 5 nm and compared fitted data with theoretical calculation based on the Drude-Lorentz theory. Once the characterization method was verified, we analyzed a phase separated mixture where a tri-layer structure was developed. We were able to identify the layers in the fitting model to obtain three different optical spectra for each layer: free surface, middle layer and substrate. The large contrast between the interfacial and middle layers was examined especially in the wavelength range responsible for the surface plasmon resonance (SPR) effect. However, the contrast in the

refractive index disappeared within the phase separated film when the total film thickness was small and two particle-rich layers were in close proximity. Using the optical analysis of homogeneous and phase separated mixtures by SE technique suggested a facile route to tailor and characterize optical properties of thin film polymer/NP mixtures.

2) Direct Self-Assembly of NPs on the island boundaries of thin film BCPs and the effect of NPs on coarsening dynamics of islands

In chapter 4, we demonstrated that the NPs arrange themselves as clusters exclusively in defects in thin film BCPs to minimize the elastic energy of chains. When lamellar thin film BCPs forms islands/hole domains at suboptimal thicknesses, edge dislocations develop into the domain boundaries. A majority of NPs of sufficiently large in comparison with lamellar spacing, $R \geq 0.25L$, sequestered into the edge dislocations as a cluster while particles of size $R \leq 0.15L$ were dispersed throughout the film as translational entropy dominates the system. NP cluster size on the boundaries corresponded to the "healing length" of the island, proportional to the square root of film thickness. A surface deformation on island boundaries in the topographical image indicated the location of NP clusters. Self-organization of NPs into topographically developed defects illuminated strong energetic interactions between NPs and surface-driven defects.

The study in chapter 5 was designed to elucidate the role of NPs on coarsening dynamics of islands on lamellar thin film BCPs. The island growth was inhibited considerably by NPs trapped along the island boundaries. To further investigate the island coarsening processes, two mechanisms, i.e., Ostwald ripening (OR) and coalescence, were described to define the dominating coarsening mechanism. Probability distribution

of islands revealed that the presence of NPs had greater influence on OR than on the coalescence mechanism. Hence, coalescence was the governing mechanism for island coarsening in 5 wt% NPs containing film while OR was dominant for pure BCP film at the late growth stage. Characterizing the shape and distribution of "trapped" NP clusters allowed the prediction of the structural evolution of two-dimensional islands.

6.2 Recommendations for the Future Work

In chapter 2, we examined the morphology and phase behavior of thin film PS-coated Au NPs/PS mixtures by tailoring the size ratio between the degree of polymerization of host chains, P and grafted chains, N. Three different phases were identified by the phase miscibility and morphology of the mixtures. One can extend the miscibility parameters to NP concentration and thickness to define the phase behavior from thin film to bulk mixtures. The transition thickness from thin film to bulk is expected to rely on the brush thickness and R_g of host chains at relatively small NP size. In the case of NP concentration, we briefly showed the shift in degree of phase separation by measuring the characteristic length of phase separated domains comparing 2 and 4 wt%. It will be useful to extend the concentration range and to quantify the transitions. In ultra-thin film regimes, packing frustrations may suppress the phase separation and develop into 2D organization. Grazing incidence small angle X-ray scattering (GI-SAXS) may be the appropriate technique to determine long-range structures and characteristic length of the PNC film. Phase behavior of other polymer systems, including biopolymers and semi-crystalline polymers, can be explored using a similar concept. As one expands the materials systems, more critical parameter space may emerge which will be key to

theoretical and simulation studies on this topic. These experiments will possibly facilitate broadening our understanding of phase behaviors on thin film PNCs and enlighten our development of new design rules.

In this study, we have correlated the optical properties with the phase miscibility of thin film PS-coated Au NPs/PS mixtures. On the condition of N << P for short N where NPs are completely segregated to both interfaces, we have identified three layers, i.e., free surface, interior and substrate, to characterize the change in optical constants within the film. Multi-layer films can be fabricated by alternating solvents that will not dissolve the layer underneath. Through this method, advanced functionalities can be developed such as bio-compatible surfaces for sensors and biomedical applications. Processing the multi-layer film in sc-CO_2 will be advantageous since pressurized CO_2 usually enhances the interfacial properties and increases the mechanical stability of the film. Chitosan molecules may be an attractive alternative for their good spin-casting characteristics, abundance in nature, and accessibility as a ligand for Au NPs. Furthermore, thin film polymer-coated AuNPs/polymer can be applied to enhance the performance of organic photovoltaics. The surface plasmon resonance effect of metal NPs is responsible for the increase in efficiency. Our fabrication method of organizing NPs is effective in terms of size and processability. It would be interesting to compare the performance of homogeneously distributed film and tri-layer film, both containing the same amount of NPs.

In chapter 4, we have shown that the NPs preferentially segregated to edge dislocation cores as clusters. Adopting this behavior, one can intentionally pattern the substrate and develop disorientations in the domains, thus creating grain boundaries.

Particles are likely to segregate to the boundaries as indicated in this study. In order to successfully organize particles exclusively into the patterns, one may need to control the shape, size, and periodic spacing of the ordered structures. A hierarchical pattern of clustered NPs presented a configuration distinctive from other thin film BCP-NP hybrid systems. The proposed system of patterning NP clusters, therefore, offers unique opportunities to explore new optical and catalytic properties for bio-sensing and optoelectronic devices as well as serving as a template for further fabrication.

APPENDICES

Appendix A. Nanoparticle size analysis

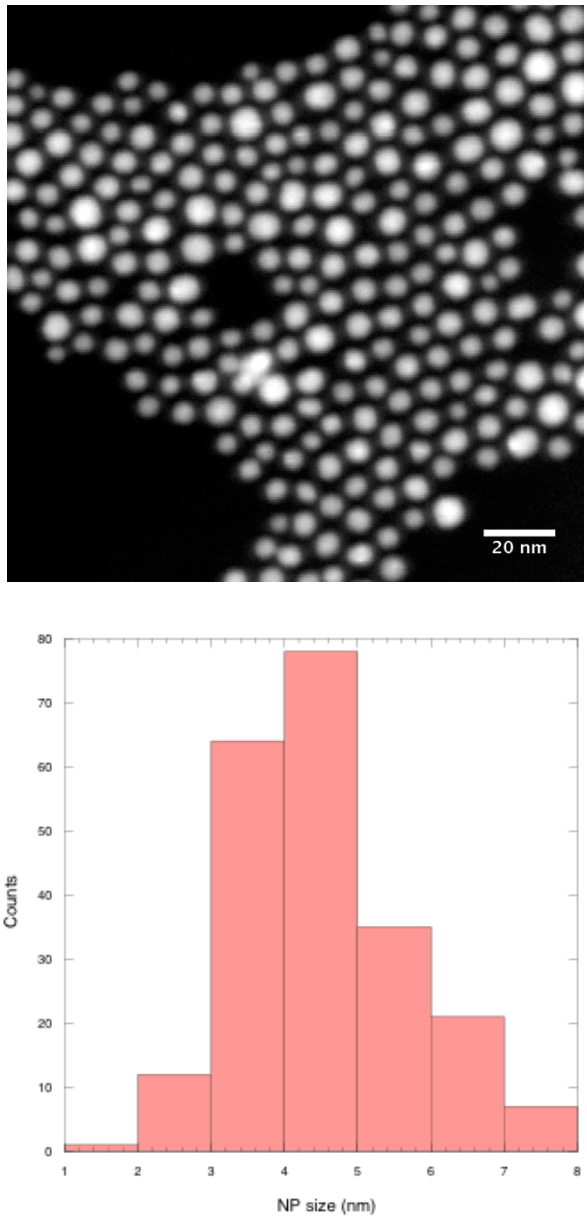

Figure S1. Particle size distribution. D_{core}=5.1±1.2 nm, σ=2.13 chains/nm^2

Appendix B. Lamellar spacing of BCP thin film ($1L < h_0 < 2L$) VS NP concentration

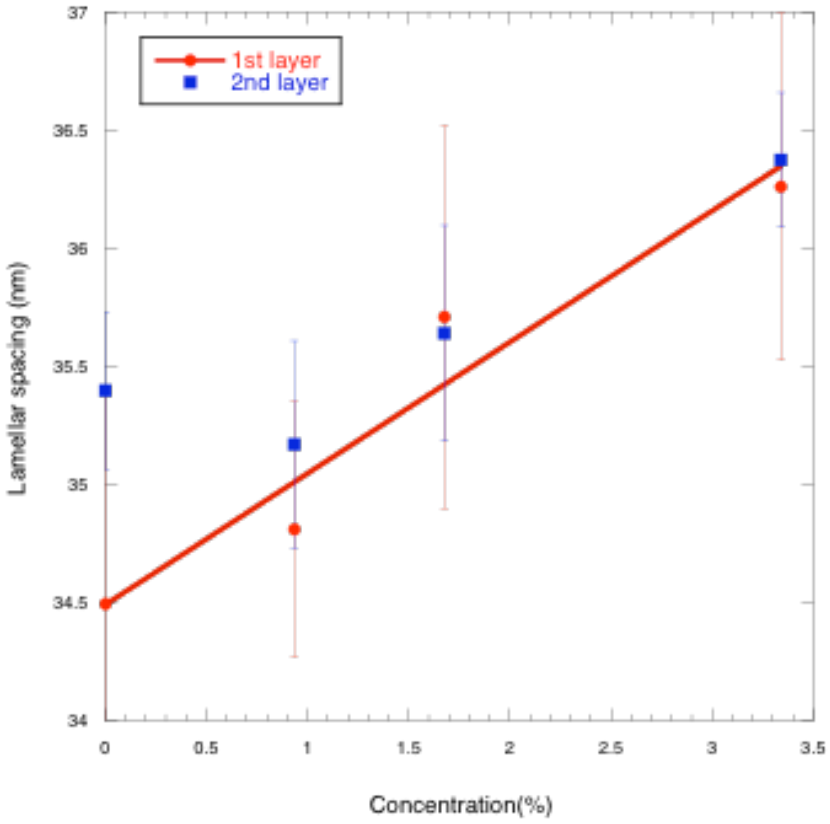

Figure S2. Lamellar spacing of PS-b-PnBMA film as a function of NP concentration. 1st layer corresponds to the layer on the substrate and 2nd layer indicated the island. Solid line accounts for the theoretical prediction $L=L+\varphi/(1-\varphi)$[1]. Domain thicknesses were measured by AFM where the film was scratched prior to annealing.

Appendix C. Thickness swelling of BCP thin film ($1L < h_0 < 2L$) under supercritical carbon dioxide

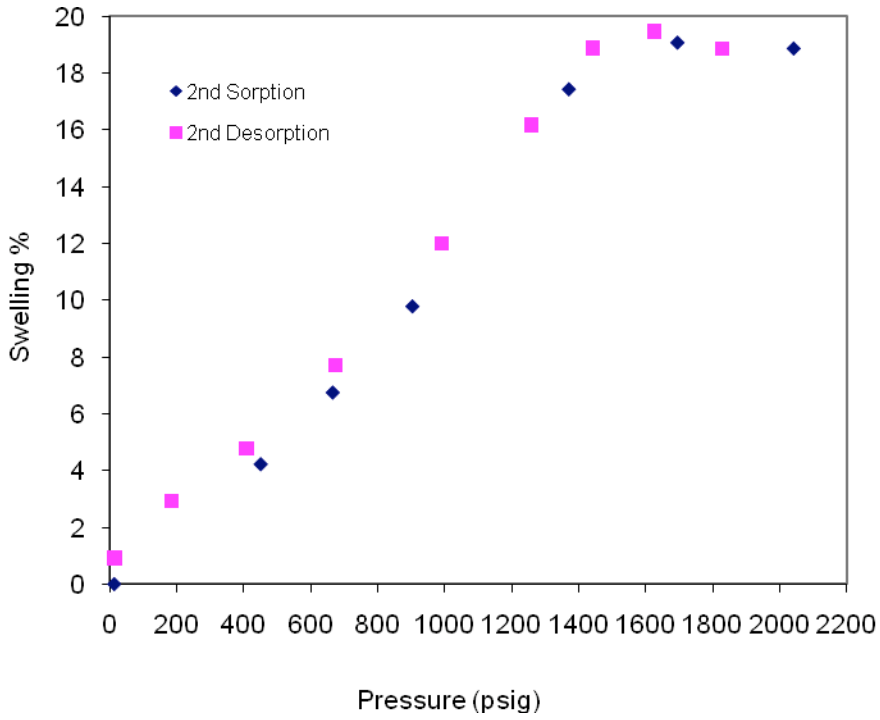

Figure S3. In-situ swelling measurement of neat PS-b-PnBMA film of (~100nm) in supercritical-CO_2 by spectroscopic ellipsometry. Maximum swelling amount was 19% at 1630psi. Detail measurements can be found in reference [2].

Appendix D. Optical characterization of phase separated thin film PNCs

Spectroscopic ellipsometry measures the changes in polarization state of reflected light from the sample. The change in polarization is characterized by ψ and Δ parameters which is defined as

$$\rho = \frac{r^p}{r^s} = \tan(\psi)\, e^{i\Delta}$$

where ρ is defined as the ratio of the reflectivity of the p- polarized light (r^p) and s-polarized light (r^s). To obtain sample properties such as optical constants, thickness, and surface roughness from the measured data, optical model should be established with the exception of bulk samples.

Prior to refractive index analysis, it is best to know the film structure and build a model based on the structure. If not, it would be difficult to obtain a reliable result especially when there are too many unknown parameters. Increase in fitting parameters means that there will be correlations between parameters which produce a vague fitting result. One way to roughly determine whether the thin film mixture is homogeneous or not is to convert the optical model from isotropic to anisotropic and see whether the fitting improves or not.

Data analysis procedures for phase separated mixtures (ex. 30wt% $AuPS_{30}$-PS_{1630}, h~105nm) are the following:

1. Fit measured data with Cauchy layer by selecting transparent wavelength range (ex. 900 nm-1700 nm, differs depending on the sample) to obtain film thickness.

Cauchy layer (fit A, B, thickness)
Native Oxide_jaw (fixed)
Si_jaw (substrate-fixed)

Figure S4. A schematic of the fitting model to determine total film thickness.

2. Convert Cauchy layer to three EMA (effective medium approximation) layers. Each layer is assumed to be a homogeneous mixture. To minimize fitting parameters, first fix Au concentration of the middle layer to zero and the film thicknesses of top and bottom layer to 10~ 15nm based on NP size and the film structure. The thickness of the middle layer will then be determined by the difference between total film thickness and the thickness of top and bottom layer. It would be ideal to have a depth profile of gold by SIMS or RBS (Rutherford backscattering) to input more accurate thickness. Expand the wavelength to 370 nm-1700 nm and fit the data (concentration of top and bottom layer).

EMA (Cauchy + Au) (fix h_{top}: 10~15nm)
EMA (Cauchy) (fix $h_{middle} = h_{tot} - (h_{top} + h_{bot})$
EMA (Cauchy + Au) (fix h_{bot}: 10~15nm)
Native Oxide_jaw (fixed)
Si_jaw (fixed)

Figure S5. A schematic of the fitting model of three EMA layers to distinguish between particle-rich and polymer-rich layers.

3. Fit all film thicknesses and concentrations for every layer including the middle layer (particle-poor layer).
4. Parameterize EMA model to Gen-Osc model and match e2 (or k) shape followed by the e1 (or n) shape by choosing the oscillator types. Replace layer to Gen-Osc layer and fit the data. This procedure should be performed one layer at a time while other layers remain fixed. When assigning oscillators to previously obtained n & k, there should be only one oscillator that describes the SPR band while 3 or 4 oscillators can be assigned for wavelength range other than SPR band. By this

procedure, amplitude, width, and the location of the peak shifts will be adjusted that decreases MSE significantly. (MSE reduced from 7.785 to 3.690 for 30wt% $AuPS_{30}$-PS_{1630} mixtures)

Gen-Osc (used Gaussian oscillators to fit e1 and e2)
Gen-Osc (used Gaussian oscillators to fit e1 and e2)
Gen-Osc (used Gaussian oscillators to fit e1 and e2)
Native Oxide_jaw (fixed)
Si_jaw (fixed)

Figure S6. A schematic of the fitting model converted from EMA to Gen-Osc models.

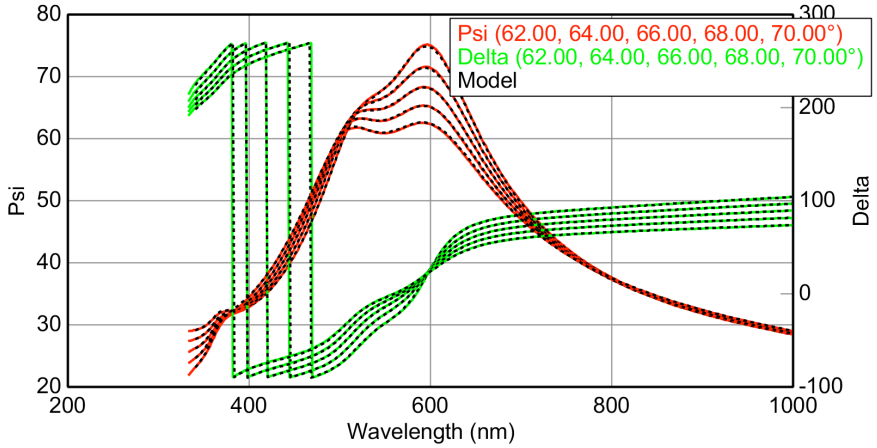

Figure S7. ψ and Δ data as a function of wavelength fitted from the model for 30wt% $AuPS_{30}$-PS_{1630} (h~105nm). CompleteEASE™ software (J.A. Woollam Co.) is used for data acquisition and analysis.

References

1. Hamdoun, B.; Ausserre, D.; Joly, S.; J. Phys. II France 6 (1996) 1207-1217

2. Sirard, S. M.; Green, P. F.; Johnston, K. P.; Spectroscopic ellipsometry investigation of the swelling of poly(demethylsiloxane) thin films with high pressure carbon dioxide. J. Phys. Chem. B 2001, 105, 766−772

3. Snyder, P.G., et al., Graded refractive index silicon oxynitride thin film characterized by spectroscopic ellipsometry. Journal of Vacuum Science & Technology A: Vacuum, Surfaces, and Films, 1992. 10(4): p. 1462-1466.